3D-printed electrodes for redox flow batteries

Kroese, M.

Award date:
2022

Eindhoven University of Technology

Master Thesis

3D-printed electrodes for redox flow batteries

M. Kroese

1011379

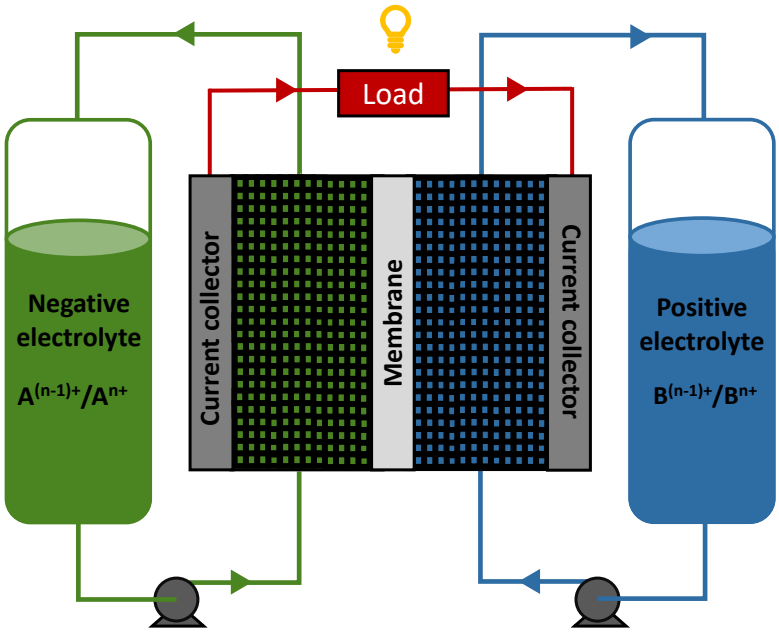

Supervisors:
Ir. M van der Heijden
Dr. Ir. A. Forner-Cuenca

Committee:
Dr. Ing. Z. Borneman
Dr. Ir. D. Giuntini

Eindhoven, March 10, 2022

Acknowledgments

I wish to thank my supervisors Ir. Maxime van der Heijden and Dr. Ir. Antoni Forner-Cuenca for their guidance, enthusiasm and valuable suggestions. They did not only introduce me to the field of electrochemistry, but they also helped me improve on my writing and quality of research. I would also like to thank Dr. Ing. Zandrie Borneman and Dr. Ir. D. Giuntini for taking place in my thesis committee and for the great discussions and valuable feedback about the work.

Furthermore, my appreciation goes out to the support of the staff and students of the Membrane Materials and Processes group, and I am thankful for the opportunity to be part of this group the past year. Particularly I want to thank Emre Boz, Rémy Jacquemond, Adrian Mularczyk, Joey Kloos, Anna Casimiro, Cees Weijers, Sjoukje Lubach, and Nadia Boulif for being open to discuss the results, and for their advise on the experimental work.

Finally, I want to thank my family and friends for their support during my studies and their invaluable advice. I especially want to thank Goan Booij and Luuk Kempen, for their feedback on my work as peers.

Summary

Redox flow batteries are a promising technology for long-term and large-scale storage of electrical energy. However, an improvement in cost of manufacturing and operation needs to be realized in order for them to become viable. The electrodes influence the performance of an RFB to a great extent through the active surface area, which enables the electrochemical reactions, and through its geometry for mass and charge transport.

In this thesis a new manufacturing technique for the electrodes is investigated, which allows control of both the micro- and macrotructure. The 3D structure of the electrode was printed with stereolithography, thermally treated in air at 250 °C for 5 h and in nitrogen at 850 °C for 1 h, and then placed in a redox flow cell. Electrochemical tests in an aqueous cell (Fe^{2+}/Fe^{3+}) and non-aqueous cell ($TEMPO/TEMPO^{+}$) showed that the electrodes enabled the electrochemical reaction to run, proving the great potential of this technique. The results showed that the anisotropicity of the 3D printed structures influenced the performance, for which the electrodes with their printed layers perpendicular to the current collector had the lowest resistance and thus the best performance.

The effect of the thermal treatments on the shrinkage, weight loss, conductivity, and wetting of the electrodes was investigated. A longer dwell time of the oxidation has proven to be beneficial, as it reduced shrinkage and weight loss, while increasing conductivity. A higher temperature in the carbonization greatly enhanced the conductivity. The potential of polymerization-induced phase separation was investigated as technique to control the microporosity of the electrode. The separation and extraction was successful and the surface and porosity had increased. However, several factors, including the induced brittleness, made that the conclusion was drawn that this technique is not suitable to introduce micro-porosity in printed electrodes.

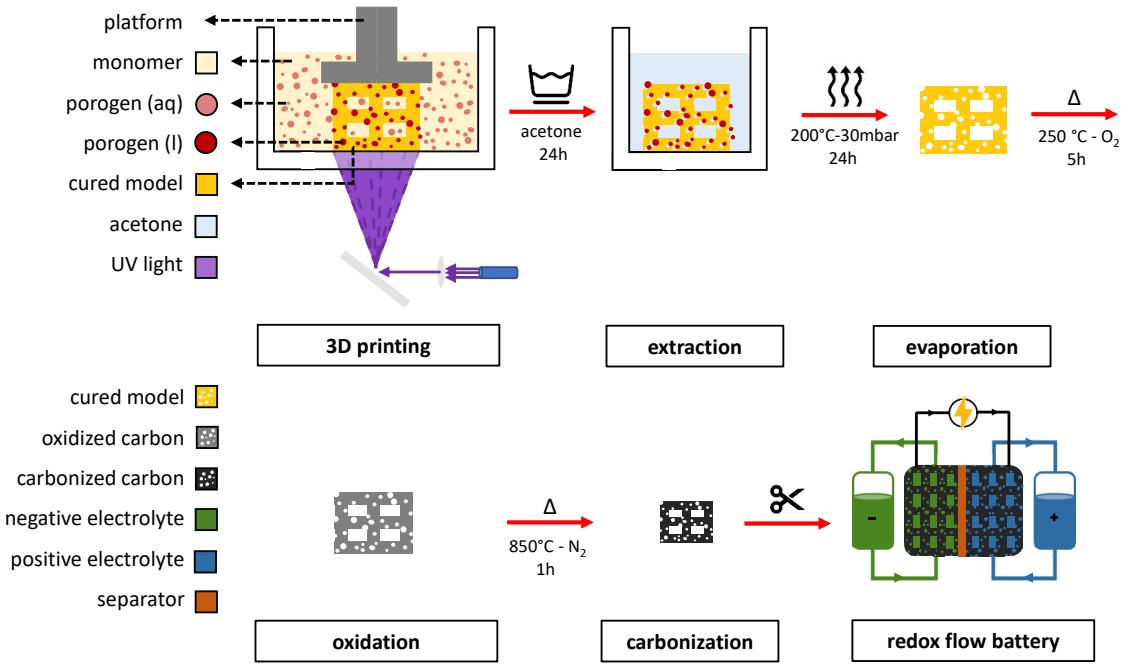

Table of contents

Nomenclature

	symbol	unit	definition
abbreviations	CAD		computer-aided design
	cyclo		cyclohexanol
	deca		1-decanol
	EDMA		ethylene glycol dimethacrylate
	EDS		energy-dispersive X-ray spectroscopy
	EIS		electrochemical impedance spectroscopy
	GHG		greenhouse gases
	HEMA		2-hydroxyethyl methacrylate
	IPA		isopropanol
	OCV		open-circuit voltage
	PETA		pentaerythritol tetraacrylate
	PNM		pore network model
	RHE		reversible hydrogen electrode
	SEM		scanning electron microscope
	SLA		stereolithography
	TGA		thermogravimetric analysis
	UV		ultra violet
	XPS		X-Ray photoelectron spectroscopy
parameters	A	m^2	area
	c	$mol\,m^{-3}$	concentration
	d	m	diameter for circles, edge for squares and triangles
	E	V	potential
	E^0	V	standard reduction potential
	E_0	V	standard cell potential
	E_{cell}	V	cell potential
	E_{eq}	V	equilibrium cell potential
	F	$C\,mol^{-1}$	Faradaic constant, $96\,485\,C\,mol^{-1}$
	f	-	monomer functionality
	G	J	Gibbs free energy
	h	J s	Planck constant
	I	A	current
	i	$A\,m^{-2}$	current density
	i_l	$A\,m^{-2}$	limiting current density
	L	m	length
	n	-	number of electrons transferred or sample size
	P	W	power

Table 1: Nomenclature part 1

	symbol	unit	definition
	p	bar	pressure
	Q	$dm^3\ min^{-1}$	volumetric flowrate
	Q	-	reaction quotient
	R	$J\ mol^{-1}\ K^{-1}$	gas constant, $8.314\ J\ mol^{-1}\ K^{-1}$
	T	°C	temperature
	t	s, min or h	time
	v	$m\ s^{-1}$	velocity
Greek symbols	γ	-	activity coefficient active species
	ϵ	-	porosity
	η	V	overpotential
	ν	s^{-1}	photon's frequency
	ρ	$\Omega\ m$	electrical resistivity
	σ	$\Omega^{-1}\ m^{-1}$	electrical conductivity
subscripts	A		anode
	act		activation
	C		cathode
	$conc$		concentration
	e		electrolyte
	mt		mass transfer
	ohm		ohmic
	ox		oxidized form
	red		reduced form

Table 2: Nomenclature part 2

List of Figures

List of Tables

Chapter 1. Introduction

"It is unequivocal that human influence has warmed the atmosphere, ocean and land. Widespread and rapid changes in the atmosphere, ocean, cryosphere and biosphere have occurred." This is the conclusion of the sixth report on climate change of the UN's Intergovernmental Panel of Climate Change, published in 2021 [1]. Upon use of the fossil fuels coal, oil, and gas, greenhouse gases (GHG) are released in the atmosphere, where they help retain the earth's heat. The resulting increase of GHG concentrations is attributedto be the main driver of the aforementioned climate change. The energy sector is a dominant contributor to this change due to the vast amount of GHG emissions it generates with the combustion of fossil fuels. In 2017, the sector accounted for 66 % of GHG and over 80 % of the CO_2 emissions worldwide [2–6]. To move towards a green energy system with net-zero emissions – as is agreed upon in the Paris Agreement – fossil fuels should be limited and eventually banned by the year 2050 [3, 6–10]. One of the means to realize this is to advance in research on a renewable energy system [3, 7, 10, 11].

The investment costs of renewable energy are declining rapidly – making them viable next to fossil sources. However, most renewable energy sources are irregular and non-dispatchable, causing a partial incompatibility with the traditional electricity grid. The mismatch of the renewable energy generation peaks during the day and the peak loads formed by household consumption during the morning and evening further amplifies this stress on the grid. Sometimes this even results in negative energy prices and disconnection of the renewable energy sources from the grid [10–16]. Hence, a smart solution is needed which can compensate for the irregular electricity generation. One of the possible solutions is energy storage systems. Energy storage systems can integrate the intermittent renewable energy sources with the grid by acting as an intermediate between the two, enabling better control over the dispatch of the generated electricity. To cope with different applications required in the electrical system, such as insurance of power quality on the short term (seconds and minutes), bridging of power gaps on the medium term (hours), and management of energy over the long term (days), various energy storage systems need to be implemented simultaneously [3, 5, 11–13, 17]. Redox flow batteries (RFB) are a promising new technology for large-scale and medium-term energy storage in an efficient, reliable, and sustainable manner. RFBs can operate on the grid (see Figure 1.1) with a discharge duration ranging from hours to a few days and a response time within seconds, making them an ideal bridging technology [11–13, 17–19].

In an RFB, chemical energy is converted to electrical energy and vice versa by means of two reversible redox reactions occurring in two separated half-cells at the same time. An RFB comprises two storage tanks containing the redox species dissolved in an electrolyte solution and an electrochemical stack, consisting of current collectors, electrodes, and a membrane. The solutions are pumped through the stack, upon which the redox species are converted while charging or discharging the battery. The decoupling of power usage (stack size) and energy storage capacity (tank size) in an RFB is a great advantage, as this allows for independent scaling. Furthermore, RFBs have a fast response time, high round-trip efficiency, long durability, and

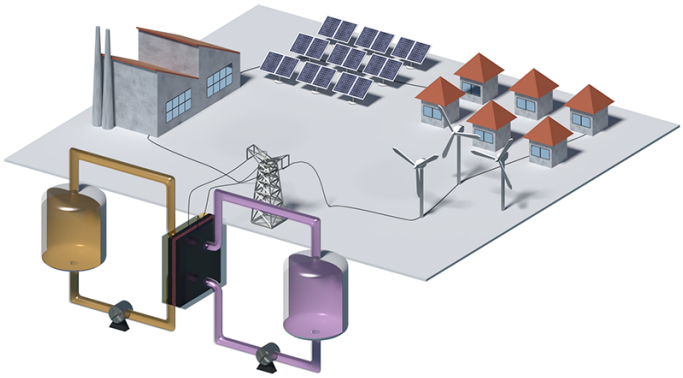

Figure 1.1: RFB connected to the electricity grid: surplus of generated energy can be stored until needed [20].

low environmental impact. They can be operated safely with little management and maintenance needed, and they are not subject to geographical limitations. Additionally, they can be used in a variety of applications, including small storage systems for electric container ships, trucks and airplanes, or large storage systems next to a wind park or solar panel park, integrated in the grid [12, 13, 18, 19]. Unfortunately, RFB systems are currently not implemented at a large scale yet due to financial reasons, despite their promising state of the art. In order to overcome the financial limitations, significant cost reductions must be realized, which can be achieved through advancement in the technology and material development and through the concept of economies of scale. Thus, more research is needed regarding the redox chemistry, material design and reactor design. One of the elements in the RFB which can be improved is the porous electrodes, responsible for the energy conversion [13, 18, 19, 21–23].

The performance of a porous electrode in an RFB is determined by its properties such as kinetic activity, conductivity, active surface area, wettability, and promotion of mass transport of the redox species. Choice of material, structure, and manufacturing technique influence these properties. Carbon is desired as a material because of its high electronic conductivity, high electrocatalytic activity for a variety of redox couples, stability in the electrochemical environment, low weight, natural abundancy, and affordability. The possibility to tune electrical, thermal and mechanical properties by altering the crystallinity, hybridization, and functional groups gives great prospect for further development of carbon electrodes. Other materials, such as noble metals, show good performances as well. However, they are not viable compared to carbon-based materials due to high price and low availability [18, 19, 24–26]. The structure of an electrode affects properties such as mass and charge transport, overpotentials, and reaction kinetics. Ideally, the design should include small pores on the microscale (nm to µm), in order to ensure a high surface area to minimize diffusion distance to the surface and maximize reaction kinetics, and large pores on the macroscale (µm to mm), to minimize pressure drop. A well-designed structure can moreover induce static mixing, which enhances the mass transport of the active species towards the surface. Lastly, the manufacturing technique determines i.e. the conductivity, kinetic activity, and stability of the electrode. Various manufacturing techniques

such as paper making, weaving, needle punching, and hydro-entangling are employed, but they are limited in their control over the final structure – often only one scale can be fine-tuned [18, 23, 27–37]. However, optimization on all scales would greatly enhance electrode performance, as both activation and mass transfer losses can be minimized. Hence, there is a need for a new synthesis and manufacturing technique for carbon electrodes in which great control over the material's properties and the structure on the micro- and macroscale can be realized.

Stereolithography (SLA) based 3D printing offers great potential: the high-resolution manufacturing technique enables the creation of complex, detailed and customized 3D designs with a great variance of materials and functionalities. This can often be realized in only one manufacturing step in an easy, reproducible, and controlled manner [5, 28, 38, 39]. Recent developments in printing on the micrometer scale opened the door for new opportunities for 3D-printed electrodes with macroscale-controlled pores [5, 28]. The conductive functionality required for a 3D-printed electrode can be achieved by printing with a conductive resin or through post-treatment processes, such as applying a conductive coating through electrografting or spray coating or by carbonizing the plastic at high temperatures [24, 27, 35, 40–45]. The last technique, based on the pyrolysis of printed carbonaceous material at a high temperature in an inert atmosphere, is promising. It creates a conductive material, while allowing the properties of the carbonized product to be tailored through variation of pyrolysis and pre- and post-heat treatment parameters [24, 27, 44–46]. Pores on a microscale can be introduced by polymerization-induced phase separation of a porogen – an inert molecule – added to the resin. Induced phase separation is a relatively new but promising technique for the synthesis of porous structures suitable for the application of electrodes, as it enables the control of the microstructure and porosity [20, 47–50].

Aim of this thesis

In this thesis, the possibility to synthesize a conductive carbon electrode with a predefined and optimized structure, controlled porosity, and controlled electrical properties by means of 3D printing, polymerization-induced phase separation, and carbonization is investigated in the laboratory. Separate studies on 3D printing, phase separation, and carbonization are performed first, and their results are subsequently combined to create a 3D-printed electrode. The electrodes are then tested in both an aqueous and non-aqueous battery. This research combines the knowledge obtained on the carbonization of 3D-printed objects [26, 27] with the tunability of polymerization-induced phase separation [47] and applies it to the field of electrochemistry.

This thesis is divided into five chapters. In this chapter a short introduction and brief motivation for the research was given. Chapter 2 provides the theoretical background on RFBs, carbonization of plastic, 3D printing and polymerization-induced phase separation. Chapter 3 contains the description of the conducted laboratory experiments. The results are then presented and discussed in Chapter 4. Finally, the conclusions and an outlook for future work are presented in Chapter 5.

Chapter 2. Theory

In this chapter the theoretical background relevant for this thesis is provided. First, the redox flow batteries are discussed, after which the topics are narrowed down to the electrode, thermal treatments, 3D printing of the macrostructure, and the microstructure from the polymerization-induced phase separation.

2.1. Redox flow batteries

A battery consists of one or more electrochemical cells, used to store and deliver electricity, in which chemical energy is converted into electrical energy (discharging) or vice versa (charging). In an RFB, energy is stored in redox couples (species that donate and accept electrons) dissolved in liquid electrolyte solutions, and is converted when the solutions are pumped through the electrochemical half-cells in the core of the battery, upon which a redox half-reaction occurs at the electrode–electrolyte interface. Electrons and ions are generated in a reduction reaction at one electrode and recombine in an oxidation reaction at the other electrode. The active species (electrons and ions) are transferred at the solid–liquid interface, after which ions are transported by the electrolyte and the separator, and electrons by the conductive electrode and external circuit. Transport of the active species between the half-cells through either the membrane or the electrical circuit closes the system and ensures that the net charge and stoichiometry is preserved. A schematic representation of an RFB can be seen in Figure 2.1. The redox reaction is driven by the potential difference between the two electrolyte solutions and is thus thermodynamically and kinetically controlled. This setup enables an RFB to decouple energy and power, as the energy capacity (kWh) and power capacity (kW) can be independently scaled through respectively the size of the electrolyte tank, choice of active species and concentration of species; and the size of the cells and amount of cells in one stack [13, 18, 19, 22, 51, 52].

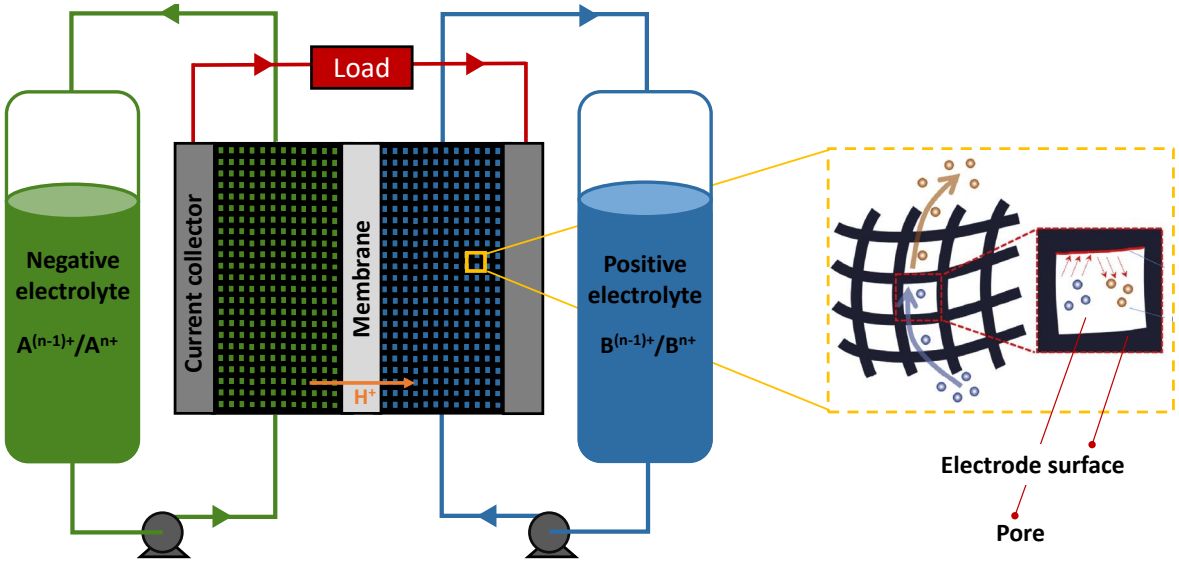

Figure 2.1: Schematic representation of a single-cell RFB, including an illustration of a redox reaction at the electrode's surface.

Redox chemistry

In a redox reaction the oxidation states of the involved chemical species change due to a chemical reaction in which electrons are generated or consumed by molecules and/or ions. The species which decrease in oxidation state generate electrons and undergo oxidation, while the species which increase in oxidation state consume electrons and undergo reduction. The oxidation and reduction half-reactions in the separate half-cells are coupled in one redox reaction via charge transport between the cells, and are thus reciprocal [13, 19, 52–55]. The general mechanism of a single-electron and ion redox reaction is as follows:

$$A^{(n-1)+} \underset{\text{charge}}{\overset{\text{discharge}}{\rightleftharpoons}} A^{n+} + e^- \qquad \text{negative electrode} \qquad 2.1$$

$$B^{(m+1)+} + e^- \underset{\text{charge}}{\overset{\text{discharge}}{\rightleftharpoons}} B^{m+} \qquad \text{positive electrode} \qquad 2.2$$

Each redox couple has an equilibrium state in which the species with the most favorable energy state is formed the most. If electrical energy is added to the system (charging), a non-spontaneous process is started in which the species with the least favorable energy state ($A^{(n-1)+}$ and $B^{(m+1)+}$) will be formed at expense of the species with the most favorable energy state (A^{n+} and B^{m+}). Upon discharge, the reverse will happen spontaneously and the system moves back to the equilibrium state, generating electrons. Only the relative concentrations of the oxidized and reduced form of the active species change during charge and discharge of an RFB; both the oxidized and reduced form of the species are soluble in the electrolyte and no physical transfer of the species occurs at the electrode interface. The tendency of the active species to acquire electrons and thus be reduced is defined relatively to the reversible hydrogen electrode in the standard reduction potential E_0. A higher standard reduction potential indicates a greater affinity of the species towards electrons, which is beneficial for a battery. The difference in the standard reduction potential of the two redox couples used in the adjacent half-cells forms the standard cell potential, E^0, or the equilibrium cell potential, E_{eq}, if reaction conditions are taken into account [13, 19, 51–56].

Components of an RFB

A single-cell RFB consists of a negative and a positive half-cell connected to separate tanks, each with its own redox couple dissolved in an electrolyte solution (Figure 2.1). Both half-cells are connected by a separator, which allows for selective ion transport, by an electrical circuit, which allows for electron transport. The separator prevents the mixing of active species, and is either an ion-exchange membrane or a porous separator, depending on the system used. The active species are dissolved in an electrolyte – an ionic solution due to the presence of a salt, to enable easy transport of ions due to increase ionic conductivity –, which is pumped through the corresponding half-cell. Each half-cell consists of an electrode, a current collector, and optionally

a flow field. The porous electrode enables the redox reactions by means of its electrocatalytic surface, where the active species of the redox couple are converted into another oxidation state by losing or gaining electrons. The current collector transports the electrons between the electrode and the electrical circuit by means of conduction. In simple systems without a flow field, the electrolyte is pumped directly through the porous electrodes. However, the addition of a flow field gives a more efficient operating mode with better mixing, better surface coverage, and lower pressure drop, as it transports the electrolyte both past and through the electrodes, ensuring a better distribution of the electrolyte and a more convective and even turbulent flow. Various flow channel patterns exists. Multiple cells can be combined into one stack in order to increase the power output of the system [13, 19, 22, 51, 52, 54, 55, 57].

A typical RFB system is a liquid–liquid system. Solid–liquid and gas–liquid systems exist as well, but are irrelevant for this thesis. The selection of the redox couple is based on the compatibility between the thermodynamic potentials of both species. Other important factors taken into account for the choice of redox couple and solvent are the electrochemical reversibility of the redox reaction, the energy density, viscosity, and solubility of the solution, and the safety, cost and availability of the components [52, 58]. The solvent used in an RFB can be organic (non-aqueous) or inorganic (aqueous). Aqueous systems are the most commonly used since they have advantageous operating conditions, high ionic conductivity's, and are cheap. An example of an aqueous setup is an Fe^{2+}/Fe^{3+} redox couple dissolved in a HCl solution [22, 52, 59]. However, aqueous systems do face a limitation in the maximum cell potential which can be applied, since hydrogen or oxygen evolution can take place if the cell voltage exceeds $E_{cell} > 1.23\,\text{V}$ vs. RHE [59]. Organic systems are more often used in newly developed systems, as they have a better electrochemical stability and a wider potential window, meaning higher-voltage redox couples can be used, achieving a higher energy density. They also shows larger property flexibility due to the possibility to tailor molecular functionalities. The biggest limitation, besides costs, remains poorer conductivity in comparison to the inorganic systems. An example of a non-aqueous RFB configuration is a TEMPO/$TEMPO^{+}$ redox couple dissolved in acetonitrile [58, 59].

Electrode design

Porous electrodes provide the electrochemical surface for the redox reactions. To increase conversion it is favored that electrodes have a large surface area (A) with a high amount of active catalytic sites, exhibit high and specific electrocatalytic activities, are chemically stable, and wet properly with the solvent. Furthermore, high ionic permeability and electronic conductivity, low contact resistances, and an open structure are desired to reduce ohmic resistances and pressure drop. Large electrode surface area, required for a fast reaction rate, is in trade off with an open structure, needed to decrease pressure drop and increase permeability of the active species, as microporosity (which increases the surface area) impedes convective flow. This not only increases pressure drop, but also results in dead zones and underutilization of the electrode's surface area.

Additionally, the electrode structure dictates the current density distribution and can, under bad design or uneven distribution of reaction zones, give rise to localized hot spots and ultimately electrode degradation [13, 18, 19, 52, 55, 59]. Thus, in order to address these problems and reduce performance losses, special care must be given to the design of the electrode's structure.

Currently, the greater part of electrodes are made of carbon due to its electrocatalytic activity, electrical conductivity, and great variety of allotropes. Furthermore, carbon shows a high stability and durability in electrochemical systems, and has a low price and high natural availability. However, carbon electrodes are also brittle, have a tendency to oxidize, and wet poorly with aqueous solvents. Other materials, such as noble metals, are used as well, but they are more expensive and not always stable [18, 19, 25, 52]. The performance of a carbon electrode varies greatly as function of the allotrope, structure, and manufacturing technique used, as the chemistry of carbon materials has a wide range of possible surface bonds and functional groups [19, 25]. Different carbon-based electrodes exist, including carbon felts, paper and cloths, with porosities (ε) around 0.8–0.9. These electrodes are, however, developed for the fuel cell industry, and are not yet optimized for RFBs. Development of various treatments such as etching, doping, nanoparticle disposition, addition of functional groups, or thermal treatments enhanced the electrocatalytic activities, ionic permeability, electronic conductivity, electrolyte wetting, or surface area of the electrodes for RFBs. However, most of the developments within electrode production or treatment focus on improving either the micro-, meso- or nanoscale, instead of all scales [18, 19, 25, 28, 52, 59].

Transport phenomena within an RFB

Transport phenomena in RFBs consist of charge, mass, momentum, and heat transport. The heat transport lies outside the scope of this thesis, just as the influence of the electric double layer or boundary layer effects due to convection on mass and charge transport. Transport of the charge through the solid components is by means of electron conduction. Mass and charge transport of the dissolved species from the bulk of the electrolyte towards the electrode surface occurs via three main transport mechanisms, namely convection, diffusion, and migration. Convection is caused by a mechanical force which causes a bulk motion, by e.g. pumping or (static) mixing. A stagnant layer forms next to the solid surface of the electrode in which the velocity of the convective flow is very low due to the presence of shear forces. In this stagnant layer – also indicated as the diffusion layer — species are transported from the bulk to the electrode by means of diffusion and migration, induced by respectively concentration and potential gradients. At the electrode surface, the active species are converted, which decreases their concentration and consequently enhances their diffusion. If the conversion of the species is faster than the diffusion of the species, then reactant depletion will occur at the electrode's surface. [52, 54, 55, 57, 60, 61].

Proper control of mass and charge transport is important for efficient operation of an RFB. Within

the battery local differences in species transport can arise, with different surface concentrations, reaction rate, and thus current density on the electrode as consequence. These differences can result in both local dead zones with reactant starvation and local hot spots with potentially harmful high current distributions, and both phenomena are disadvantageous to the performance of the battery. Local differences of species transport can occur at different length scales within the electrode. In small pores with a high surface-area-to-volume ratio, viscous surface forces are dominant over inertial body forces, giving rise to low Reynolds numbers and thus predominantly laminar flow regimes, where mixing is dominated by diffusion. In the large pores containing the bulk of the electrolyte solution convective transport is dominant [62–65]. In order to promote turbulent transport, which is favored over laminar transport, with rather slow mixing and a thicker diffusion boundary layer, static mixing can be introduced [52, 54, 55, 57, 61, 66, 67]. In static mixing, eddies and vortices arise due to changes in fluid streamlines, a change in the boundary layer thickness, and local acceleration and stretching of the fluid. This can be realized by altering the structure of the electrodes, such as split and mixing channels, slanted walls, curvatures, helices, ridges, grooves, and pillars. An advantage of static mixing is that it is a passive method with no operation requirements and low maintenance costs due to the absence of moving parts [62–65, 68]

Performance and limitations

The performance of an RFB is indicated by the energy and power capacity. The power (P) delivered by an RFB is equal to the current (I) times the potential (E) at which it operates, in which the current is equal to the current density (i) times the electrode surface (A). In an ideal and reversible system, an RFB would operate at the equilibrium cell potential E_{eq}, which is thermodynamically the most favorable potential. The equilibrium cell potential is an extension of the standard cell potential E_0, and can be found with the Nernst equation, which includes the concentration of the active species (C_{red}, C_{ox}), activity coefficients (γ_{red}, γ_{ox}), temperature (T), pressure and pH:

$$E_{eq} = E^0 - \frac{RT}{nF} \ln \left(\frac{\gamma_{red}}{\gamma_{ox}} \frac{C_{red}}{C_{ox}} \right) \tag{2.3}$$

where R is the gas constant, n is the number of electrons transferred in the balanced reaction, and F is the Faradaic constant. In practice, the equilibrium cell potential is measured as the open-circuit voltage (OCV), which is defined as the difference in electric potential of electrons at the positive and negative electrodes. This is, however, an approximate value, as the OCV will never truly correspond with the complete thermodynamic equilibrium of the cell due to non-equilibrium thermodynamic effects, such as corrosion or species crossover [52, 54, 55, 69].

When an RFB is in operation an overpotential arises, which causes the battery to operate at a different – and less ideal – potential than predicted by thermodynamics. Hence, an RFB

consumes more energy during charging due to a higher potential, and generates less energy during discharging due to a lower potential than the ideal equilibrium potential. The overpotential is dependent on the current density – meaning that a higher power output of the RFB brings about higher energy losses. The energy is lost in the form of heat. The overpotential is classified by three main contributors: activation losses (η_{act}), ohmic losses (IR_Ω, and concentration losses (η_{conc}). The activation overpotential is dominant primarily at lower current densities, the ohmic overpotential at intermediate current densities, and the mass transfer overpotential at high current densities (Figure 2.2) [13, 52, 54, 55, 70]. The actual potential at which an RFB operates, taking all the losses into account, is defined according to Equation 2.4 for discharging and to Equation 2.5 for charging.

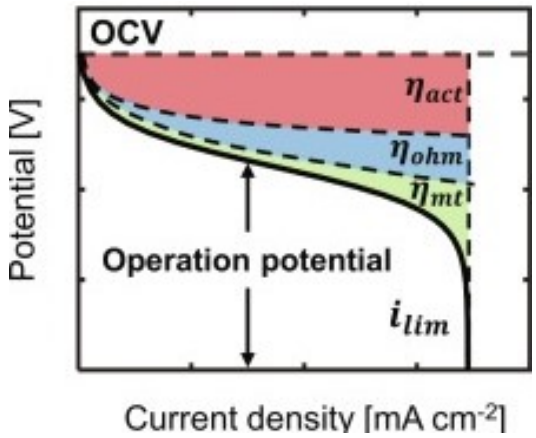

Figure 2.2: Example of a polarization curve of an RFB in discharge mode, including different overpotential contributions [71].

$$E = E_{eq} - \eta_{act,C} - \eta_{conc,C} - \eta_{act,A} - \eta_{conc,A} - \sum IR_\Omega \quad (2.4)$$

$$E = E_{eq} + \eta_{act,C} + \eta_{conc,C} + \eta_{act,A} + \eta_{conc,A} + \sum IR_\Omega \quad (2.5)$$

Activation losses are caused by the activation energy required to transfer charge at the solid-liquid interface between the electrode and electrolyte. Activation losses can be reduced by using an electrocatalyst, or by operation at higher temperatures [13, 52, 54]. Ohmic losses comprise all the ionic and electronic resistances in the cells, including the resistance of ionic transport through the electrolyte and membrane, electrical transport in the electrode and circuit, and the resistance of the contact between cell components (also known as junction overpotentials). This relation is therefore a summation of all the resistance elements multiplied by the current. Additional energy is needed to overcome those resistances [13, 52, 54, 55]. Concentration losses are mass transport related losses, and are dictated by the depletion of the electroactive species at the electrode surface. This depletion occurs when the rate of the redox reaction of the species at the electrode surface is much faster than the rate of mass transport of the species from the bulk towards the surface. In this case, the rate of transport becomes limiting and is measured as the limiting current density (I_L). The concentration overpotential can be minimized by increasing the surface area of the electrodes or the species' conductivity in the electrolyte, or by improving mass transport. The latter can be realized with higher flow velocities, the use of flow fields, or by introducing of static mixing. [13, 52, 54, 55, 66, 67].

Additional events in the system induce operation losses as well. These include shunt currents (when electric current deviates from the intended path to a parallel path with sufficient low resistance), crossover of active species to the other half-cell through the separator, high pressure drops and hydraulic losses, dead zones in the electrode, and self-decomposition, degradation or precipitation of the material or active species used. Poor thermal management, poor electrode wetting or incomplete conversion of active species impose challenges as well. Development of better materials, process and cell design used in the batteries hopefully will reduce these overpotentials [19, 52, 70, 72].

2.2. The effect of heat: oxidation and carbonization

Electrocatalytic activity and conductivity can be introduced in a polymer by means of thermal treatment at an elevated temperature (50–1100 °C) in either a non-inert or inert environment (with or without oxygen, respectively). Thermal treatments also affects other properties of the polymer, including the weight, length, density, elasticity, mechanical strength, hydrophilicity, and surface area [24, 26, 27, 73–75]. These changes arise due to alterations in the carbon structure or chemistry induced by the heat: the ratio of aromatic or graphitic (sp^2 hybridized) to tetrahedral (sp^3 hybridized) regions and the ratio of crystalline to amorphous regions changes, and functional groups can be converted. Higher sp^2/sp^3 hybridization ratios give a more graphitic and thus more conductive material [26, 73, 74, 76–78]. Processes occurring during thermal treatment of a polymer include evaporation of unreacted species (distillation), decomposition of weak hydrogen, ionic, or weak covalent bonds, and the scission of strong covalent bonds in the matrix. The latter two mechanisms create (radical) reactive groups that can react with other polymer groups (crosslinking) or with oxygen and hydrogen atoms (oxidation and hydrogenation). Fragments which do not react are evaporated out of the polymer matrix. Thermal treatment can be classified into oxidation (non-inert atmosphere), which can result in combustion, and carbonization (inert atmosphere), which gives rise to pyrolysis and pyrosynthesis [73, 75, 76, 78]. Both will be discussed next.

Oxidation

Thermal oxidation causes oxidative crosslinking of the polymer matrix, increasing the stiffness and brittleness, and the addition of oxygen functional groups on the surface, increasing the hydrophilicity (wetting), and the catalytic abilities of the material [73, 76]. The transformations occurring in the polymer result from complex interactions between oxygen and the matrix and within the matrix itself, and are influenced by factors such as temperature, oxygen levels, ramp rate, dwell time, and catalytic surface [73–75, 79]. During thermal treatment in air, oxygen reacts with surface groups of the polymer, and either adds onto the surface (oxidation, at low temperatures), or splits and degrades the product into gases (combustion, at high temperatures). The different degradation patterns at higher temperature give rise to various radical products,

which can react with other functional groups, polymer chains, and oxygen or hydrogen atoms, resulting in a range of products. The temperature of the process determines the extent of degradation of the carbon-based species, and at very high temperatures only oxidized gaseous products such as CO_2, CO, H_2O and NO_x are formed [75, 79]. At low temperatures, oxygen-based functional groups are formed on the polymer by processes such as transesterification reactions, formation of ketones, hydrogen donor and acceptor interactions between alcohols and esters, or the formation of hydrogen bonds [47].

Carbonization

Carbonization is a complex process of concentrating and purifying carbon by destructive distillation of organic matter, which entails breaking and re-arranging bonds at high temperatures in inert conditions. Carbonization consists of four coincident and partly competing phases. The first phase is distillation (~100 °C), in which heat evaporates the freely moving volatile and semivolatile hydrocarbons into the gas phase. The second phase is pyrolysis, in which carbon–carbon bonds are broken by excessive heat, creating increasingly smaller and lighter hydrocarbon gases. Thermally unstable regions within the polymer matrix can be cleaved, causing cracks and deformation. The third phase is pyrosynthesis, in which excessive heat breaks larger carbon molecules into small reactive molecular fragments, which either evaporate or react and form an increasingly condensed polymeric network of aromatic carbon (coke). If the temperature surpasses 1300 °C, then crystal structures are formed next to the aromatic regions of the carbon, which indicates movement and rearrangement of atoms within the matrix. Above 2000 °C only crystal structures are formed, resembling graphite. The extent of the effect of the pyrosynthesis phase on the carbon structure can be seen in Figure 2.3. The fourth phase is condensation, in which the vapor phase cools down and the volatile and semivolatile hydrocarbons condense to stable gases (methane, ethane, acytelene, etc.), liquid pyrolytic condensate (tar), or solid

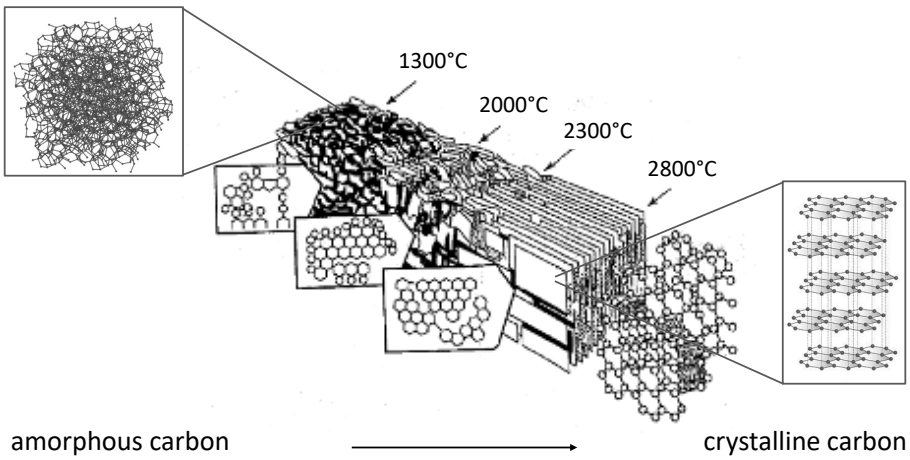

Figure 2.3: Schematic representation of the carbon structure formed during the pyrosynthesis phase of the carbonization, in which a higher temperature results in a more crystalline and graphitic structure. Adapted from Hardyal [77].

pyrolytic condensate (soot). Thermally stable coal minerals bound by graphitic carbon (coke) remain as product after carbonization [77, 79]. Literature studies on carbonization report that higher temperatures result in a more graphitic carbon with lower electrical resistivity, slightly higher loss of mass, higher linear shrinkage, and higher structural density. A longer dwell time and slower ramp rate allows for more rearrangement of carbon atoms in a gradual manner and more annealment of the carbon matrix. This leads to less mass loss, less shrinkage, less trapped gases, and consequently a larger structural density with more graphitic areas and a smoother surface with a lower surface area [24, 26, 74, 77]. The linear shrinkage occurs due to evaporation of the gaseous products formed and due to the crosslinking of the matrix [24, 79].

2.3. 3D printing

3D printing is a relatively new but rapidly developing technology used to manufacture products with a high variety in material type and purity, printing accuracy and complexity, and the product's strength, flexibility, and conductivity. 3D printing makes use of computer-aided design (CAD) software which enables one to create a 3D product as intricate as desired [38, 80]. The used manufacturing technique (jetting, extrusion, fusion, photopolymerization, sheet lamination, direct energy deposition) and materials (inks, metal, plastics, ceramics) have great influence on the properties of the product and on manufacturing parameters (e.g. layer thickness, resolution, build volume, and build speed) [28, 38, 80–82]. Another important property of a 3D-printed material is its anisotropicity, which is the quality of that properties have different values when measured along different axes. Anisotropicity arises when there are differences in the structure in the horizontal and vertical direction of the printed part [83]. This property is relevant for printing techniques that build their print layer-by-layer, in which one layer is printed horizontally (XY plane) and multiple layers are printed on top of each other in the vertical (Z) direction. High anisotropy indicates little fusion between adjacent layers, which reduces the product's mechanical strength in the Z direction spanning multiple layers. In order to lower the anisotropicity, strong chemical bonds (e.g. ionic or covalent) must be realized between the layers. The prints becomes isotropic if a high degree of covalent bonds between the layers results in a structure that exhibits no difference in the mechanical strength (or other properties) between the XY and Z directions [28, 80, 84, 85].

The goal of this research is to print a conductive carbon-based electrode with high resolution and great porosity spanning the macro- and microscale. This can be achieved by printing with a resin mixed with an inert porogen (particles with a specified shape or size used to make pores in a molded structure), after which the printed electrode is subsequently carbonized. Hence, three requirements for the printer must be met to fabricate such electrodes using 3D printing: it must use a carbon based resin, the porogen must be compatible with the resin (i.a. inert and miscible), and the crosslinked polymer should be able to hold its shape when carbonized (i.e. a thermoset).

Material extrusion, material jetting and vat-photopolymerization make use of a plastic resin

used in a liquid phase, so they meet the given requirements. The first method operates using mechanical forces and the last two opeare using a high-power electromagnetic force (light beam) [28, 38, 80–82]. Material extrusion heats and deposits a plastic or filament in the correct shape in a layer-by-layer fashion. It is a fast and cheap method with a large choice in available resins, but it also renders rough surface products with high anisotropicity and limited detail. Furthermore, material extrusion makes use of thermoplastics to melt and shape the material, which means it is not able to hold shape during carbonization. Thus, this technique is not suitable for this application. Vat-photopolymerization and material jetting give a smooth finish, high resolution, high mechanical strength, and high fusion between adjacent layers due to the formation of chemical bonds and crosslinks in the printing process. The high degree of covalent bonds between layers results in a less anisotropic or – depending on the apparatus and resin used – even an isotropic print. Resins comprising of monomers with high functionality ($f \geq 3$) favor synthesis of a thermoset due to the high degree of crosslinking [27, 28, 39, 78, 82, 85, 86]. However, both techniques have disadvantages as well, including limited choice in available resins (and thus less possibility to fine-tune the material's properties), slow printing rate, possible shrinkage during polymerization, use of hazardous resins, and an UV sensitive polymer product, with possible degradation of the material as consequence. Vat-photopolymerization requires an additional post-processing step due to the required supports on the print. Material jetting, on the other hand, performs worse in terms of resolution and mechanical strength compared to vat-photopolymerization, and has is even more limited in material choice due to the additional resin viscosity requirements [28, 38, 39, 80–82, 86, 87]. Overall, vat-photopolymerization is the most suitable technique for our design case: it meets all the requirements, it performs better in terms of resolution, strength, and material selection than material jetting, and its disadvantages such as slow printing rate and the requirement of post-processing can easily be overcome.

Stereolithography

The most used vat-photopolymerization technique is stereolithography. In SLA, a photocurable resin is solidified upon irradiation with an ultraviolet (UV) light beam that supplies the required energy to initiate a chemical reaction between monomers, forming a polymer (also known as curing). The chemical reaction commonly used for SLA is an acrylate-based free radical chain growth polymerization. The photoinitiator added to the resin generates free radicals upon exposure to light with a wavelength to which it is reactive, upon which the radicals react with the double bonds of the acrylate monomer in an additive manner, creating a radical monomer. The radical monomer then reacts with another monomer to form a polymer chain, and the radical is transferred to the added monomer. This reaction propagates, allowing the polymer chain to grow in length. Termination of the polymerization reaction arises from chain combination, disproportionation, or transfer. The mechanism of this reaction with a methyl methacrylate monomer can be seen in Figure 2.4 [38, 78, 81, 88].

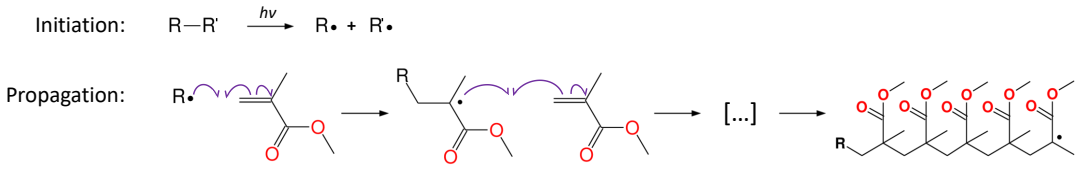

Figure 2.4: Free radical chain growth polymerization of methyl methacrylate towards poly(methyl methacrylate) using an unspecified photoinitiator. Ultraviolet light is indicated with $h\nu$. Adapted from Mazzucco [88]

By choosing a different acrylate monomers the material properties of the print can be influenced (e.g. mechanical strength, flexibility and temperature resistance). For example, monomers that can crosslink due to their high functionality (i.e. number of bonds that one monomer can form) can be used to increase the mechanical strength of the product in all directions and reduce the anisotropicity, but they can induce brittleness, higher shrinkage, and non-uniformity as well. Monomers with higher molecular weights, on the contrary, can reduce shrinkage and brittleness due to their lower reactive group concentration, but they increase the viscosity and might require heating during printing. The addition of functional groups can be used to introduce specific properties. Urethane groups, for instance, are able to align polymer chains via hydrogen bonding, creating crystalline regions. The monomers chosen for the resin should, however, at least be compatible with the SLA system used, meaning that vat life, viscosity, glass transition temperature, and reactivity need to fall within the appropriate operating ranges [81, 86, 89, 90].

A typical SLA machine comprises a tank containing the liquid resin, a movable platform upon which the print is built, a recoater blade, and an UV light generator and processing system (Figure 2.5). The CAD model is first converted to a print model by a software which slices the CAD model into independent binary images, including the printing path of the laser for each layer. During the printing process the light beam is focused with lenses and mirrors, and is scanned along the desired pathway in the XY plane given by the software, polymerizing a single layer of the product. After one layer is printed, the platform is lifted up in the Z direction, a new layer of resin is swept over the tray, and the platform is lowered again to one layer thickness above the previous printing position. Then, a new layer is formed in a similar fashion, and the process is repeated until the print is finished. A monomer conversion between 65–90 % ensures that the polymerization reaction is not driven to completion yet after one layer is printed, creating a semi-reacted state between two adjacent layers. This state allows for the formation of polymer chains between the two layers, resulting in a high degree of covalent bonds in the Z-direction and thus reduced anisotropicity. The high degrees of covalent bonds within one layer and between adjacent layers together create a strong, dense, and sometimes even isotropic product [38, 80, 85, 89, 91, 92]. Since the resin does not completely cure during the SLA process, a post-processing step is required. This comprises of washing the print with a solvent to remove unreacted resin, and treating it with UV light and heat to cure unreacted sections [38, 80, 93, 94].

Process parameters such as the spot size (wavelength, focal length, and aperture) and penetration

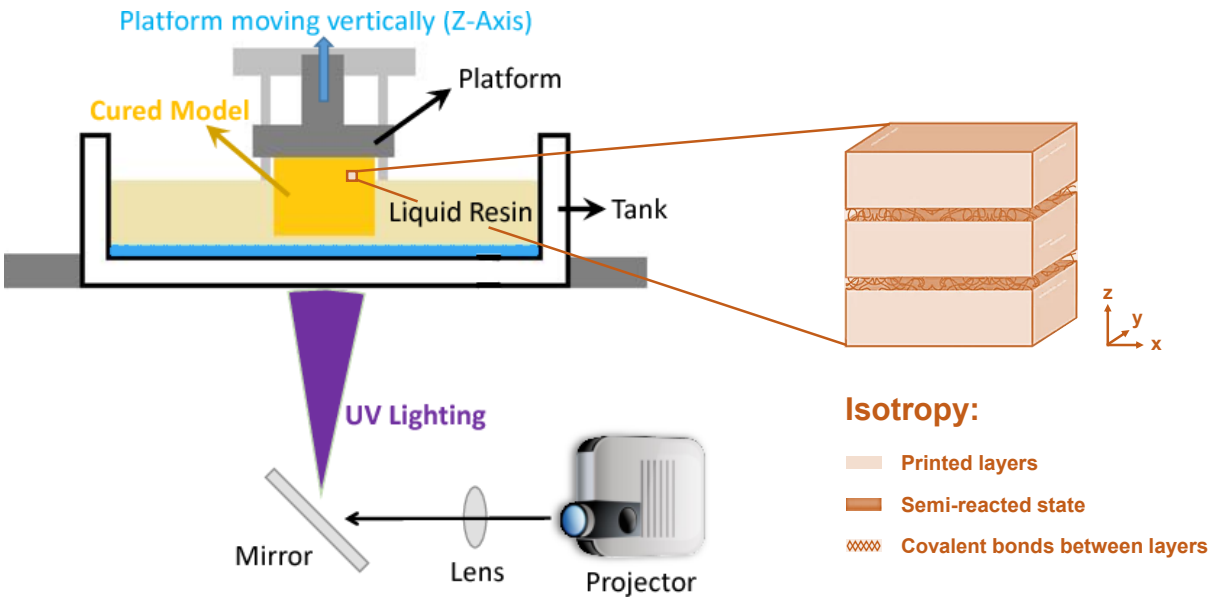

Figure 2.5: Schematic representation of the SLA 3D printing process and the isotropy between adjacent layers. Adapted from Xometry Europe [91] and Formlabs [85].

depth (power and exposure time) of the laser, hatch style and spacing, scanning speed, sweep period, layer thickness, and orientation of print affect the quality of the print. Most of these parameters are already defined by the printer used, but layer thickness and orientation of the print can be adjusted. A coarser set layer thickness will reduce the print time but will also decrease the surface quality and the resolution. The orientation affects the amount of support and number of layers required and thus influences the print time. The orientation also affects the direction of anisotropicity of the product, as the layers printed parallel in the XY plane have the highest lateral mechanical strength and the most dense (crosslinked) network [38, 86, 95].

2.4. Polymerization-induced phase separation

While 3D printing does provide control of the macrostructure, it does not allow for control over the microstructure due to limited printer resolution. Surface modifications, such as treatment of a 3D-printed electrode with chemicals, irradiation, or heat, can be used to increase the surface porosity [18, 35, 43, 46, 96]. Fabrication methods used in the field of polymer membranes can also be used to created micropores and thus increase the surface area. Of those methods, induced phase separation is applicable to our setup: a porogen can be added to the monomer mixture, and upon polymerization a three-component mixture arises, which spontaneously undergoes phase separation [47, 97–99]. During the polymerization the polymer is solidified around porogen agglomerates, creating a polymer matrix. This process is caused by the separation of the porogen, which has a high solubility towards the monomer and a low solubility towards the polymer, out of the monomer–polymer mixture as the monomer concentration decreases and polymer concentration increases. This process gives rise to a matrix with a liquid porogen phase encapsulated by a solid polymer phase (Figure 2.6). The liquid porogen phase can be extracted out of

the polymer matrix by washing with a solvent in which the porogen dissolves, but the polymer does not. Subsequently, the solvent and dissolved porogen are removed from the polymer matrix by evaporation. This results in a macroporous polymer matrix of which the size and distribution of the pores correspond to the size and distribution of the porogen agglomerates in the mixture (Figure 2.6) [27, 47, 97, 99].

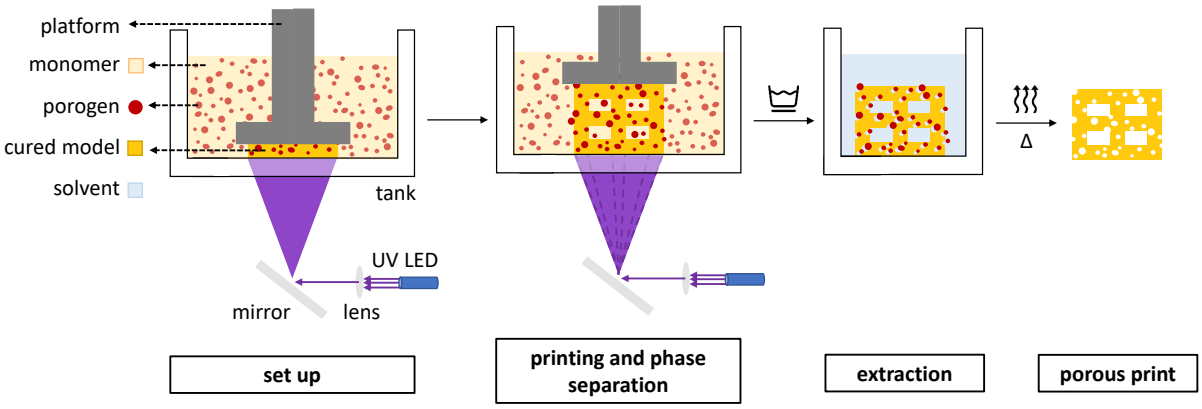

Figure 2.6: Schematic representation of a polymerization-induced phase separation whilst 3D printing, followed by a porogen extraction by washing it with a solvent, and a solvent evaporation at elevated temperatures under vacuum.

The microporosity can be controlled with the choice of porogen and the concentration of the porogen in the resin, as it acts as a direct template of the pores obtained in the final product. A porogen concentration results in a more porous polymer product with a higher surface area, but also a lower density and a lower mechanical strength. The choice of monomer influences the process as well, as the interaction with the porogen and the polymerization kinetics dictate the course of the phase separation. A ternary diagram based on the Flory–Huggins solution theory can give insight in the ease and course of the phase separation and the final polymer matrix. The porogen should be chosen such that it is inert to both monomer and polymer, and that it can easily be extracted from the polymer phase [27, 47, 100].

Chapter 3. Methods and Materials

This chapter summarizes the conducted laboratory experiments. First, the materials and methods used in general are given. Then, the scientific procedures used for each step in the synthesis of the electrodes are elaborated upon, which are polymerization-induced phase separation, 3D printing, and thermal treatments. Finally, the preparation and operation of both a non-aqueous and aqueous symmetrical redox flow cell with the synthesized electrodes is explained.

3.1. General experimental procedures

Surface and elemental analysis

The structure and morphology of the surface and cross section of the prepared samples were examined with a scanning electron microscope (SEM), which is able to produce high resolution images on micrometer and nanometer scale. An elemental analysis was done with energy-dispersive X-ray spectroscopy (EDS) and X-ray photoelectron spectroscopy (XPS), which gave insight in the elemental content of a sample. For the SEM and EDS a JOEL JSM-IT100 was used, for the XPS a Thermo Fischer Scientific K-Alpha. The non-conductive samples were coated beforeanalysis with a thin layer of platinum using a JEOL JFC-2300HR for a duration of 60 seconds and at a pressure (p) of 40 mbar. The SEM images were subsequently analyzed with the software ImageJ, using the threshold and measuring tools. Unfortunately, elemental measurement techniques such as nuclear magnetic resonance spectroscopy, gas chromatography and infrared spectroscopy could not be used on the carbonized samples, because they are not soluble and are conductive.

Thermal analysis

A thermal gravimetric analysis (TGA) was used to assess the material's thermal stability and the mass degradation behvarior over a temperature range. The TGA was performed using a PerkinElmer TGA 4000 apparatus or using a TA's instruments TGA Q500 with a ramp rate of $10\,^{\circ}\mathrm{C\,min^{-1}}$ and an O_2 or N_2 gas flow of $20\,\mathrm{mL\,min^{-1}}$.

Assessment of samples' weight and size

The weight, size, and volume of the samples were measured before and after the synthesis steps. The weight was measured with a Sartorius CPA3245S lab scale, which has a repeatability of ± 0.2 mg [101]. The size of the entire sample was determined by analysis of photographs, taken with a smartphone or with the TOOLCRAFT USB microscope, with ImageJ. The volume (and inherently the density) was measured using of the suspension method, in which Archimedes' principle is applied [102]. This method is explained in Appendix A.

3.2. Photopolymerization, induced phase separation and extraction

The principles used in the experimental set-up for the polymerization-induced phase separation

and carbonization are based on the work of Steldinger et al. [27] and Dong et al. [47].

Resin composition

The photocurable resin consists of (a number of) monomers, porogens, and a photoinitator. 2-Hydroxyethyl methacrylate (HEMA), ethylene glycol dimethacrylate (EDMA), and pentaerythritol tetraacrylate (PETA) (all from Merck chemicals) were used as monomers, which respectively have functionality of two, four, and eight in the polymerization. The inhibitor was not removed from the monomers, as the polymerization proceeded successfully without removal. Cyclohexanol (from Merck chemicals) and 1-decanol (made in house) (in the sample codes referred to as cyclo and deca respectively) were used as porogen. Phenylbis(2,4,6-trimethylbenzoyl)phosphine oxide (Irgacure 819) was used as photoinitiator. The structural formulas of the chemicals used can be seen in Figure 3.1. The resin contained 0–30 wt% porogen and 4 wt% photoinitiator with respect to the monomers. The components were weighed and mixed together into a resin in amber sample vials. The resin was sonicated in Branson 5510 sonication bath for 30–60 min to obtain a clear and homogeneous mixture. The resin was stored in a refrigerator and sonicated again before each use.

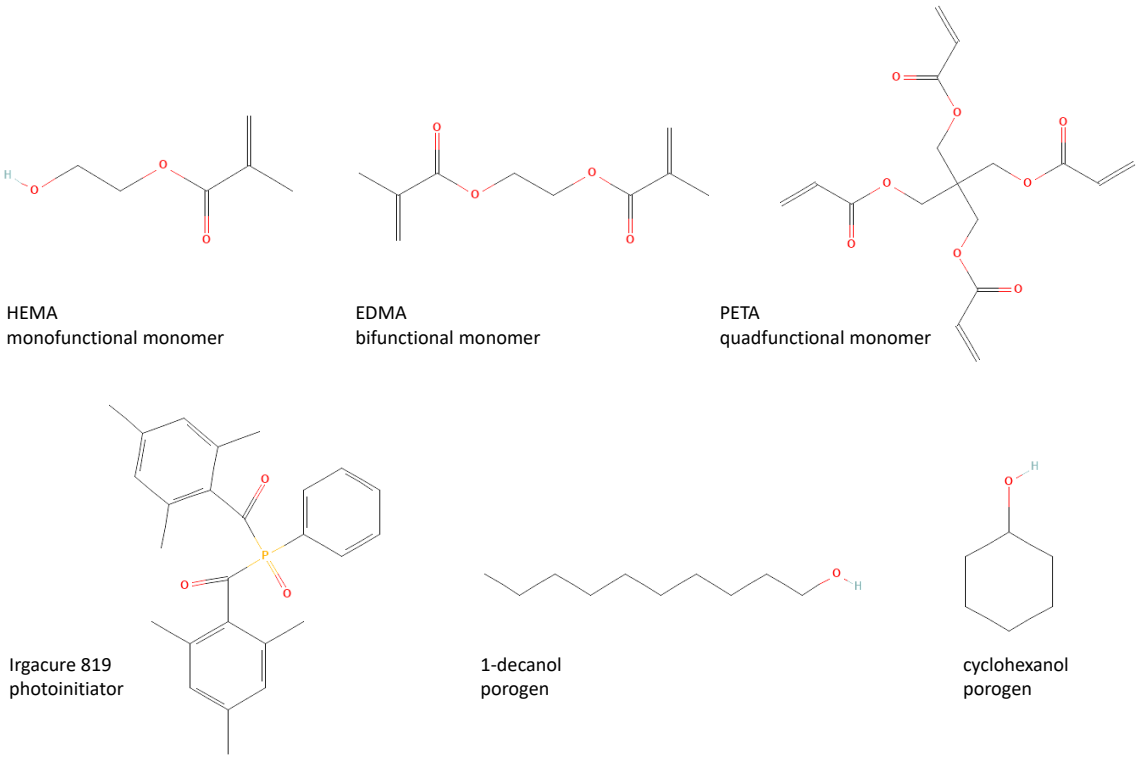

Figure 3.1: Structural formulas of components used in the photocurable resin,

Photopolymerization with induced phase separation and porogen extraction

The polymerization was performed with a 405 nm lamp and LED controller from THORLABS. The light was placed in a black box inside a fume hood. A few droplets of the resin were pipetted

on a cleaned glass plate inside this box, after which the polymerization and phase separation took place when the resin was illuminated by UV light. The cured plastic sample was removed from the glass and put in a sealed reagent bottle filled with the washing solvent (acetone, isopropanol (IPA), ethanol, or xylene) for 24 or 48 h on a rolling bench. The extraction of the porogen and solvent was then realized by means of a vacuum oven (Memmert) under various conditions.

3.3. 3D printing

To differentiate between identical looking samples, design elements such as text or shapes were added such that it would not compromise comparison to the other samples.

Form 3 printer

The samples were printed with the 3D printer Form 3 of the company Formlabs, which uses the SLA technology. It is equipped with a laser with a wavelength of 405 nm, a power of 120 mW and a spot size of 85 µm, which results in a XY printing resolution of 25–300 µm and a Z resolution of 25 µm [103]. The laser is supported by a Light Processing Unit comprising of a system of lenses and mirrors, which enables the printer to print accurate and repeatable prints [93]. The digital models for the printer were created with AutoCAD software and were imported to the printer with the PreForm software. The print resolution in the Z-direction was set in PreForm to 25 µm, which is the highest possible resolution. The resin High Temp V2 was chosen as commercial resin due to the properties it has as a thermoset, which enables the printed samples to keep their shape upon heating. The resin is composed of the following trade secret components: a methacrylate monomer (25–45 wt%), acrylate monomer (45–65 wt%), urethane dimethacrylate (7–10 wt%), and a photo-initiator (<0.9 wt%) [104].

The post-processing is done with the Form Wash and Form Cure of Formlabs and is based on the advise given by Formlabs for the High Temp V2 resin [105, 106]. The printed samples were removed from their support platforms and were washed in IPA for five minutes. If required for the experiment, the sample was cured under UV light at a temperature of 80 °C for three hours.

Printer's performance

The performance of the 3D printer is measured for printed pins and holes with a square and circular shape on plates with a thickness of 0.1–0.5 mm. The pins had a diameter of 80–250 µm and the holes of 250–1000 µm. The pins and holes of equal size were printed with a spacing of 100 or 500 µm. The accuracy of the printed elements was determined with a visual analysis in the SEM combined with ImageJ, in which the diameters of the printed pins and holes were compared to the set diameter in the digital CAD models. The precision of the printer was found with the standard deviation of the average diameter of multiple printed pins and holes. The sample size of the printed elements varied from $n = 12$ to $n = 80$, depending on how much of the elements would fit onto one plate. The highest resolution possible for the printer was based

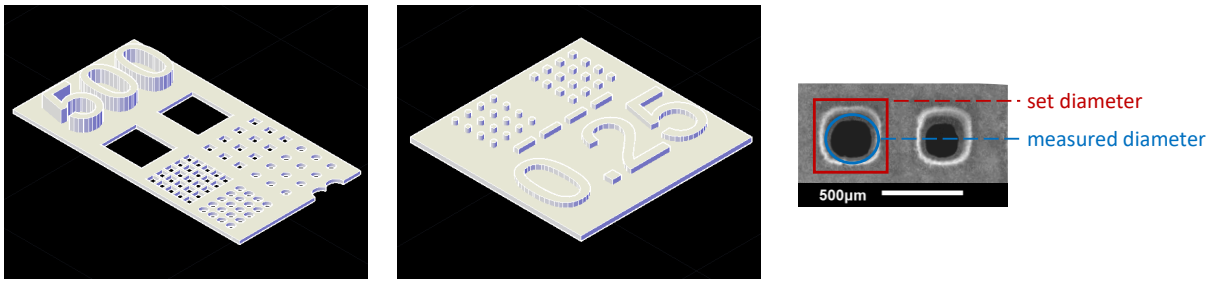

Figure 3.2: Analysis of the performance of the 3D printer. On the left and in the middle there are two CAD models of plates with printed square and circular holes and pins respectively. On the right an example of an ImageJ analysis of a SEM image of printed holes is given

on the measured accuracy of the printed rods and holes. A printed hole was deemed successful when the diameter deviated not less than 50% (arbitrarily chosen) of the set diameter. Hence, (partially) were indicated unsuccessful. In this way, the highest possible resolution for the holes and rods could be determined. An example of the CAD models and the image analysis can be seen in Figure 3.2. Lastly, the effect of the post-process treatments (washing and UV-curing) and print orientation (horizontal and vertical) were analyzed visually in the SEM.

3.4. Thermal treatments

The plastic samples undergo two to three thermal treatments before they can be used as a conductive electrode, namely an oxidation, a carbonization and another oxidation. The optimal duration and temperature of the those treatments were tested with open structured samples printed with the High Temp V2 resin. A TGA on the material was performed so to assure safe operating conditions and to confirm that the material is able to carbonize without 100% mass loss. Unfortunately, the tubular oven used for the carbonization went out of function during this thesis, so only a limited amount of electrodes could be carbonized and tested.

Equipment and methods

The samples for the heat treatment experiment were printed with the High Temp V2 resin in square 3D grid structures with 0.1 mm rods thick and 1 mm holes (see Figure 3.3). However, the study on the resolution of the Form 3 revealed that the rods are printed with a diameter of on average 237 µm, so set diameter of the rods in reality will be larger. The carbonization requires an open structure, since trapped gas will explode out of dense structures, leading to severe deformations. Various shapes surrounding the grid structures were used to differentiate between pre-treatments. The diamond shaped prints were only washed, the squares washed and UV-cured, the circles washed and oxidized, and the rectangles washed, UV cured and oxidized (Figure 3.3). The duration of the oxidation was indicated with additional square grid extensions, in which one extension represented one hour of thermal treatment.

In the first oxidation step a Memmert oven at 250 °C under atmospheric air was used for 1–5 h.

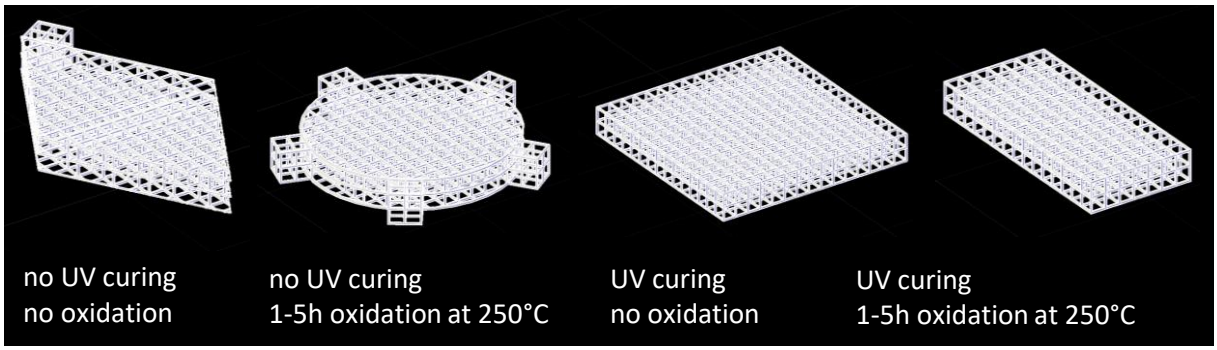

Figure 3.3: CAD model of four samples that undergo a different treatment before carbonization

For the carbonization step the tubular oven Carbolite TZF 12/75/700 was used, flushed with nitrogen at a temperature ranging from 650 to 850 °C for a duration of 1 to 5 h. The maximum temperature of 850 °C was defined by the oven. The accuracy of this furnace was not optimal, since an overshoot of 10 °C or a different ramp rate could easily occur. For the second oxidation step a Naberthem muffle oven model C290 or P300 was used at 450 °C for 0.5–12 h under air. All heat treatments had a ramp rate set to 10 °C min^{-1}.

Sample analysis

The oxidized and carbonized samples were first examined in terms of change in dimension, weight, volume and density. Unfortunately, it was not possible to perform the measurements for the volume and density of the carbonized samples; the density was lower than the density of water or IPA, so the samples did not sink. Other volume measurements such as the overflow or level method also could not be used, since they require immersing the sample in a liquid as well.

The wetting of the samples was investigated qualitative by placing the samples in small vials filled with water or acetonitrile on a rolling bench. After 1 h and 24 h the wetting of the sample was checked visually, in which the wetting was assessed as 'good' if the sample sunk. A quantitative contact angle measurement was not possible due to the grid structure of the samples; the small holes altered the shape of the droplets significantly.

The electrical conductivity of the carbonized samples could roughly be determined by measuring the electrical resistance upon an applied current. To do so, the sample was placed on top of two measuring leads (gold) connected to a Voltcraft VC130-T resistance meter (see **??**). A non-conductive sample was placed on top to ensure proper contact. The average resistance, measured as the applied voltage over the applied current, was defined as the electrical resistance (R) of the sample. The material's conductivity (σ) is the inverse of the material's electrical resistivity (ρ), which is related to the resistance. As can be seen in Equation 3.1, this relation includes the length and the cross sectional area of the sample. However, even though the measuring leads are located at a defined spacing, it is not possible to control the length and area due to the curvature and grid structure of the samples. Hence, this method can only be used qualitatively to obtain an indication of the conductivity. Better measurement techniques, such as using crocodile beaks,

could not be performed due to the brittleness of the samples.

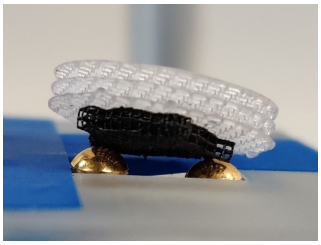

Figure 3.4: Conductivity test of a carbonized sample placed on two golden leads connected to a resistance meter

$$R = \rho \frac{l}{A} = \frac{V}{I} \tag{3.1}$$

$$\sigma = \frac{1}{\rho} \tag{3.2}$$

Lastly, a study was done to the limitations with the carbonization of plastic thermoset samples. Different shaped samples were carbonized for 1 h at 850 °C and were visually checked for shape deformations due to an explosion of trapped gas. The variation in shape included dense plates with thickness varying from 0.1 to 1.0 mm, square grid structures with a 1.0 mm wide hole and square rods varying in thickness from 0.4 to 1.5 mm, and square grid structures with holes with a width from 0.5 to 1.3 mm with square rods of either 0.3 or 0.4 mm in diameter.

3.5. Electrochemical tests

Shape and structure of the electrode

The shapes and structure of the printed electrodes were varied so that the effect of induced mixing could be studied. Four different shapes were used for the rods in the square grid structure: square, circular, triangle and square with a helical twist (Figure 3.5. The diameter of the rods and the holes in the grid were designed in such way that the surface area and the electrode porosity were equal for each electrode. This was done based on a calculation, provided in Appendix A. Furthermore, square grid structures with square rods were printed in a horizontal, diagonal and vertical fashion, so that the effect of the anisotropicity of the print can be evaluated. The

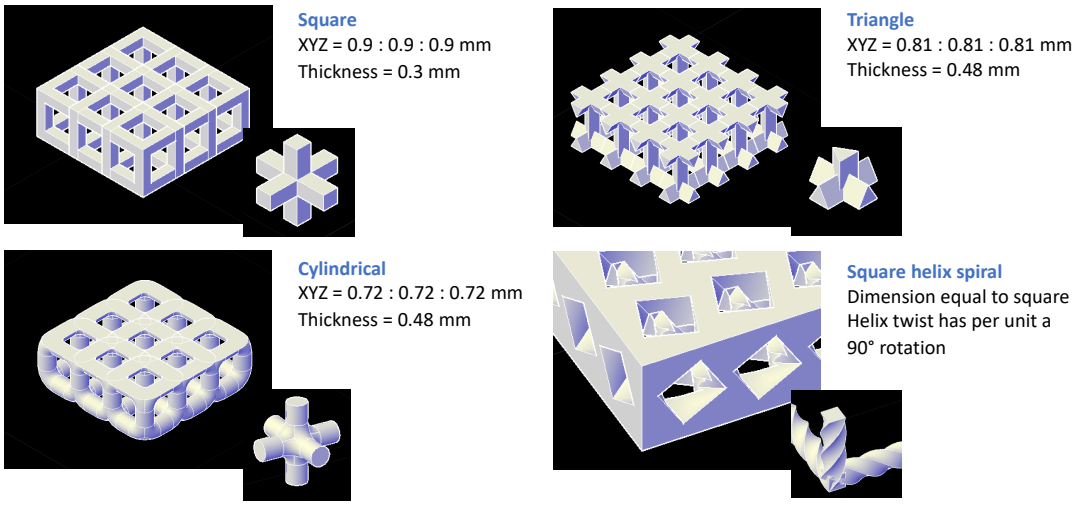

Figure 3.5: CAD models of four electrodes with an equal grid structure but differently shaped rods

electrodes were oxidized for 5 h at 250 °C, carbonized for 1 h at 850 °C and optionally oxidized again for 1 h at 450 °C.

Redox flow cell

The thermally treated electrodes were tested in a single electrolyte flow cell configuration. A schematic of the assembly can be seen in Figure 3.6, the flow cell configurations can be seen in .. ... A FreudenbergH23 carbon cloth (Fuel Cell Store) with an uncompressed thickness of 210 µm and a porosity of 80% was used as received as the reference electrode [58]. All the electrodes were cut to 1.7 cm × 1.5 cm, which results in an external area of 2.55 cm^2. The non-aquous electrolyte solution was prepared with 0.1 M 2,2,6,6-Tetramethylpiperidin-1-yl)oxyl (TEMPO·, Sigma Aldrich 98%) and 0.1 M 2,2,6,6-Tetramethyl-1-piperidinyloxy-oxo (TEMPO+) hexafluorophosphate (synthesised in house) as redox couple and 1.0 M tetrabutylammonium hexafluorophosphate ($TBAPF_6$, Sigma Aldrich >99%) as supporting salt, all dissolved in acetonitrile. Daramic 175 (SLI Flatsheet Membrane, 175 µm) was used as membrane for this system. The aqueous electrolyte solution was prepared with 0.1 M ferrous chloride hydrate ($FeCl_2 \cdot 4\,H_2O$, 98%, Sigma-Aldrich) and 0.1 M ferric chloride hydrate ($FeCl_3 \cdot 6\,H_2O$, 97%, Sigma-Aldrich) as redox couple and 1.0 M sodium chloride (NaCl, ≥99.0%, AkzoNobel) as supporting salt, all dissolved in deonized water. The Nafion 211 membrane (Fuel Cell Store, 25.4 µm) was used for this system.

The flow cells were assembled by stacking the following items on top of each other: a Teflon body, to which nipples are connected which distribute the liquid and in which O-rings are placed which prevent leakages; a current collector with an embedded flow field, to which an electricity connector is screwed; Teflon gaskets, which control the compression with their incompressible thickness; the electrode cut to size of the gasket; a membrane larger in size than the electrode, so that mixing of the electrolytes is prevented; another electrode and gasket; another current collector; and another body with nipples and O-rings. The stack is secured together with assembly pins and bolts and screws, of which the latter are fasted in a stepwise fashion to a compression of 2 N m, so that proper contact between the elements is ensured and leaking is prevented. The stack is connected to the electrolyte tanks with LS-14 tubes. The electrolyte is pumped with a superficial velocity (v_e) of 0.5, 1.5, and 5.0 cm s^{-1} through the cells with a Masterflex L/S Easy-

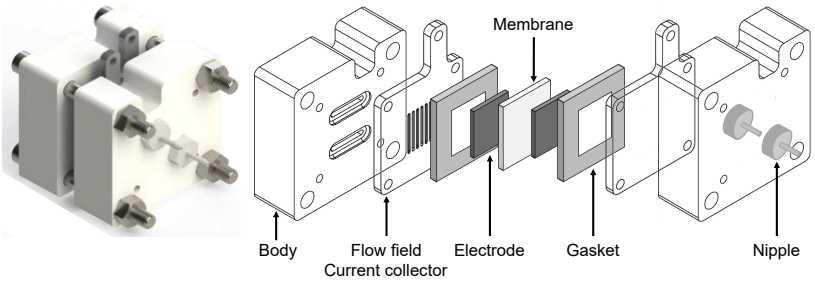

Figure 3.6: Schematic representation of an assembled and disassembled redox flow cell [107]

Load II pump. Different velocities are measured in descending flow rate order so to account for differences in the electrode thickness. The velocity was calculated according to Equation 3.3 , in which Q is the volumetric flow rate ($m^3\ s^{-1}$), t_e is the compressed electrode thickness (m) and w_e is the electrode width (m). The electricity collectors are connected to the Biologic VMP-300 potentiostat.

$$v_e = \frac{Q}{t_e w_e} \tag{3.3}$$

The electrochemical experiments were performed in a discharge mode in a single electrolyte configuration (see Figure 3.7 and Figure 3.8 for the non-aqueous and aqueous flow cells respectively). The same reaction occurs on both side, so there is no net reaction, and the OCV becomes nearly zero. Polarization curves were obtained by applying a constant voltage of 0.05 V for 1 min and measuring the responding current over a voltage range of 0.0–1.0 V. The resistance of the cell was measured with an impedance spectroscopy at OCV with an amplitude of 10 mV and a frequency range of 1–100 kHz with 8 points per decade, 6 measurements per frequency and a waiting time of 0.10 period before each frequency.

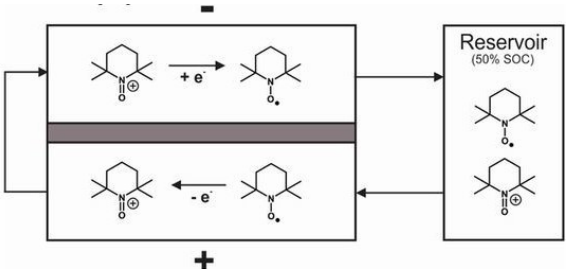

Figure 3.7: Schematic representation of a single non-aqueous electrolyte flow cell configuration containing TEMPO/$TEMPO^+$ [18].

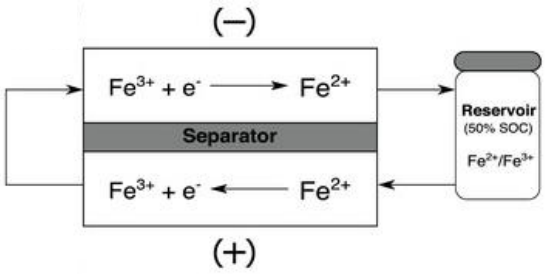

Figure 3.8: Schematic representation of a single aqueous electrolyte flow cell configuration containing Fe^{2+}/Fe^{+3} [20].

Three electrode cell set-up

In order to study the kinetics of the material, an attempt was made to perform a three electrode cell experiment on the carbonized electrodes. Unfortunately this experiment failed, as the crushed electrode could not bind with the binder. This was most likely because the particles in the crushed powder were still to large.

Chapter 4. Results and Discussion

In this chapter the results of the conducted experiments as described in Chapter 3 are presented and discussed with respect to the theory and values found in literature. The order of this chapter follows the synthesis of the electrodes in chronological order, which is the polymerization-induced phase separation, 3D printing, thermal treatments, and electrochemical performance.

4.1. Microporosity via polymerization-induced phase separation

In theory microporosity can be achieved by mixing an inert porogen with a liquid resin and extracting it after the polymerization is complete. In this section the this concept is investigated in practice. A visual qualitative analysis with the SEM is used to see if pores are present on the surface and/or in the bulk of the plastic. The latter is done usinga cross section of the sample. The extent of the extraction is quantified with a TGA. The weight loss of untreated pure PETA and untreated PETA with porogen together form the porogen extraction phase, which is indicated in red (see Figure 4.2 for an example). If the weight loss of the samples in which the porogen is extracted with a treatment lies near or higher than this phase then the extraction was successful, as all the porogen is removed. If it lies in the red phase, then solvent or porogen were still present after the extraction treatment. Attention should be given to the composition of the samples as well. The porogens are *added* as weight percentage of PETA. The composition of the mixture lies is thus different: 10 wt% porogen forms 9.1 wt% of the total mixture, 20 wt% forms 16.7 wt% and 30 wt% forms 23 wt%.

Polymerization of the resin

Three polymers made with different acrylate monomers were tested with a TGA on whether they are suitable as resin. The total weight left at 850 °Cfor HEMA, EDMA, and PETA are 1.8 wt%, 1.8 wt% and 8.8 wt% respectively. PETA is the only monomer with a substantial mass left after the carbonization. This indicates that it polymerizes to a thermoset – as is required for this resin. It performs even better than the High Temp resin, which holds 4.7 % of its weight. The TGA can be seen in Figure C.1 in Appendix C. These results are attributed to the high functionality of PETA (eight covalent bonds per monomer) compared to HEMA and EDMA (two and four, respectively). Monomers with a functionality of three and higher can form a thermoset due to the ability to crosslink, and the thermoset quality improves with a higher crosslinking density. The strong covalent bonds formed between polymer chains during crosslinking hold upon application of heat, while the regular non-covalent between the chains do not, and break down easily [78, 90, 108]. Based on these results, PETA is chosen as monomer used for the resin.

During the polymerization of the porogen and resin mixture, a phase separation takes place. Upon decrease of monomer concentration, the porogen is extracted out of the monomer phase in which it can dissolve, into the polymer phase in which it is insoluble. Hence, a polymer-rich and a porogen-rich phase arise [47, 109–111]. These phases can clearly be seen in the two

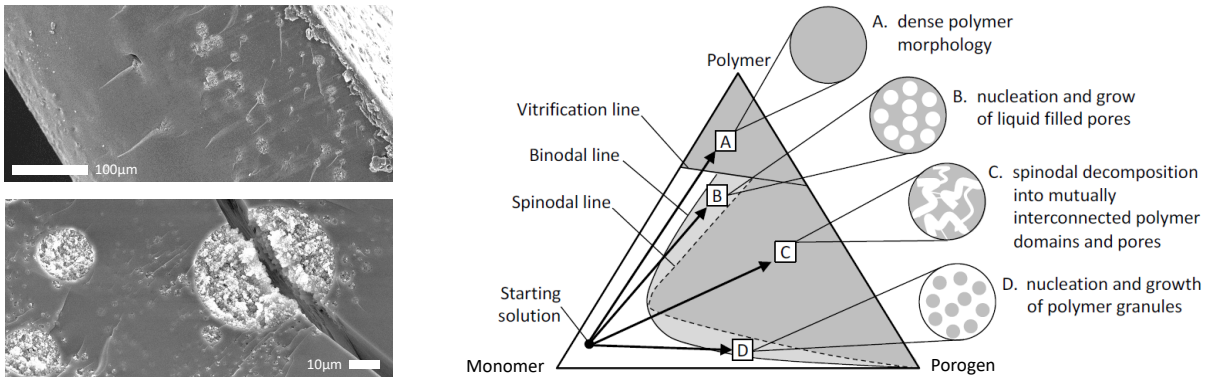

Figure 4.1: Image taken with a SEM at a 500x (top left) and 5000x (bottom left) magnification of a cross section of polymerized PETA + 30 wt% 1-decanol washed for 24 h with acetone, and an illustrative example of various phase separating pathways in a ternary diagram (right), adapted from Nijmeijer [109].

left images of Figure 4.1. They display the cross section of a polymerized matrix of PETA and 30 wt% 1-decanol, which was washed out with acetone. The visible pores are formed by the agglomeration of porogen in droplets during the phase separation, which open up after the extraction. The pores show a clear dispersion in both the distribution (top left image) and size (bottom left image). The agglomerates are formed in a response of an increase of the Gibbs free energy due to the change in monomer and polymer concentration. By merging into droplets, the porogen reduces the area with the polymer and thus reduces the unfavorable interface tension [109–111]. This process is illustrated in the ternary diagram on the right of Figure 4.1. The binodal and spinodal line form the transition of the monomer-polymer-porogen mixture from stable to metastable and from metastable to unstable respectively. The lines indicate how the volume fraction of the components changes, which is also known as the pathway. This pathway determines the outcome of the polymer matrix and is influenced by the initial composition and the speed of the phase separation - in this case thus by the UV light intensity in the resin [47, 109–111].For this case, pathway C is required, as it will open up the polymer and gives the electrolyte easy access to many pores - and thus to a large surface [26, 47]. In the sample of Figure 4.1 a binodal decomposition took place, in which demixing between the liquid monomer-porogen phase occurs, before the spinodal demixing with the liquid and solid phase separation occurred. Hence, the porogen already was able to form and grow nucleus, which became larger well dispersed droplets in the polymer matrix [109, 110].

Porogen selection

Two porogens mixtures, 30 wt% cyclohexanol and 30 wt% 1-decanol, were polymerized with PETA. The results can be seen in the top and bottom solid boxes of Figure 4.2 respectively. The SEM photos show that cyclohexanol failed to form distinctive pores upon the phase separation, whereas 1-decanol did form pores. This applies for both the cross section and the surface. Various tested extraction and evaporation methods gave similar results, those can be seen in Figures C.2 to C.4 in Appendix C. The dashed contoured box on the right shows the results of

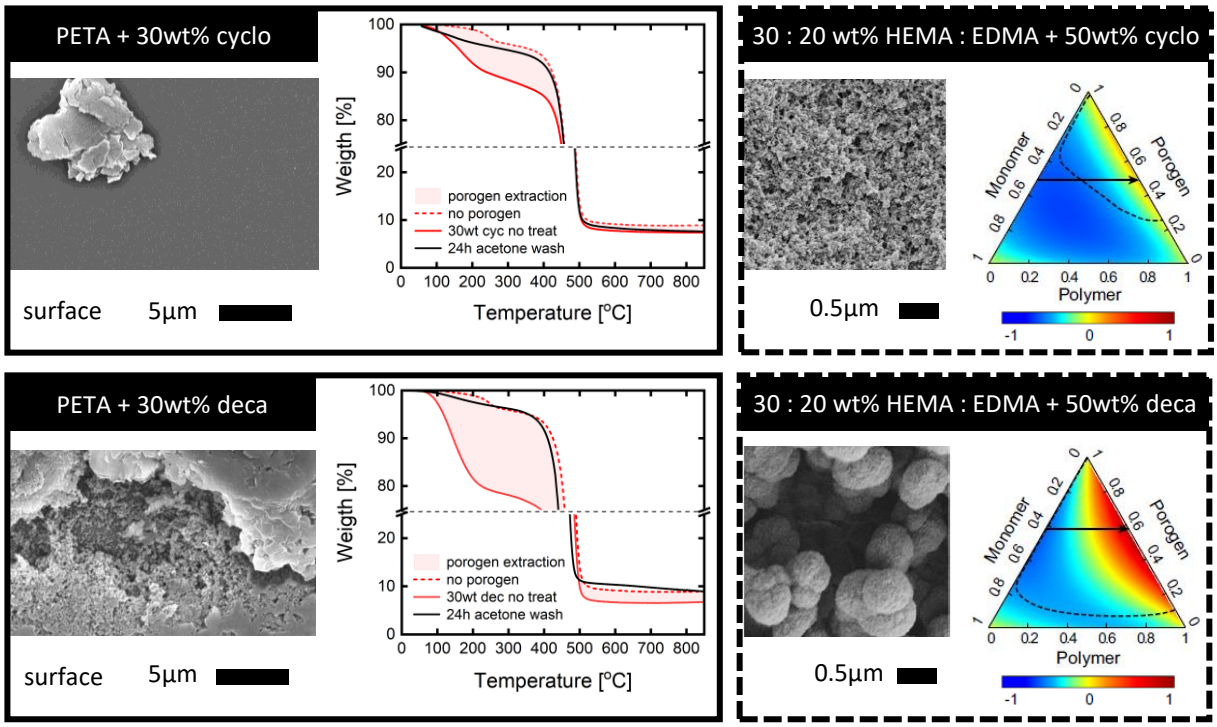

Figure 4.2: Surface image taken with a SEM at 5000× magnification and a TGA of polymerized PETA + 30 wt% cyclohexanol (top left) and PETA + 30 wt% 1-decanol (bottom left) washed with acetone for 24 h. The surface image and ternary diagram (ΔG_{mix} normalized) of the phase extraction of 30 wt% PETA + 20 wt% EDMA with 50 wt% cyclohexanol or 50 wt% 1-decanol of Dong et al. [47] can be seen on the top and bottom right respectively.

Dong et al. [47], who polymerized a resin with the same porogens but with HEMA and EDMA as monomers. Based on the ternary diagram it is clear that 1-decanol has less affinity with the acrylate monomers than cyclohexanol, which results in a quicker and faster phase separation. The unstable phase indicated with the spinodal is reached almost immediately for 1-decanol, but is not for cyclohexanol. Furthermore, the change of the free energy of mixture (with ΔG_{mix} normalized) is much more severe. Thus, the driving force to separation is greater compared to cyclohexanol [110, 111]. This is reflected by the significantly larger pores formed by 1-decanol in their polymer matrix [47]. These findings could explain why 1-decanol does form visible pores in a PETA based polymer matrix, and why cyclohexanol does not. Because even though Dong et al. [47] do not use the exact same resin, their results do give a clear indication on how the porogens interact with acrylate based monomers.

A closer inspection of the TGA results reveal that less cyclohexanol is present in the polymerized mixture then when it was mixed in the monomer resin. The weight difference between untreated pure PETA and untreated polymerized PETA + 30 wt% cyclohexanol is 7.5 wt% at 300 °C, whilst it should have been 23 wt% (the concentration of the porogen in the resin before polymerization). 1-decanol performs better with weight difference of 17.6 wt%. The difference in weight for both porogens is most likely due to the fact that some of the porogen is completely pushed out of the polymer matrix during the polymerization-induced phase separation, instead of being pushed into agglomerates inside the matrix (which form the pores) [109, 110]. The samples were a bit wet

after the polymerization, which is most likely the porogen, so this hypothesis is very reasonable. Because the phase separation occurs slower and more graduate for cyclohexanol compared to 1-decanol, it reasonable to argue that it can diffuse out of the polymer-monomer matrix more easily, giving rise to smaller agglomerates, and thus less porogen present inside the matrix as well [47, 109–111]. Another hypothesis is that the porogen is pushed out of the polymer matrix during the shrinkage induced by the polymerization. Cyclohexanol could therefore experience a higher pressure to be pushed out than 1-decanol due to the smaller pore size. Evaporation of the porogen after the polymerization and phase separation is completed could have resulted in a weight loss as well, which is not detected by the TGA. Based on these results it was decided to continue with 1-decanol as porogen.

Porogen concentration

The SEM images of the extraction of 10 wt% (top), 20 wt% (middle) and 30 wt% (bottom) 1-decanol from polymerized PETA with an acetone wash of 24 h shows that more pores are formed

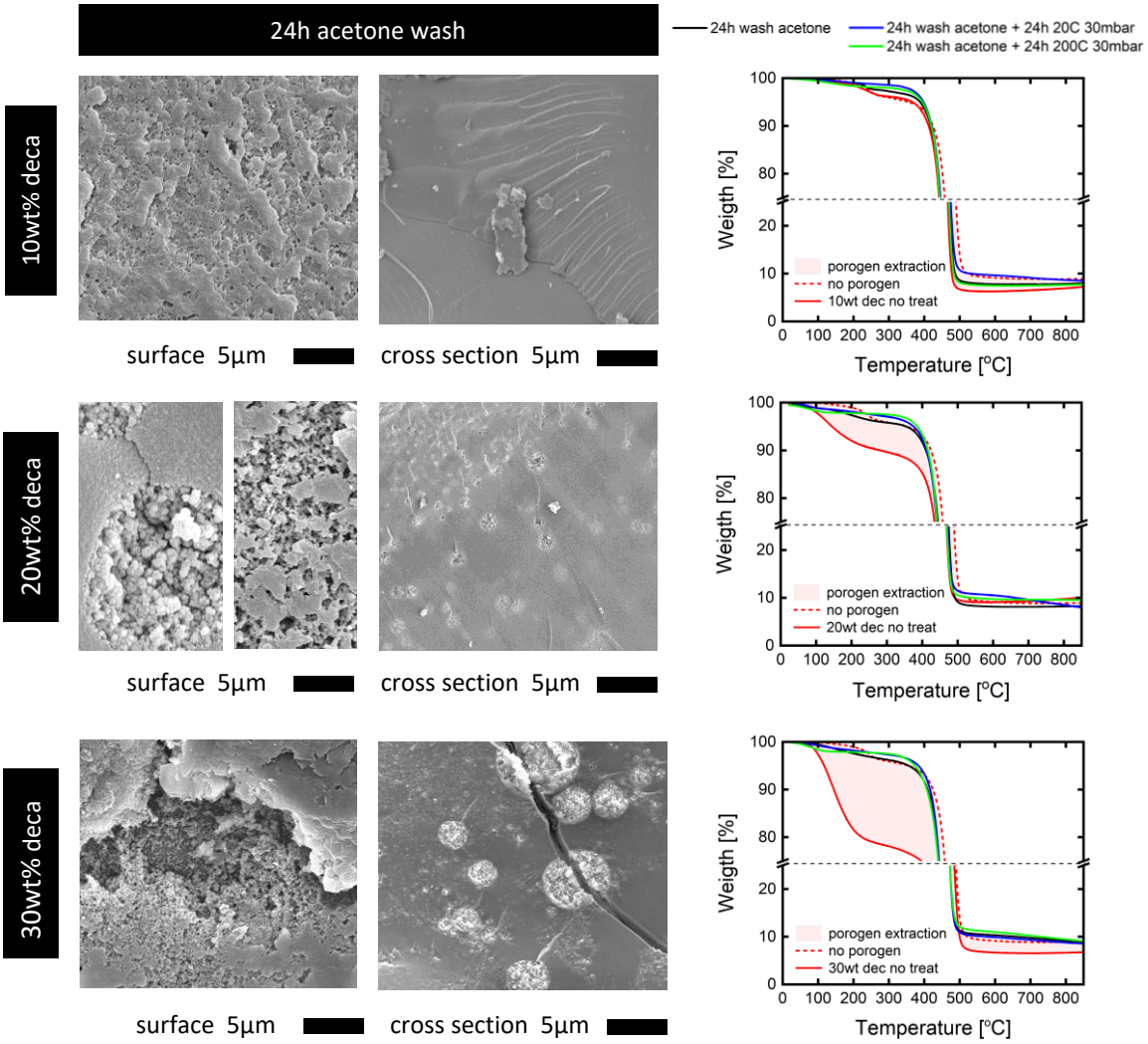

Figure 4.3: Image taken with a SEM at 5000× magnification of surface (left) and cross section (middle) and TGA (right) of polymerized PETA + 10 wt%- (top), + 20 wt%- (middle) and + 30 wt% 1-decanol (bottom)

at a higher porogen concentration - as is to be expected (Figure 4.3). The brittleness also increases for increasing porogen concentration, to a point that the plastic samples of PETA + 30 wt% 1-decanol broke upon touch. Once again, the weight loss of the untreated polymerized samples with porogen does not match the weight of the porogen mixed into the monomer resin. At 350 °C, the weight difference between untreated pure PETA and untreated polymerized PETA + porogen is: 0 wt% for PETA + 10 wt% 1-decanol, 7 wt% for PETA + 20 wt% 1-decanol, and 18 wt% for PETA + 30 wt% 1-decanol. This can again most presumably be attributed to the arguments given for cyclohexanol: 1-decanol separates during the phase separation to agglomerates inside the polymer matrix and to a layer on top of the matrix; 1-decanol is pushed out of the agglomerates during the shrinkage of PETA polymerizing; 1-decanol already evaporated to an extent before it was tested in the TGA [109, 110]. Regarding the phase separation, the spinodal in the ternary diagram of 1-decanol (Figure 4.1) reveals that the interaction between 1-decanol and an acrylate is less favorable for 30 wt% then for 10 wt%. If the Gibbs free energy is higher, then the driving force for separation is higher as well. This results in less time to establish an equilibrium and reduce the interface tensions for the porogen agglomerates. Hence, they will gather in droplets inside the polymer matrix before they had a chance to gather into a layer on the outside of the matrix [47, 109, 110]. It can be concluded that the porogen extraction with washing in acetone for 24 h, washing followed by an evaporation at 20 °C and 30 mbar for 24 h, and washing followed by an evaporation at 200 °C and 30 mbar for 24 h went successfully: they all lie in the TGA near or above the porogen extraction phase, indicated in red (Figure 4.3). The SEM images of these extraction methods can be seen in Figures C.5 to C.8 in Appendix C. The extraction is discussed more elaborate in the next three sections. Overall, due to sufficient pores and a minimized brittleness it was decided to continue with the resin PETA+20 wt% 1-decanol.

Porogen extraction

Polymerized PETA + 20 wt% 1-decanol was first washed for 24 h in acetone in order to extract the porogen. Acetone was then removed with three different evaporation methods, of which the results can be seen in Figure 4.4. The evaporation at 20 °C and 200 °C at 30 mbar extracted the solvent and traces of porogen out of the polymer matrix successfully, visible by the pores on

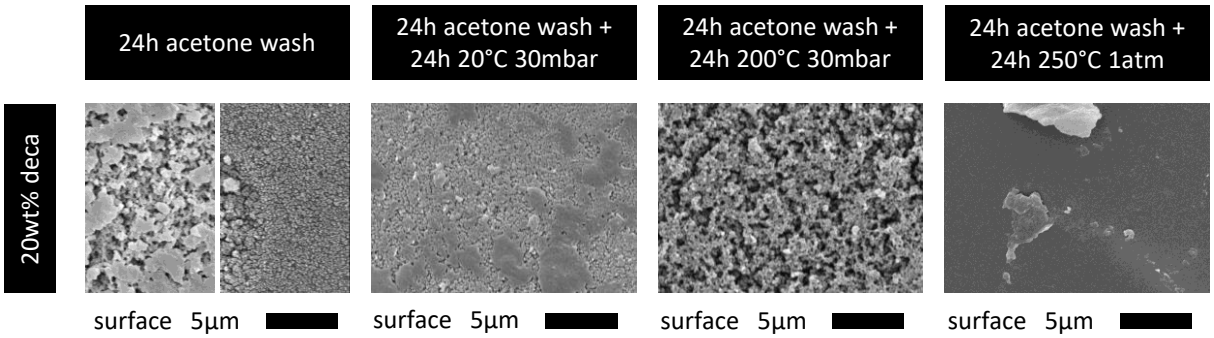

Figure 4.4: Surface image taken with a SEM at 5000× magnification of PETA + 20 wt% 1-decanol washed with acetone for 24 h (left), and three different evaporation treatments (right).

the surface. A higher temperature gives rise to more pores on the surface when compared to the mere washed sample. This is as expected, since more added energy results in a faster and more extensive evaporation of the solvent and porogen [112, 113]. The porosity of the samples is however loss during the evaporation treatment at 250 °C at 1 atm. The surface and cross section (see Figures C.5 to C.8 in Appendix C) are completely smooth, whilst porosity was formed after the wash treatment. The loss in porosity is attributed to the oxygen present in air in atmospheric conditions: the combination of oxygen and heat causes thermal oxidation, which alters and breaks down the polymer [73, 75, 76, 114]. This effect is discussed more indepth in Section 4.3. Overall, the evaporation of solvent from the polymer at 200 °C and 30 mbar was chosen as most favorable extraction method after a 24 h wash in acetone.

Solvent selection

The extraction of the porogen by washing it for 24 h or 48 h with a solvent and evaporating the solvent for 24 h at 200 °C and 20 mbar was tested with four different solvents: acetone (Figure 4.3), IPA, ethanol and xylene (Figure 4.5 left, middle, and right respectively). The TGA reveals that every solvent was removed during the evaporation step (Figure 4.3 for acetone and Figure 4.5 for the rest). However, the extraction with IPA, ethanol and xylene is not successful based on their SEM images, as no pores are visible on the surface. Ethanol and xylene did manage to extract the solvent and porogen out of the bulk of the sample, based on their cross section images (Figures C.11 to C.14 in Appendix C). IPA on the other did not show pores on either the surface or cross section. This is against expectations and contradictory with the results

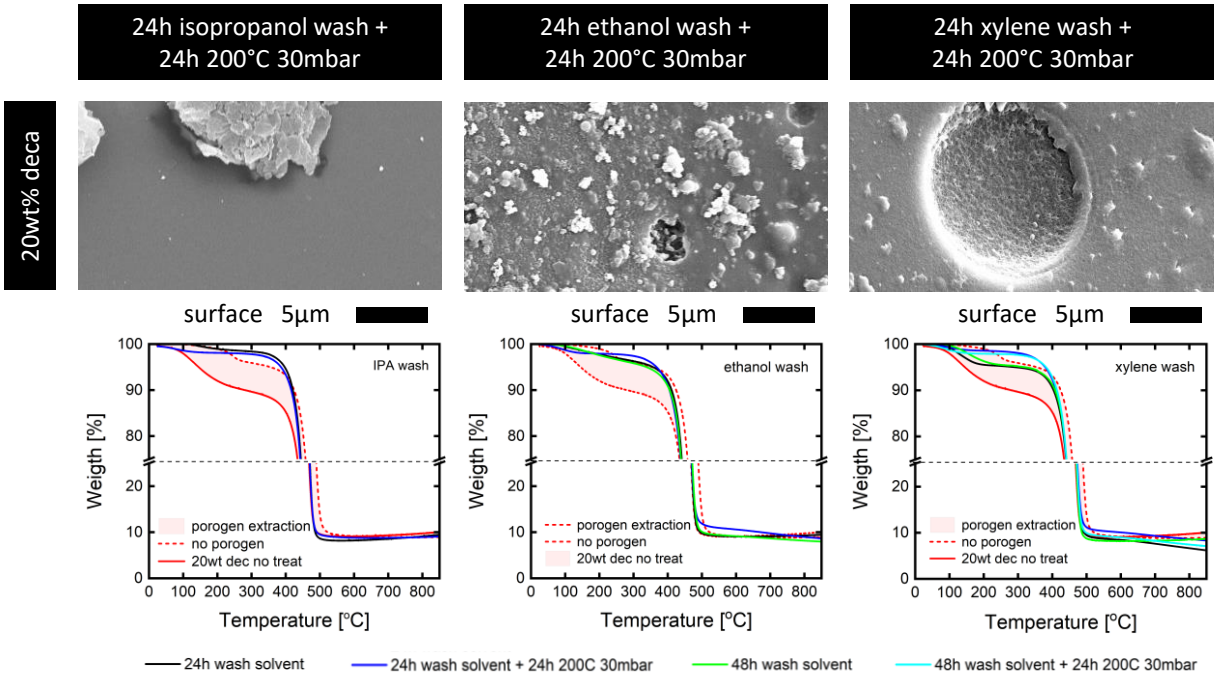

Figure 4.5: Surface image taken with a SEM at 5000× magnification and TGA of PETA + 20 wt% 1-decanol washed for 24 h with IPA (left), ethanol (middle), and xylene (right).

of the TGA, so this should be confirmed with a duplo or triplo experiment. Furthermore, the samples which were washed with acetone and xylene twice showed against expectations less pores on the surface, whilst the success of the extraction based on the TGA remains the same. The samples washed with ethanol twice did show more pores on the surface.

The success of the extraction with acetone can be attributed to its ketone group: it forms a hydrogen bond with the alcohol group of 1-decanol, and is slightly repelled by the δ^- ester group of the polymerized PETA [78, 115]. Hence, the interactions are most favorable between the solvent and porogen, not with the polymer matrix. IPA and ethanol on the other side can form hydrogen bonds with the ester groups of PETA, and are therefore in competition with 1-decanol [78, 115]. Xylene can bind the alcohol group of 1-decanol by means of hydrogen-bonding to its aromatic ring, giving rise to extraction. However, π-hydrogen bonds are several kcal mol^{-1} weaker than regular hydrogen-bonds [115]. Furthermore, all the four solvents have a favorable vapor pressure below atmospheric pressure, indicating that they evaporate easily. Their surface tension with air are similar as well, and their boiling points (56–139 °C) were all below the evaporation temperature of 200 °C [116]. Thus, no explanation on the success rate of extraction of the different solvents could be found in these physical properties.

Based on this information, it can be hypothesized that all four solvents do extract the porogen successfully (see the TGA's), but only acetone could be evaporated completely out of the matrix due to repulsive hydrogen-bonds with PETA, whilst IPA, ethanol and xylene could not completely be evaporated due to attractive hydrogen-bonds, forming a small layer on top (see the SEM images). This small layer is clearly visible in the SEM images of the surface and cross section of an extraction with a 24 h wash with ethanol and a 24 h evaporation at 200 °C at 30 mbar (Figure 4.6): the partially rough surface of the merely washed sample becomes completely smooth after the evaporation of ethanol out of the polymer matrix. The evaporation of the solvent from the bulk of the polymer to the atmosphere requires that the droplets diffuse from the bulk to the surface and evaporate from the surface into the air [117]. The resistance of solvent evaporation remains fairly constant during the process of drying, but the resistance of the solvent transport increases for a decreasing solvent concentration. The resistance of the last few droplets from the bulk to the surface is in the end so high that the diffusion rate becomes

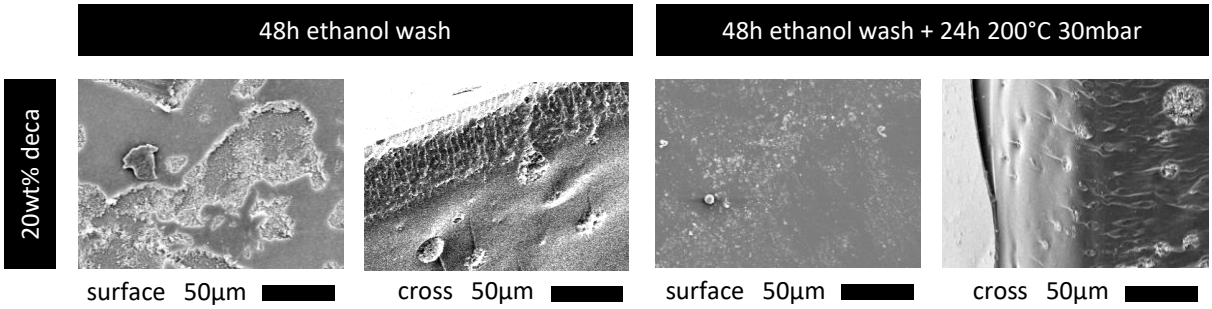

Figure 4.6: Image taken with a SEM at 500× magnification of the surface and cross section of polymerized PETA + 20 wt% 1-decanol washed with ethanol for 48 h (left), and washed and evaporated at 200 °C at 30 mbar (right).

exceptionally slow - so slow that the droplets remain near the top layer of the polymer matrix [117, 118]. The rough structure and large surface of the pores do influence the wetting with the solvent as well, but it is not possible to provide a hypothesis on this effect due to limited information on the surface and interaction parameters.

Another hypothesis on the formation of the layer on the surface is that the either the heat or solvent change the chemical composition of the polymer matrix. However, this hypothesis is less likely: if either the heat or solvent would have altered the matrix, then the loss of pores should have been visible in both the cross section and surface, as was the case for the evaporation at 250 °C under air (Figure 4.4, right). It is furthermore not likely that the solvent and heat alter the polymer on the surface only, without changing the polymer in the bulk. It is namely certain that the heat and solvent can reach both the bulk and surface - otherwise no extraction would have taken place in the first place. However, no information could be found on possible reactions with the polymer and the solvents at elevated temperatures, so this hypothesis cannot be ruled out. Based on the results it is clear that the extraction of 20 wt% 1-decanol out of polymerized PETA can be done successfully with a washing treatment with acetone for 24 h, followed by an evaporation treatment at 200 °C at 20 mbar.

4.2. Macroporosity via 3D printing

First the accuracy, precision and resolution with which the Form 3 can print holes and pins is investigated based on the analysis of 83 SEM photos.

Printed holes of Form 3

The left photo of Figure 4.7 shows printed round and square holes which had in the CAD model a set diameter of 450 µm and a spacing of 100 µm. The Form 3 has difficulties with printing holes, as it printed some holes partly (B) or not at all (C), and failed to print the shapes uniformly. The successfully printed holes (A), defined as successful if the diameter is at least 50% of the set diameter, form the minority of the attempted printed holes. On top of that, the successfully printed holes are smaller in size than the set diameter in the CAD software, which is indicated with the red circle. This is due to fact that resin of the plastic regions adjacent to the holes polymerized outside its given boundaries, which decreases the size of the hole. For the sample in this image, the diameter of the holes are on average 313 µm and 201 µm for the round and square holes respectively, both significantly smaller than the set 450 µm. The success rates are 87% and 10% for respectively the round and square holes in this sample, and both shapes resemble more than not a circle.

The deviations in the measured size is systematic for all the holes printed, regardless the diameter, shape and spacing, as they all have a smaller measured diameter than set (Figure 4.8, left). The larger holes shows a smaller deviation ((~100 µm) than the smaller holes (~150 µm). Furthermore, smaller holes and holes printed at a smaller distance from each other are printed

more poorly or even not at all (Figure 4.8, middle). Noteworthy is that the absolute deviation of the sum of the hole and the solidified space between the holes very small: the smaller size of the hole is compensated with a larger solidified section in between, resulting in an overall correct dimension. For example: holes placed 100 µm apart were printed with a diameter that was 162 µm smaller than set, whereas the space in between was printed 177 µm too large. This trend can be seen in Figure B.1. The Form 3 can print holes with a diameter of 500 µm or larger successfully - holes with a smaller diameter would be printed to small or get clogged (Figure 4.8, middle). The holes that are spaced with 100 µm are printed less successful than those that are 500 µm apart.

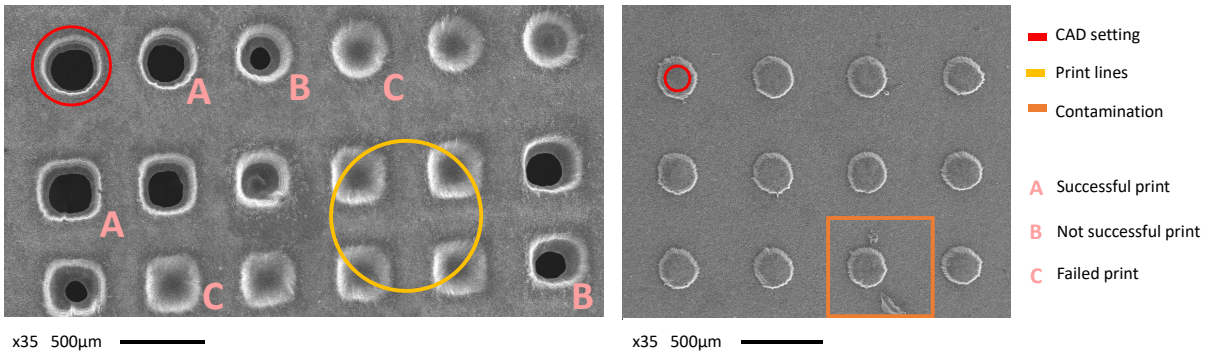

Figure 4.7: SEM image of printed round and square holes of with the diameter set to 450 µm (left) and round pins with the diameter set to 80 µm (right) on a plate of 0.5 mm thick. Additional indications are added in color

Printed pins of Form 3

Form 3 does print pins successfully. The photo on the right of Figure 4.7 shows printed pins which have on average a diameter of 232 µm, whilst they were set to have a diameter of 80 µm at a spacing of 500 µm. This shows again that resin is polymerized outside the set boundaries from the CAD model. Both the round and the square printed pins have a circular shape, although not perfectly round. They are therefore combined into one dataset for the quantitative analysis. The deviations in the measured size is systematic for all the printed pins (Figure 4.8, right), as all the pins have a larger diameter compared to their set diameter. The overshoot however decreases with an increase in the set diameter. The resolution of Form 3 to print pins is 250 µm.

Print precision and accuracy of Form 3

The precision of the Form 3 is good, as opposed to the accuracy, given the small error bars of the measured diameters of the printed holes and pins (Figure 4.8, left and right). These deviations observed are reported in literature as well: holes with diameter smaller than 500 µm are not printed at all or not printed successfully [119], a print deviation for pins of ~140 µm was measured for the Form2 [120], and print deviations were relatively the largest for the smallest prints [119, 120]. Furthermore, the printed holes resembles the same pattern as the print pathway generated from the print model (Figure 4.9). This, in combination with the small deviation the

size of the holes plus solidified area in between, indicates that the precision of the Form 3 is good, but the execution and thus the accuracy is not.

Lastly, there a few other noteworthy observations from the SEM photos taken. In the photo on the left of Figure 4.7 the line of the laser, which has a spot size of 85 µm, can clearly be distinguished in between the holes (indicated with the yellow circle). In the orange frame in the photo on the right some contaminations are visible, which appear to be solidified resin as well. At a high magnification of the surface of an horizontally printed sample small spots of on average 2 µm large are visible (Figure 4.9).

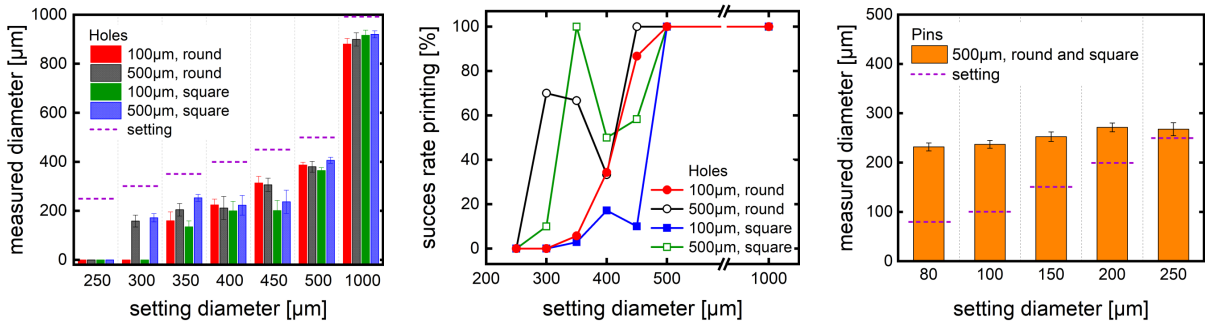

Figure 4.8: Measured performance of the Form 3 on printing accuracy on pins (left) and on holes (right), and the success rate of printing holes (right). The shape and spacing of the holes is indicated in the legend.

The deviations of the printed diameter of the holes and pins from the model can be caused by numerous flaws in the printing process. Although not many studies are performed on the *exact* influence of specific elements of the printing process on the accuracy and precision, there is a general consensus on causative factors arising from the software, hardware and resin [92, 121, 122]. The likeliness of these factors on the deviations observed will be, based on indicative studies, discussed next.

Flaws in the design

A 3D product is designed and translated to a readable file for the printer making use of software. The design has an influence on how successful the product will be printed: the SLA print technique is not very well suited to print overhanging parts, cups, or small and unsupported details [121, 123]. Formlabs recommends to print holes with a diameter ≥500 µm, and pillars ≥200 µm, with a maximum overhang of 29 mm [124]. The outcome of the results is in line with these recommendations.

The orientation of the product with respect to the print platform chosen by the user also affects the accuracy. Literature reports that the highest accuracy will be achieved if among other things the number of horizontal faces in the XY direction and the number of holes with their axes in the Z direction are maximized [92, 119, 123]. Holes and pillars printed under an angle show larger deviations in the size and shape, in which the largest deviations was measured for an angle of 90° [92, 119, 123]. Thus, the orientation of the print with respect to gravity is important, most likely

due to unconverted resin on the sample that is pulled in a downwards direction, after which it is polymerized during the curing of a new layer. The prints used for this experiments fulfill these conditions, so an incorrect orientation will not be the cause of the inaccuracies. Formlabs on the other hand recommends for flat surfaces a horizontal tilt of 10–20° for the best success rate, as it decrease the surface area of each layer and reduces the contact area with the tank [125].

Flaws in the software and settings

During the translation of the CAD model into the print file, various errors which diminish details and thus accuracy of the final print can occur. These errors are among other things incorrect slicing, tessellation and inaccurate rendered printing pathways [121, 123]. Especially uniform rendering and slicing methods, as opposed to adaptive methods, are prone to flaws: the method can be too rough for translating small elements, which causes loss of detail in the print file and eventually the printed product [121, 123]. The print pathways shown in Figure 4.10 does however circumference the correct shape and resemble the CAD model. The prints in Figure 4.7 also show that the pattern of the pathway is printed correctly. The execution of printing the pattern is however sloppy. Thus, the software can be ruled out as causation for the observed deviations.

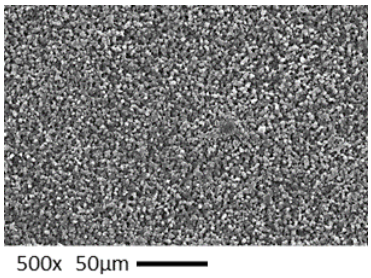

Figure 4.9: SEM image of a printed sample

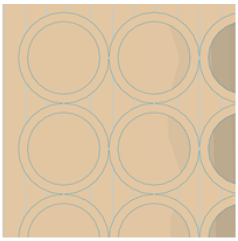

Figure 4.10: Laser pathway of print file

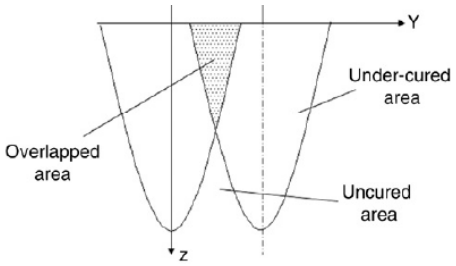

Figure 4.11: Curing width and depth of two consecutive laser hits overlapping [126]

Print settings including the layer thickness, hatch spacing and overcure, exposure time, lifting height and speed, and print delay are important for the printer's accuracy. These settings influence the control on the photopolymerization, as they determine the amount of energy of one UV hit, the depth of polymerization of one hit, and the precision of the pathway of the laser [27, 92, 121, 122, 126]. Of these settings only the layer thickness can be adjusted by the user for the Form 3, which was set to the highest accuracy (25 µm) [103]. Formlabs provides no information on the other settings. The pathway in Figure 4.10 shows that the laser circumvents each hole, resulting in that the section between the holes is cured twice. With a laser width of 85 µm one would thus expect that the section between the holes (which is set to 100 µm) will have a width of 170 µm if the laser is not allowed to cure on section twice (so 2×85), less if the adjacent laser pathways do overlap [93]. However, the measured width is on average 278 µm, much larger than expected. Thus, the print pathway does not explain the observed deviations in accuracy. The print pathway does however confirm that the precision of the printer is high, as was mentioned already earlier.

Flaws in the polymerization process

During the photopolymerization light penetrates the resin and activates the initiator, generating radicals. The spot size of the laser beam does however not exactly translate to the shape and size of the polymerized sample. The curing accuracy, which is related to the curing depth and curing width, is influenced by the laser (spot size and penetration depth), the resin (UV refraction and absorption, rate of polymerization, viscosity and scattering of added components) and the interaction between the two [92, 126–128]. The polymerization process in the resin is, although seemingly simple, complicated to decipher: polymerization kinetics, homogeneity of initiator and monomer concentration, layer adhesion, and environmental conditions vary in and between the layers [92, 129]. During the propagation, the resin (a mixture containing monomer and polymer) becomes more viscous due to an increase of crosslinking, resulting in a rubbery and eventually glassy state. In these states, the polymerization rate goes down, and the reaction rate becomes diffusion controlled instead of kinetically controlled [78, 128, 129]. Furthermore, the oxygen present in the mixture acts as an inhibitor by quenching the radicals, slowing down the overall reaction rate and allows a fresh layer of resin always to be present below the printed part. This leads to smaller polymerized particles and a lower monomer conversion [128–130].

The single dots of ~2 µm visible on the surface of a 3D-printed sample (Figure 4.9) could resemble polymerized regions initiated by single UV hits. Several papers mention an ultimate resolution of SLA of 1 µm, although it is not specified what this resolution is based on [131, 132]. Based on the research of ASML, one can conclude that this resolution is defined by the ultimate resolution of an UV laser beam [133]. This resolution is however equal to the size of the single polymerized dots. Hence, it is likely that the initiation and propagation of one single UV hit is contained to 2 µm, but this cannot be stated with full certainty. If this is the case, then rapid propagation can be excluded as the cause of the large deviations reported in the results.

It is hypothesized that the effect of crosslinking and additional curing between polymer chains generated by different UV light spots could possibly increase the width of the cured region. Furthermore, there is a possibility that small polymer chains (oligomers) are already present in the resin [128]. If those chains crosslink with each other, very large chains can arise. Although this is a likely explanation for small deviations observed in the accuracy, no statement can be made on whether this can cause deviations on the scale of 100 µm. Randomly distributed uncontrolled polymerization due to, for example, unevenly distributed initiators, inhibitors, or oligomers could be another reason on why the deviations in print accuracy arise [92]. Due to lack of knowledge on the composition of the resin this effect can neither be studied, confirmed, or ruled out.

Over- and undercured regions due to overlapping print pathways give rise to a distribution in crosslinking density (Figure 4.11) [122, 126]. The crosslinked networks formed during printing cause internal stresses, which can lead to shrinkage or deformation of the product, and conse-

quently a decrease in printing accuracy. Differences in crosslinking density would then result in a different shrinkage amounts [92, 121, 122, 126, 129, 134]. The volume shrinkage for acrylate resins is reportedly a few percent – not enough to adequately explain the results [121, 126, 134]

Flaws in the hardware

Optical phenomena such as diffraction, reflection, and scattering of the UV light can cause significant deviations in the printing accuracy. These phenomena occur with every interaction of light and an object: lenses, mirrors, air, the tray, and the resin. If light is diffracted or scattered around the spot of the laser, then resin is cured outside that boundary as well, which can decrease the accuracy and resolution [121, 127, 128]. The higher the quality of these objects used, the smaller the influence of the optical phenomena [135]. It is due to lack of information on the hardware used in the Form 3 not possible to give a detailed discussion about the interaction with hardware and light.

Nakamoto et al. [127] studied the interaction between the laser and the resin. They found that focal length divided by aperture (f/R) has a significant influence on the maximum width of the solidified polymer: a laser with a spot size of 3.3 µm cures a polymer with a size of 3.2 µm, but a laser with a spot size of 9.3 µm polymerizes a surface with a width of 20 µm, and this trend continues exponentially. The laser beam of the Form 3 with a spot size of 85 µm would, based on an extrapolation of this data, easily solidify a polymer with a maximum lateral width of a few hundred micrometers [127]. Increasing f/R thus does not only increase the laser spot size and depth of focus, it also reduces the sharpness of the focus. In this work This explanation matches the observed deviations in this work: the solidified sections between the holes have a thickness of ~277 µm instead of the set 100 µm, and the pins, with a set diameter of 80–250 µm, all have a diameter of ~252 µm. In the same study, the wavelength and absorption coefficient of the polymer did not have a notable effect on width of the solidified area [127].

4.3. Thermal treatments

The effect of UV curing, dwell time, and temperature of the thermal treatments on a 3D-printed polyacrylate are investigated in terms of change in chemical composition, surface composition and physical properties. Furthermore, the dimensions of the holes and rods in the electrode suitable for carbonization are determined. UV curing did not have a significant effect on any of the investigated properties (see Figure 4.15), so these results are not explicitly considered in this section. The results of the UV cured sample can be seen in Appendix D.

Changes in chemical composition

The polyacrylate obtained from the High Temp V2 resin consists of various trade secret acrylate, methacrylate and urethane dimethacrylate monomers. Table 4.1 shows how the bulk chemical composition of the polyacrylate, measured with EDS, changes for various thermal treatments.

The shift in surface chemistry can be seen in XPS C1s peak in Figure 4.12, in which the regions resemble general peak locations of carbon bonds [136]. It should be noted that the XPS data can only be regarded qualitatively. The fit in Figure 4.13 functions as an illustration on how the peaks are *most likely* fitted, as the fit is based on a fit of a carbon electrode and not on the analyzed carbonized plastic, since no information was available on the exact structure.

treatment			composition [atom %]		
1st oxidation	carbonization	2nd oxidation	carbon	oxygen	nitrogen
-	-	-	85.35	12.12	2.53
5h 250 °C	-	-	71.05	26.53	2.42
1h 250 °C	1h 650 °C	-	86.41	11.54	2.05
5h 250 °C	1h 850 °C	-	94.48	3.77	1.75
5h 250 °C	5h 850 °C	-	94.56	3.94	1.49
5h 250 °C	1h 850 °C	0.5h 450 °C	89.23	9.00	1.77
5h 250 °C	1h 850 °C	1h 450 °C	84.91	13.02	2.07
5h 250 °C	1h 850 °C	5h 450 °C	84.62	12.22	3.16
5h 250 °C	1h 850 °C	12h 450 °C	68.17	29.35	2.49

Table 4.1: Elemental composition obtained from EDS of samples treated with various thermal treatments.

Oxygen and nitrogen are present in the polymer due to the functional groups attached to the carbon backbone. The oxygen content increases after the first and second thermal oxidation. This is accompanied with a decrease in carbon content. A longer oxidation dwell time (5 vs 1 h) results in a higher oxygen content. The nitrogen content decreases for a longer dwell time in the second oxidation, which could be caused by a greater mass loss of carbon fragments. These results are in line with the expectations set in Section 2.2 and what is reported in literature [26, 73, 75]. During the oxidation at moderate temperatures oxidative chain scission, crosslinking, and the formation of oxygen-containing functional groups occur. The oxygen can bind to the carbon chain, and thereby introduce radicals to the chain. Radical fragments then break the chain or bind the chain to other chains [75, 76, 114]. Highly crosslinked polymers can withstand thermal oxidative degradation better than less crosslinked polymer [114]. Transesterification reactions and H-donor/H-acceptor interactions increase the degree of crosslinking as well [76]. Furthermore, functional groups such as carboxyl, hydroxyl, γ-lactone, aldehyde, and ketone are formed on the polymer during the oxidation [73, 76, 137]. This is reflected in the increase of oxygen containing carbon groups in the XPS spectra (Figure 4.12). Oxidative dehydrogenation converts alkanes into alkenes, and this occurs more readily for longer and higher branched alkanes. However, this process only becomes relevant at temperatures above 400 °C [138]. The majority of these reactions produces gases such as CO_2, H_2O, CH_3OH and CH_3COOH are formed [76, 79, 114, 137, 138].

The carbonization process increases the carbon content and decreases the oxygen and nitrogen content with respect to the merely oxidized sample. A higher temperature results in a lower nitrogen and oxygen content; the effect of the dwell time is small. Literature reports that during

carbonization polymethacrylates are mainly degraded to their monomers [139–142]. Polyacrylates, on the other hand, mainly undergo: (1) chain scission reactions, during which i.a. monomer, methacrylates, diesters, and dimers are formed, and (2) (non-)radical reactions, during which i.a. olefins, alkenes, long chain alcohols, anhydrides, and crosslinks are formed. The scission reactions are followed by free radical chain or transfer reactions, so both processes cannot be considered separately from each other [114, 137–143]. For the pyrolysis of both polymethacrylates and polyacrylates, light gases such as CO, CO_2, H_2O, CH_4, C_2H_6, CH_3OH, and C_2H_5OH are formed as well [114, 137, 139–141, 143]. It is furthermore reported that the diffusion of the degraded products influence the process as well [114, 141]. A higher temperature gives rise to more (non-)radical side-chain reactions over main-chain scission reactions and gives rise to more sp^2 carbon bonds than sp^3 carbon bonds [26, 74, 142, 144]. Polymers with longer alkyl chains and a higher crosslinking density are proven to be more stable due to a reduced mobility of radicals and, in consequence, a higher recombination probability. They also tend to undergo dehydrogenation more easily, forming alkenes [114, 138, 141]. The alkenes form a conductive conjugated network [26, 78]. The presence of these bonds are confirmed by the XPS fit of the carbonized sample (Figure 4.13). The C1s peak is asymmetric and centered around 284.5 eV, which is typical for C=C bonds. Furthermore, a $\pi - -\pi$ transition is present around 290.9 eV [26, 144, 145]. Overall, the outcome of carbonization of acrylate polymers is a complex process, which is difficult to predict, due to the variety of reactions that occur with different kinetics both consecutively and simultaneously [79, 114, 142].

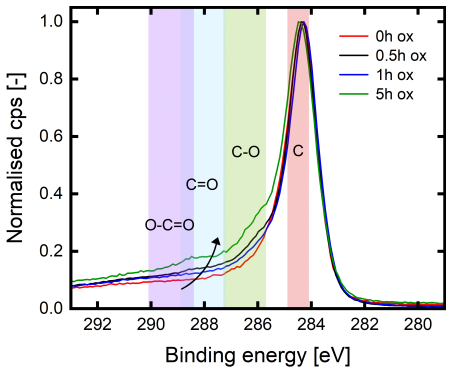

Figure 4.12: XPS C1s peak of carbonized electrodes with various dwell times in the second oxidation. The regions of typical carbon bond peaks are from Biesinger [136]

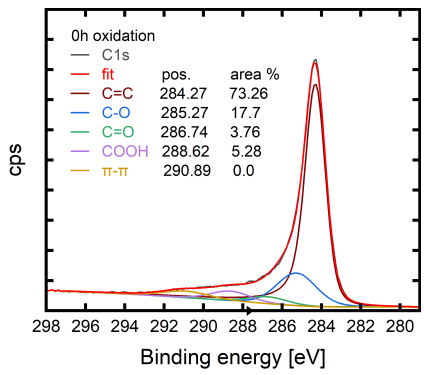

Figure 4.13: XPS C1s peak of electrode with no second oxidation. Fit is based on a XPS fit of a carbon electrode.

Surface visualization

During the carbonization a shrinkage is caused by both the release of gaseous products and by the compressive forces caused by the crosslinking [24, 26]. This can be seen in the surface images of thermally treated electrodes (Figure 4.14). Due to a limited availability of carbonized electrodes, both horizontally and vertically printed electrodes (indicated with red and blue frames respectively) were treated with a second oxidation. A shrinkage took place after the carbonization

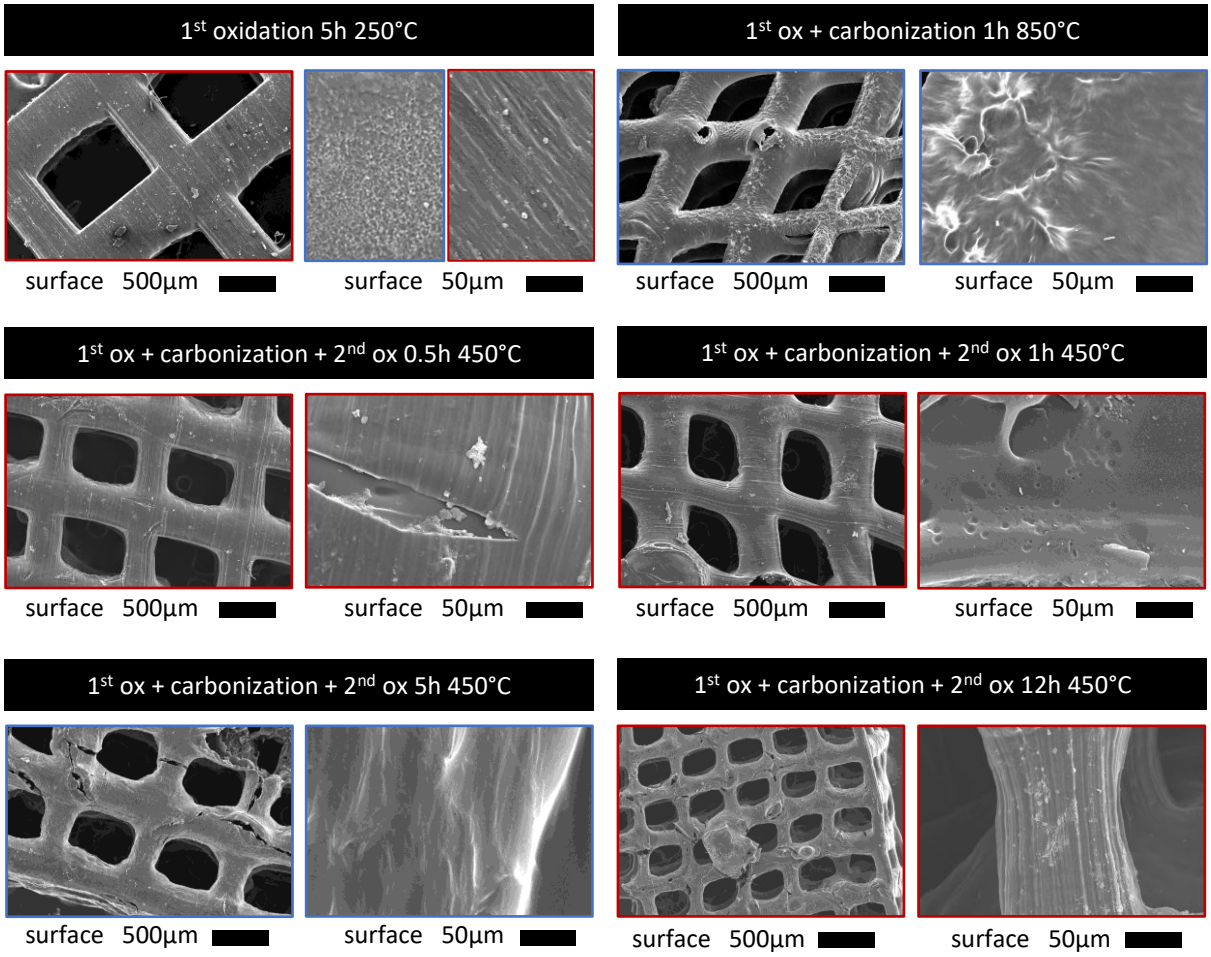

Figure 4.14: Surface image taken with a SEM with a 50× and 500× magnification of thermally treated electrodes printed with the High Temp V2 resin. Horizontally printed electrodes are indicated in red, vertically in blue.

and second oxidation with a dwell time of both 5 h and 12 h. The shrinkage is non-isotropic because the deformation is not the same in every direction. Furthermore, intrinsic stress on the matrix resulted in fracture of some rods. In the center of the rods in the carbonized sample (top right) it appears as if mass is pushed from the bulk outwards to the surface due to forces acting upon it during the shrinkage. This effect is even more pronounced in the carbonization with a dwell time of 5 h (see Appendix D). The same sort of deformations after the carbonization of PETA are reported in the work of Rezaei et al. [26]. The cause of the deformation can be ascribed to the high pressure of the trapped gaseous products acting on the polymer matrix. As the carbonization progresses the amount of gases and thus the pressure increases, and in consequence the matrix expands or bursts open [26, 73, 74].

Carbonization and oxidation decrease the roughness of the surface (Figure 4.14). After the first oxidation (top left) the dots on the surface created during the polymerization are still visible, but on the edges already slightly smoothened. During the carbonization (top right) and second oxidation of 5 h (bottom left) the details vanish even more. This effect is most likely caused by loss of material during the thermal treatment, in combination with a gradual release of gases (a fast and explosive release would lead to deformations) [26, 73, 74]. The relative increase of

the nitrogen content for longer oxidation confirms this, as it shows that more carbon and oxygen containing material is lost. However, thermal oxidative treatments are often used to increase the surface area of an carbon electrode [18]. This contradiction could be due to the very high oxidation temperature (450 °C): Greco et al. [73] found that an oxidation at ≥450 °C of their electrode increased the smoothness of the surface and decreased the surface area. They found that the content loss due to oxidative decomposition and a decrease in molecular disorder due to sp^2 hybridization affected the surface and surface area more significantly than the chemical change of the electrode surface through the formation of oxygen functional groups [73].

Changes in physical properties

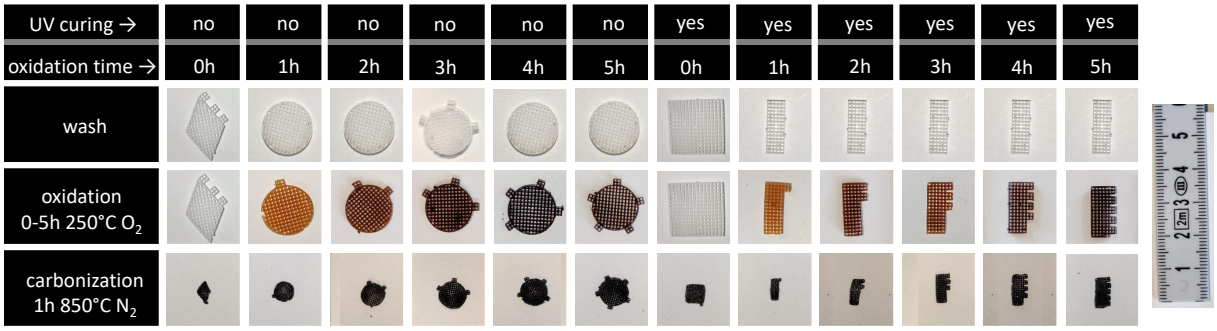

Figure 4.15: Images of samples after washing, oxidation, and carbonization (rows) for various pretreatments (columns). The pre-treatments include optional UV curing and different dwell times for oxidation at 250 °C.

Figure 4.15 shows how the heat treatments (rows) affect 3D-printed samples treated with different UV curing options and oxidation dwell times (columns). Images of samples for three other carbonization treatments can be seen in Appendix D. Upon heat application their color changes to a brown and eventually black tone. The size and weight of the sample decrease during the carbonization, and the shrinkage is not uniform throughout the shape: non-isotropic shrinkage is visible in the straight lines of the diamond, square, and rectangular shaped samples. It is not possible to ascribe this observation to the effect of the UV curing treatment, since circular shapes can handle compressive strength in all directions better than linear shapes [146]. A longer oxidation dwell time does however clearly result in a darker color after oxidation and a smaller linear shrinkage after carbonization.

The trends of the linear shrinkage and weight decrease of various thermal treatments can be seen in respectively the left and middle graphs of Figure 4.16. The length and weight of the samples were measured before and after the thermal treatments and are presented relative to their values after only washing. A longer oxidation dwell time results in a smaller overall linear shrinkage and a less weight loss after the carbonization. The linear shrinkage is, on average, 65% for the samples which did not undergo a thermal oxidation, and 40% for the samples which were heated in air for 5 h. The weight loss ranges from on average 96% for the non-thermally pretreated samples to 91% for the samples oxidized for 5 h. These results are in line with the trends reported in literature [26, 74, 142]. Rezaei et al. [26] report a linear shrinkage of 59.67% and a weight

reduction of 95.22% in their samples carbonized at 900 °C. The effect of the heat treatments on the electrical resistance is given in the right graph of Figure 4.16, in which the resistance of the carbonized sample is presented relative to the normalized resistance of a Freudenberg paper. The carbonization temperature has a clear effect on the electrical conductivity. The electrical resistance of the samples carbonized at 850 °C is 1.3 to 4.3 times higher compared to that of the Freudenberg paper, while the resistance of the samples carbonized at 650 °C is ~1000 to ~20000 times higher. The carbonization dwell time does not seem to have a significant effect, although a longer oxidation dwell time seems to be beneficial for the conductivity in the sample, as the resistance slightly decreases. Literature research on the carbonization of polymer materials confirms these trends: a higher temperature has a significant influence on the conductivity, and a longer dwell time and a slower ramp rate also have a positive effect [24, 26, 74]. Overall, the results clearly indicate that a carbonization at 650 °C does not make the material conductive, so it was decided to continue with carbonization at 850 °C for manufacturing the electrodes. The dwell time is set to 1 h – there is in these results not a clear beneficial effect for a longer dwell time, and a shorter dwell time is the most energy friendly option. The oxidation dwell time is set to 5 h to minimize the loss in size and weight and to minimize the electrical resistance.

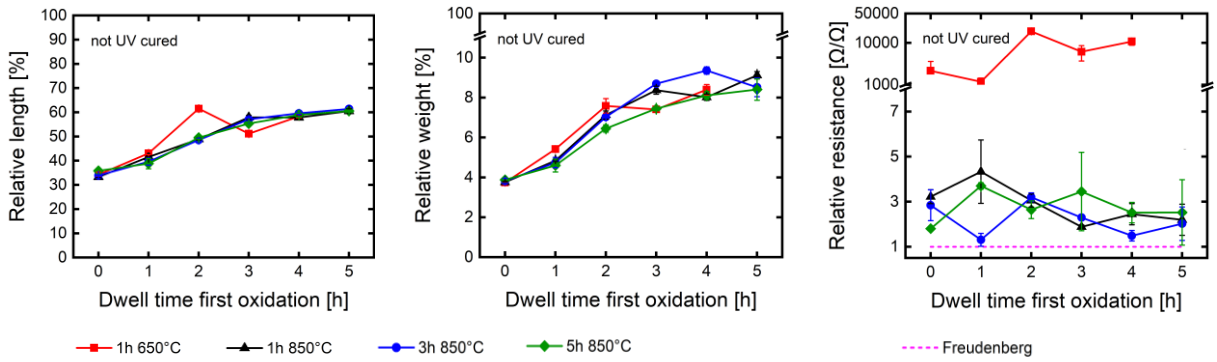

Figure 4.16: The effect of the oxidation dwell time (x axis) and the dwell time and temperature of the carbonization (lines) on the treated samples. The length and weight of the carbonized samples are given relative to untreated length and weight. The resistance is plotted relative to that of a Freudenberg paper. Note that the relative resistance is plotted linearly for low ratios, but logarithmically for high ratios.

The effect of the dwell time of the first oxidation on the extent of the shrinkage and weight loss can be explained by a few oxidative processes. First, thermal oxidation gives rise to crosslinking, which allows the polymer matrix to already rearrange itself into a more stable form. The covalent bonds formed between separate polymer chains as a result of crosslinking increase the mechanical strength of the polymer matrix, but also increase brittleness and reduce the elongation of deformation [75, 114, 141]. Furthermore, the reduction in chain mobility due to the crosslinking increases the chance of recombination of radicals [114]. Another process that can influence the extent of shrinkage and weight loss of the samples is the diffusion of the formed gaseous products out of the polymer matrix. The gaseous products can leave the matrix easier and in a less explosive way during the oxidation than during the carbonization, because the matrix is not highly crosslinked yet and because the diffusion is lower due to the lower temperature [74,

114, 142]. Although the exact influence of the diffusion of gaseous products out of the polymer is not known, literature does report that the diffusion of oxygen and the volatile products do affect the degradation kinetics of the polymer [74, 114, 142]. Moreover, a polymer matrix that is more densely crosslinked due to an oxidation treatment is proven to be stronger during the degassing of the products formed during the carbonization, resulting in a smaller shrinkage, less mass loss and less deformations [26]. A higher concentration of crosslinking density induced by the oxidation is beneficial for the conductivity of the sample as well. Upon carbonization, the polymer chains become conductive due to the conjugated double bonds of the formed alkenes. The additional crosslinking gives rise to an even better connected matrix, which results in a better conduction of electrons. Furthermore, less deformations in the matrix are beneficial as well, since those deformations form a blockage for the electrons [24, 26, 74]. This is because the matrix of the polymer is better packed and better connected. Upon carbonization, the polymer chains become conductive due to the conjugated double bonds of the formed alkenes [26, 74, 144]. The additional crosslinking gives rise to a even better connected matrix, which results in a better conduction of electrons [24, 26, 74]. Furthermore, less deformations in the matrix are beneficial as well, since those deformations form a blockage for the electrons [24, 26, 74].

The effect of the dwell time and operating temperature of the carbonization on the linear shrinkage and weight decrease appears to be minimal on the size and weight of the samples. At 650 °C (or even lower temperatures) the pyrolysis phase is already completed and the pyrosynthesis phase has started. Thus, the majority of the mass of the polymer is already lost due to dehydrogenation, polymer degradation and release of gaseous products. A further increase in the temperature or dwell time does then not have an additional effect on the mass loss. A higher temperature does then only give rise to cracking and annealing of carbon molecules, and reactions such as cyclization, condensation, hydrogen transfer and isomerization [26, 79]. The effect of the dwell time and temperature is on the contrary very significant for the conductivity of the sample. The higher temperature of the carbonization is favorable for dehydrogenation reactions in which alkenes are formed. This increases the sp^2/sp^3 hybridization ratio in the polymer matrix (Figure 4.13) [24, 26, 73, 74, 144]. As a consequence, the ability of electrons to move through the matrix is enhanced. These highly endothermic reactions occur more pronounced since more heat is available for the scission and recombination of C–C and C–H bonds. The beneficial effect of a higher temperature and/or dwell time of the carbonization is observed in literature as well [24, 26, 73, 79, 138, 144].

Wettability and absorption of water

Due to the low density of the carbon electrodes, wetting could only be studied qualitatively by having them in a vial filled with water on a rolling bench for six days. After a few days of being immersed in water, some of the electrodes had sunk to the bottom, while other had not (Figure 4.17). None of the not-oxidized electrodes sank. The electrodes which did not sink did

float just below the surface however. This indicates that the electrodes do wet with water – if they had been very hydrophobic they floated on top of the surface [78]. The electrodes furthermore absorb water, and they absorb more if they are oxidized (Figure 4.18). The absorption explains why some electrodes sank: their density simply increased. This process did happen for the highly oxidized samples (i.e. 12 h) faster. The results can easily be explained using surface chemistry of carbon electrodes. Carbon and graphite materials are neutral towards water; carbon felt electrodes have for instance a contact of 80–90° with water [73]. Wetting improves however with the introduction of oxygen containing functional groups and with higher O/C ratios. An oxidative thermal treatment is the most commonly used method to achieve this [18, 19, 73].

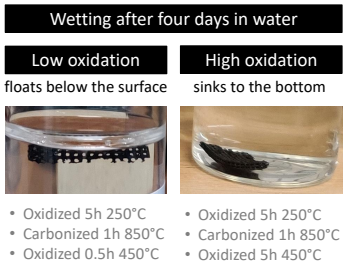

Figure 4.17: Wetting of electrodes after four days in water

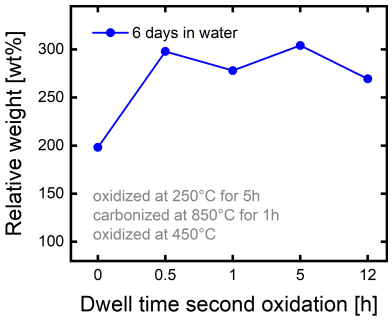

Figure 4.18: Weight increase of an electrode after six days in water due to absorption of water

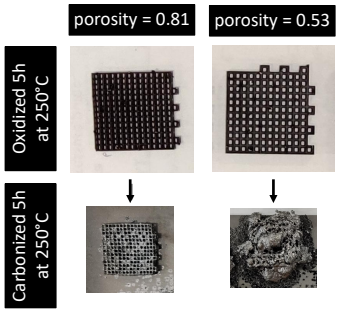

Figure 4.19: Deformation of oxidized samples after carbonization

Deformation of the sample on macroscale

The change in shape of an electrode during the carbonization is not only determined by the material and treatments used, but also by its structure. If the porosity is too low, then the electrode will blow up (Figure 4.19). This is caused by the eruption of trapped gaseous products inside the polymer matrix formed during the carbonization. If the porosity is too small, or the rod is too thick, then the gas cannot easily diffuse to the surface. Hence, it stays trapped in a bubble inside the matrix, and bursts out when the pressure becomes too high [26, 74]. A square grid with holes with a length of 0.9 mm and square rods with a thickness of 0.3 mm is the best option, because it holds shape and has the highest surface area with the lowest porosity.

4.4. Electrochemical performance

In this section the performance of the printed and carbonized electrodes in a single electrolyte flow cell is explored. With a single electrolyte set-up one redox couple is both reduced at one electrode and oxidized at the other. As a consequence, the OCV is near 0 V, and the measured polarization curve is, upon an applied current, the sum of the charge, ohmic, and mass transfer overpotentials [18, 71]. The tubular oven went out of operation during this thesis, so only a limited amount of electrodes could be made and tested in a flow cell. Nonetheless, the first results already give some insight on the viability of this method. All the tested electrodes had

square rods of 0.3 mm thick in a grid with holes of 1.0×1.0×0.5mm large (XYZ). The square, triangle, cylinder, and helix shaped electrodes were printed and oxidized successfully, but could unfortunately not be carbonized and thus not be tested.

Non-aqueous redox flow cell

The iR_Ω corrected polarization curves of oxidized and carbonized electrodes printed horizontally and vertically in a non-aqueous symmetrical flow cell show that a current is generated, and that the electrodes thus works (Figure 4.20, left, measured in duplo). At an applied voltage of 0.1 V a current density of 20.2–44.2 mA m^{-2} for the horizontal electrode and a current density of 20.8–47.8 mA m^{-2} for the vertical electrode was measured for an inlet velocity of 0.5–5.0 cm s^{-1} respectively. This is roughly a factor ten lower compared to a commercial electrode: a Freudenberg H23 paper has a current density of 290 mA m^{-2} for a superficial velocity of 1.5 cm s^{-1} at 0.1 V with 0.25 M TEMPO/$TEMPO^+$ (so 2.5× more concentrated that the cells used in this work) [18]. At this voltage there are no mass transfer limitations in the cells with the printed electrodes and the Freudenberg papers [18]. The difference in performance can be attributed to differences in surface area; the surface of the printed and carbonized electrodes is rather smooth (Figure 4.22), which reduces the surface area and thus the overall conversion of the redox couple. An increase in the surface area could make these electrodes competitive with the commercial ones on the market [18, 19, 55].

The intercept of the horizontal axis of the impedance measurement (Figure 4.20, middle) shows that the cell specific resistance lies around 1.84 Ω and 1.15 Ω for the horizontal and vertical electrode respectively. The diameter reveals that the resistance increases with 2.0 Ω, 1.54 Ω and 0.64 Ω for the horizontal and with 1.9 Ω, 1.4 Ω and 0.48 Ω for the vertical electrode at 0.5 cm s^{-1}, 1.5 cm s^{-1} and 5.0 cm s^{-1} respectively due to charge transfer and mass transfer overpotentials [71]. It was not possible to make a proper resistance fit on this impedance curve, so the contributions of the activation and mass transfer overpotential could not be found. Lower resistances are reprted for commercially available electrodes: the Freudenberg paper has a cell resistance of 0.62 Ω and a charge and mass transfer resistance of 0.78 Ω at a superficial velocity of 1.5 cm s^{-1} [18]. This can once more be attributed to the lower surface area, which gives rise to a higher charge transfer resistance [71].

An increase of superficial velocity results in a higher current density for a given voltage, and this effect is accompanied with a lower mass and charge transfer resistance (Figure 4.20): an increase of electrolyte velocities gives rise to a more convective mass transfer over a diffusive mass transfer. Hence, the active species are replenished in the bulk faster, which in turn enhances the diffusion and increases the concentration of the species near the electrode's surface. Furthermore, the boundary layer in which diffusion and migration takes place becomes thinner upon a more turbulent convective flow. This effect reduces the mass transfer overpotential[18, 54, 55, 71]. No limiting current density is observed yet at every applied velocities, but the increase in

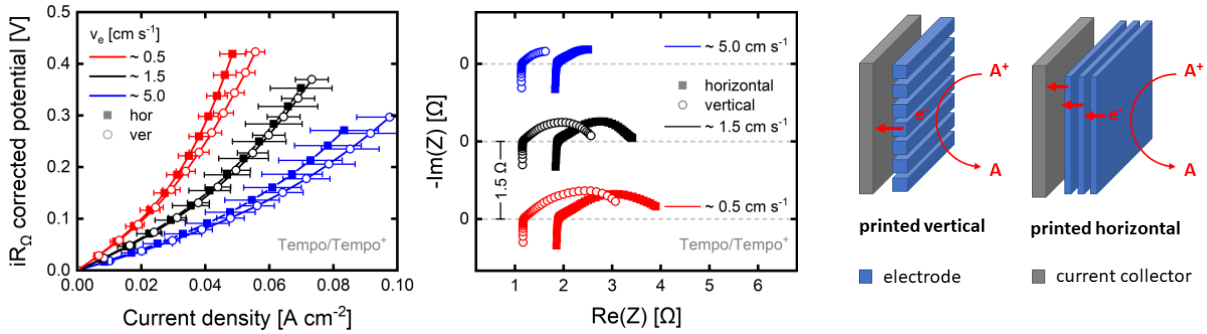

Figure 4.20: Electrochemical performance in an iR_Ω corrected polarization curve (left) and Nyquist plot (middle) of a non-aqueous symmetrical flow cell (0.1 M TEMPO/TEMPO$^+$) with electrodes printed horizontally and vertically, operated at a superficial velocities of 0.5 cm s^{-1}, 1.5 cm s^{-1}, and 5.0 cm s^{-1}; schematic illustration of the effect of the isotropicity of the printed electrodes on the conductivity (right).

polarization does show that mass transfer limitations start to act up, and this effect is more severe for a decrease in velocity. Furthermore, it is hypothesized that the different shaped rods and grids of the electrode will enhance static mixing and thus enhance the mass and charge transport. Unfortunately, this could effect not be investigated. A more detailed study on influence of these printed electrodes on the means of transport is thus recommended.

The print direction and the corresponding anisotropic alignment does affect the electrochemical performance of the electrode. The polarization curve is slightly steeper for the horizontally printed electrode compared to the vertically printed electrode (Figure 4.20, left), and the ohmic resistance is significantly higher (Figure 4.20, middle). The electrodes which are printed horizontally have the printed layers aligned parallel to the contact face of the current collector. Hence, electrons need to pass a few layers in order to travel from the surface of the electrode to the surface of the current collector (Figure 4.20, right). The electrodes which are printed vertically have their layers aligned perpendicular with respect to the contact face of the current collector. In this case, the electrons only have to travel through one layer (Figure 4.20, right). The connection between layers between the electrode surface and the current collector thus imposes and additional resistance for the electrode. J. Zhang et al. [84] reports similar results for extrusion based 3D prints, in which the resistance against electron transport is remarkably affected by the anisotropicity alignment of the print. They found that both voids and imperfections between adjacent layers reduced the conductivity [84].

Aqueous redox flow cell

The electrochemical assessment of the oxidized, carbonized and either non-oxidized or oxidized electrodes looks promising as well (Figure 4.21, left). However, the resistance in both cells increased over time, which can be seen in the impedance obtained at different velocities conducted in series (Figure 4.21, middle), and of the EIS performed both before and after one polarization curve (Figure 4.21, right). Only one experiment could be conducted, so it is not possible to draw conclusion on this phenomenon yet. Possible hypotheses could be that the electrolyte solution

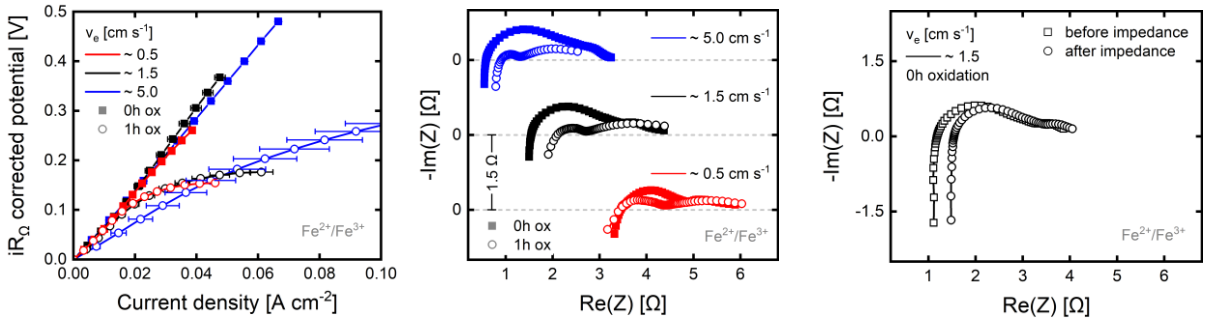

Figure 4.21: Electrochemical tests of oxidized and non-oxidized electrodes in an aqueous symmetric flow cell with on the left a iR_Ω corrected polarization curve, in the middle a Nyquist plot of the EIS at various velocities, and on the right a Nyquist plot of two EIS measurements before and after one conducted polarization curve.

was not stable, that the electrodes got too damaged during the assembly, that the redox couple reacted with the electrode, that the cell relaxed due to swelling of the electrodes, or just simply that this specific experiment was flawed. XPS data does not show significant changes due to a possible reaction of the redox couple on the elemental composition of the surface: merely 0.18% Fe was detected on the surface of the 1 h oxidized electrode, and no Fe was detected on the 1 h electrode. More research is needed to investigate whether the resistance will increase in duplicate experiments, and if so, what causes it.

Surface corrosion

The surface of the electrodes which are merely oxidized and carbonized used in the aqueous and non-aqueous flow cells were examined (Figure 4.22). Deposition of material is visible on the electrode used in TEMPO/TEMPO$^+$ (left), but not on the electrode used in $Fe^{2+}/Fe_3{}^+$ (right). Damage of the structure can be seen in the electrode used in the aqueous cell, this is caused by the pressure applied during the assembly. It is not very likely that electrochemical oxidation occurs; organic solvents and redox couples are in general very stable, and significant potentials are needed to oxidize carbon in water [147].

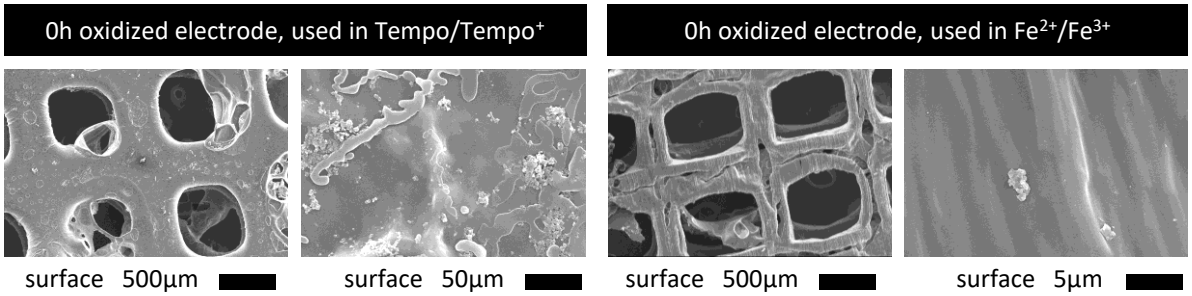

Figure 4.22: Surface image of thermally treated electrodes without a second oxidation used in an non-aqueous redox flow cell (left) and aqueous redox flow cell (right).

Chapter 5. Conclusion and outlook

The conclusions and recommendation for future research are presented here per section.

3D printing

The electrodes were succesfully printed with the SLA based printer of Form3. Whilst the print precision of Form 3 was good, the accuracy was found to be poor for very small prints: holes with a set diameter of 250–1000 µm were printed with a diameter that was 147±46 µm smaller than set; pins with a set diameter of 80–250 µm were printed on average with a diameter of 250±9.5 µm. The measured deviations got smaller when the diameter increased, but they remained significantly large for the printed holes. Furthermore, it was found that not all holes could be printed successfully, as they either were significantly smaller size or were completely polymerized. Only holes with a diameter ≥ 500 µm could be printed with a 100% success rate. Holes which were placed closer to each other were printed with less success than those which had a larger spacing. The observed deviations impose thatm in the electrode design, the holes and rods need to have a size of at least 500 µm and 250 µm large respectively. Based on a review of literature regarding the factors affecting the performance of the printer two phenomena could be indicated as the presumable explanation for the observed deviation in accuracy. The first cause could be a randomly distributed uncontrolled polymerization or extensive crosslinking of the polymer outside the laser spot. This may include the presence of oligomers in the resin, but due to the trade secrecy of the resin no conclusive statement can be made. The second cause regards the optical phenomena such as scattering and refraction arising from the interaction with the UV laser and the hardware and/or resin. If the latter one is indeed influential, then it is likely that the addition of a porogen in the resin will decrease the accuracy due to an altered of the refractive index of the resin or an increased light scattering on the porogen. Further research towards the effect of the randomly distributed uncontrolled polymerization on the accuracy of the printer could be performed by adding a polymerization inhibitor. If the inhibitors increase the accuracy and success rate of the polymerized holes, then this factor can be deemed as causative factor. The effect of light scattering and refraction can be studied with the addition of the porogen; if optical phenomena do cause a deviation in accuracy, then the addition of a porogen would decrease the accuracy.

Microporosity via polymerization-induced phase separation

The introduction of micropores in a highly crosslinked polymer was successfully done via a polymerization-induced phase separation. Two porogens were investigated, of which 1-decanol produced pores and cyclohexanol did not. The pores only became visible when ≥20 wt% 1-decanol was added to the monomer mixture. A TGA revealed that the porogen concentration in the polymer matrix was lower than the concentration of the porogen added to the monomer resin. After the polymerization, porogen was present on the surface of the polymer, indicating that it not only separated into agglomerates in the matrix, but also separated outside of the

matrix. This effect is presumably caused by the phase separation, but can also be enhanced by the shrinkage of the polymer matrix, pushing the porogen out of the agglomerates. The porogen extraction was accomplished when washed with acetone and evaporated at higher temperatures under vacuum. Other solvents did, based on the TGA, extract the porogen as well, but did not show pores on the surface in a visual analysis with the SEM. This is most likely caused by the formation of a layer of material near or on top of the surface. A possible explanation could be that the solvent experiences a high resistance to diffuse towards the surface, especially when the concentration decreases. The solvent then gathers just below the surface. Future research on the formation of layer could include XPS. The successful extraction and evaporation of the porogen with acetone was attributed to its ability to form hydrogen bonds with the porogen. The evaporation of the solvent at elevated temperatures under the presence of oxygen diminished the rough surface created by the pores. This can presumably be attributed to the an oxidative reaction or degradation of the polymer. After the extraction the polymer was more brittle, and would in some cases brake upon touch. Hence, it was decided to continue with PETA + 20 wt% 1-decanol. A few things need to be investigated in order to improve this method. PETA could be mixed with a monomer with a lower functionality, so that the evaporation of the solvent becomes easier and that the brittleness reduces. The size and the functional group of the porogen can be varied as well; it is advised to investigate the interaction with the porogen and monomer first with a ternary diagram. Furthermore, different extraction methods can still be tested, such as supercritical drying in CO_2 at 50 bar. However, based on the results it is not advised to continue with this method for the introduction of microporosity for the electrodes: the pores in the bulk make the polymer matrix brittle, and the separation of porogen outside the polymer into the resin would change the composition of resin in the printer over time. Hence, it is suggested that other methods, such as etching, should be explored to increase the surface area of the electrode.

Thermal treatments

3D printed electrodes were successfully made conductive and electrocatalytic by means of thermal treatments. A higher dwell temperature of the first oxidation at 250 °C resulted in a smaller shrinkage, a lower weight loss, and a slightly higher conductivity of the electrode after the carbonization. This is most likely caused by the oxidative crosslinking, which increases the strength of the polymer matrix. A higher temperature during the carbonization improved the conductive properties of the material greatly; there was no clear effect of the dwell time. The carbonized electrodes wetted with water and absorbed water, and a second oxidation improved both properties. Both the carbonization and the second oxidation reduced the surface roughness of the electrodes. This is can be attributed to the oxidative decomposition of material on the surface and the increase in sp^2 hybridization. Furthermore, it was established that the electrodes should have rods of 300 µm thick and holes of 0.9 mm wide in order to prevent strong deformations due to explosion of trapped gas. Various reaction mechanism during the oxidation and carbonization and their effect on the properties of the polymer matrix were identified with a

literature study. For future research it is important that the mechanical strength and the surface area of the thermally treated electrodes is studied and improved. Such an improvement could be realized with the development of a better resin or with a more suitable configuration of the thermal treatments used. It is hypothesized that the addition of a shock absorber in the polymer could have a positive effect on the mechanical strength. Carbonization at a higher temperature reportedly improves the conductivity and electrocatalytic performance of the electrode. The effect of the temperature and dwell time of the second oxidation on the surface area, wetting and electrocatalytic activity of the electrode needs to be studied more indepth as well. Other treatments such as etching are also interesting to consider. Raman spectroscopy could be used improve the analysis of the chemical composition of the electrode.

Electrochemical performance of a printed electrode

Electrochemical tests of the printed and thermally treated electrodes in an aqueous cell (Fe^{2+}/Fe^{3+}) and non-aqueous cell (TEMPO/$TEMPO^{+}$) showed that the electrodes enabled the electrochemical reaction to run, and that they thus work as required. The experiment performed in the aqueous cell showed strange deviations that could not be explained, so a duplo and triplo experiment is greatly advised. The polarization curve of the non-aqueous cell lies around 10× higher than of the commercial Freudenberg paper electrode. This can be attributed to the low surface area of the electrodes; other possible influences still need to be indicated with more duplo and triplo experiments. No limiting current density was observed for the superficial velocities, but the mass transport did already decrease for higher applied potentials. The studied anisotropicity of the printed electrodes affects the electrochemical performance: the electrodes with the layers printed perpendicular to the surface of the current collector exhibited lower ohmic resistances and a consequently a less steep polarization curve than those with the layer printed parallel to the current collector. The effect of the shape of the rods and the structure of the grid on the mass transport in the redox flow cell should be further studied. Electrodes with different shaped rods were successfully printed, but could unfortunately not be tested. Simulations with altered structures shows promising results regarding static mixing and enhanced mass transport [36, 37].

Overall recommendations

This works has shown that the 3D printed electrodes work in a redox flow battery. The possibility to tune the macro-porosity and enhance mass transport by means of static mixing gives this method great potential, for both academics and commercial application. Great advances still must be made in the improvement of the material and structure of the electrodes. The small resolution of SLA printing and the brittleness from the thermal treatments could form a bottle neck in this manufacturing technique.

Bibliography

[1] IPCC. (2021). *Summary for policymakers of climate change 2021: The physical science basis*. https://www.ipcc.ch/report/ar6/wg1/downloads/report/IPCC_AR6_WGI_SPM.pdf

[2] IEA. (2019, October). *CO2 emissions from fuel combustion*. https://doi.org/10.1787/2a701673-en.

[3] IEA. (2021, May). *Net zero by 2050 - a roadmap for the global energy sector*. https://www.iea.org/reports/net-zero-by-2050

[4] Environmental and Energy Study Institute (EESI). (n.d.). *Climate change*. https://www.eesi.org/topics/climate-change/description

[5] Browne, M. P., Redondo, E., & Pumera, M. (2020). 3D printing for electrochemical energy applications. *Chemical Reviews*, *120*(5), 2783–2810. https://doi.org/10.1021/acs.chemrev.9b00783

[6] Hoegh-Guldberg, O., Jacob, D., Taylor, M., Bindi, M., Brown, S., Camilloni, I., Diedhiou, A., Djalante, R., Ebi, K. L., Engelbrecht, F., Guiot, J., Hijioka, Y., Mehrota, S., Payne, A., Seneviratne, S. I., Thomas, A., Warren, R. F., Zhou, G., & Tschakert, P. (2018). *Impacts of 1.5ºC global warming on natural and human systems*. https://www.ipcc.ch/sr15/chapter/chapter-3/

[7] United Nations. (n.d.). *The Paris agreement*. https://unfccc.int/process-and-meetings/the-paris-agreement/the-paris-agreement

[8] UNFCCC. (2016). *The Paris agreement*. https://unfccc.int/sites/default/files/resource/parisagreement_publication.pdf

[9] Ministerie van Economische Zaken, Landbouw en Innovatie. (2020, January 31). *Climate policy*. https://www.government.nl/topics/climate-change/climate-policy

[10] SEI, IISD, ODI, E3G, & UNEP. (2020). *The production gap report: 2020 special report*. http://productiongap.org/2020report

[11] Ibrahim, H., & Ilinc, A. (2013). Techno-economic analysis of different energy storage technologies. *Energy Storage - Technologies and Applications*. https://doi.org/10.5772/52220

[12] Vazquez, S., Lukic, S., Galvan, E., Franquelo, L. G., Carrasco, J. M., & Leon, J. I. (2011). Recent advances on energy storage systems. *IECON 2011 - 37th Annual Conference of the IEEE Industrial Electronics Society*. https://doi.org/10.1109/iecon.2011.6120075

[13] Alotto, P., Guarnieri, M., & Moro, F. (2014). Redox flow batteries for the storage of renewable energy: A review. *Renewable and Sustainable Energy Reviews*, *29*, 325–335. https://doi.org/10.1016/j.rser.2013.08.001

[14] van de Weijer, B. (2021). Energiebedrijven moesten in augustus soms een negatieve prijs hanteren op hun stroom. *de Volkskrant*. https://www.volkskrant.nl/nieuws-achtergrond/energiebedrijven-moesten-in-augustus-soms-een-negatieve-prijs-hanteren-op-hun-stroom~b5cb4cd4/

[15] Amelang, S., & Appun, K. (2018, November 26). *The causes and effects of negative power prices*. Retrieved October 25, 2021, from https://www.cleanenergywire.org/factsheets/why-power-prices-turn-negative

[16] Thakur, S., Gohil, G., & Balsara, P. T. (2021). Grid forming energy router: A utility interface for renewable energy sources and energy storage grid integration applications. *2021 IEEE Applied Power Electronics Conference and Exposition*, 680–686. https://doi.org/10.1109/apec42165.2021.9487096

[17] Krishan, O., & Suhag, S. (2018). An updated review of energy storage systems: Classification and applications in distributed generation power systems incorporating renewable energy resources. *International Journal of Energy Research*, *43*(12), 6171–6210. https://doi.org/10.1002/er.4285

[18] Forner-Cuenca, A., & Brushett, F. R. (2019). Engineering porous electrodes for next-generation redox flow batteries: Recent progress and opportunities. *Current Opinion in Electrochemistry*, *18*, 113–122. https://doi.org/10.1016/j.coelec.2019.11.002

[19] Weber, A. Z., Mench, M. M., Meyers, J. P., Ross, P. N., Gostick, J. T., & Liu, Q. (2011). Redox flow batteries: A review. *Journal of Applied Electrochemistry*, *41*(10), 1137–1164. https://doi.org/10.1007/s10800-011-0348-2

[20] Wan, C. T., Jacquemond, R. R., Chiang, Y., Nijmeijer, K., Brushett, F. R., & Forner-Cuenca, A. (2021). Non-solvent induced phase separation enables designer redox flow battery electrodes. *Advanced Materials*, *33*(16), 2006716. https://doi.org/10.1002/adma.202006716

[21] Wang, H., & Fokwa, B. P. T. (2019). *Inorganic battery materials*. Wiley.

[22] Zhang, H., Lu, W., & Li, X. (2019). Progress and perspectives of flow battery technologies. *Electrochemical Energy Reviews*, *2*(3), 492–506. https://doi.org/10.1007/s41918-019-00047-1

[23] Aaron, D., Tang, Z., Papandrew, A. B., & Zawodzinski, T. A. (2011). Polarization curve analysis of all-vanadium redox flow batteries. *Journal of Applied Electrochemistry*, *41*(10), 1175–1182. https://doi.org/10.1007/s10800-011-0335-7

[24] Lee, J. A., Lee, S. W., Lee, K. C., Park, S. I., & Lee, S. S. (2008). Fabrication and characterization of freestanding 3D carbon microstructures using multi-exposures and resist pyrolysis. *Journal of Micromechanics and Microengineering*, *18*(3), 035012. https://doi.org/10.1088/0960-1317/18/3/035012

[25] McCreery, R. L. (2008). Advanced carbon electrode materials for molecular electrochemistry. *Chemical Reviews*, *108*(7), 2646–2687. https://doi.org/10.1021/cr068076m

[26] Rezaei, B., Pan, J. Y., Gundlach, C., & Keller, S. S. (2020). Highly structured 3D pyrolytic carbon electrodes derived from additive manufacturing technology. *Materials & Design*, *193*, 108834. https://doi.org/10.1016/j.matdes.2020.108834

[27] Steldinger, H., Esposito, A., Brunnengräber, K., Gläsel, J., & Etzold, B. J. M. (2019). Activated carbon in the third dimension — 3D printing of a tuned porous carbon.

Advanced Science, *6*(19), 1901340. https://doi.org/10.1002/advs.201901340

[28] Egorov, V., Gulzar, U., Zhang, Y., Breen, S., & O'Dwyer, C. (2020). Evolution of 3D printing methods and materials for electrochemical energy storage. *Advanced Materials*, *32*(29), 2000556. https://doi.org/10.1002/adma.202000556

[29] Huong Le, T. X., Bechelany, M., & Cretin, M. (2017). Carbon felt based-electrodes for energy and environmental applications: A review. *Carbon*, *122*, 564–591. https://doi.org/10.1016/j.carbon.2017.06.078

[30] Fleming, G. J., & Fleming, P. J. (2001, January). *Development and optimization of porous carbon papers suitable for gas diffusion electrodes. Final report, December 2000*. Spectracorp Ltd., Lawrence, MA (US). https://doi.org/10.2172/809960

[31] Mathur, R. B., Maheshwari, P. H., Dhami, T. L., Sharma, R. K., & Sharma, C. P. (2006). Processing of carbon composite paper as electrode for fuel cell. *Journal of Power Sources*, *161*(2), 790–798. https://doi.org/10.1016/j.jpowsour.2006.05.053

[32] Bhatt, P., & Goe, A. (2017). Carbon fibres: Production, properties and potential use. *Material Science Research India*, *14*(1), 52–57. https://doi.org/10.13005/msri/140109

[33] ZOLTEK. (2017, October 24). *How is carbon fiber made?* Retrieved October 28, 2021, from https://zoltek.com/carbon-fiber/how-is-carbon-fiber-made/

[34] Zhang, X. (2008). Hydroentangling: A novel approach to high-speed fabrication of carbon nanotube membranes. *Advanced Materials*. https://doi.org/10.1002/adma.200801919

[35] Mohammadzadeh Kakhki, R. (2019). A review to recent developments in modification of carbon fiber electrodes. *Arabian Journal of Chemistry*, *12*(7), 1783–1794. https://doi.org/10.1016/j.arabjc.2014.11.058

[36] Dussi, S., & Rycroft, C. H. (2022). Less can be more: Insights on the role of electrode microstructure in redox flow batteries from 2D direct numerical simulations. *Physics of Fluids*. https://doi.org/10.48550/arXiv.2201.00423

[37] Beck, V. A., Ivanovskaya, A. N., Chandrasekaran, S., Forien, J. B., Baker, S. E., Duoss, E. B., & Worsley, M. A. (2021). Inertially enhanced mass transport using 3D-printed porous flow-through electrodes with periodic lattice structures. *Proceedings of the National Academy of Sciences*, *118*(32), e2025562118. https://doi.org/10.1073/pnas.2025562118

[38] Salonitis, K. (2014). Stereolithography. *Comprehensive materials processing* (pp. 19–67). Elsevier. https://doi.org/10.1016/B978-0-08-096532-1.01001-3

[39] Low, Z. X., Chua, Y. T., Ray, B. M., Mattia, D., Metcalfe, I. S., & Patterson, D. A. (2017). Perspective on 3D printing of separation membranes and comparison to related unconventional fabrication techniques. *Journal of Membrane Science*, *523*, 596–613. https://doi.org/10.1016/j.memsci.2016.10.006

[40] Bélanger, D., & J, P. (2011). Electrografting: A powerful method for surface modification. *Chemical Society Reviews*, *40*(7), 3995. https://doi.org/10.1039/c0cs00149j

[41] Doeff, M. M., Kostecki, R., Wilcox, J., & Lau, G. (2007). *Conductive carbon coatings for electrode materials* (No. 39). https://doi.org/10.2172/925590

[42] Ouyang, B., Zhang, Y., Xia, X., Rawat, R. S., & Fan, H. J. (2018). A brief review on plasma for synthesis and processing of electrode materials. *Materials Today Nano*, *3*, 28–47. https://doi.org/10.1016/j.mtnano.2018.11.002

[43] Hoyer, B., Sørensen, G., Jensen, N., Nielsen, D. B., & Larsen, B. (1996). Electrostatic spraying: A novel technique for preparation of polymer coatings on electrodes. *Analytical Chemistry*, *68*(21), 3840–3844. https://doi.org/10.1021/ac9605509

[44] Wang, C., & Madou, M. (2005). From MEMS to NEMS with carbon. *Biosensors and Bioelectronics*, *20*(10), 2181–2187. https://doi.org/10.1016/j.bios.2004.09.034

[45] Quang, L. N., Halder, A., Rezaei, B., Larsen, P. E., Sun, Y., Boisen, A., & Keller, S. S. (2019). Electrochemical pyrolytic carbon resonators for mass sensing on electrodeposited polymers. *Micro and Nano Engineering*, *2*, 64–69. https://doi.org/10.1016/j.mne.2019.01.001

[46] Kim, K. J., Kim, Y. J., Kim, J. H., & Park, M. S. (2011). The effects of surface modification on carbon felt electrodes for use in vanadium redox flow batteries. *Materials Chemistry and Physics*, *131*(1-2), 547–553. https://doi.org/10.1016/j.matchemphys.2011.10.022

[47] Dong, Z., Cui, H., Zhang, H., Wang, F., Zhan, X., Mayer, F., Nestler, B., Wegener, M., & Levkin, P. A. (2021). 3D printing of inherently nanoporous polymers via polymerization-induced phase separation. *Nature Communications*, *12*(1). https://doi.org/10.1038/s41467-020-20498-1

[48] Lee, H., Yoo, J. K., Park, J. H., Kim, J. H., Kang, K., & Jung, Y. S. (2012). A stretchable polymer-carbon nanotube composite electrode for flexible Lithium-Ion batteries: Porosity engineering by controlled phase separation. *Advanced Energy Materials*, *2*(8), 976–982. https://doi.org/10.1002/aenm.201100725

[49] Jeon, J. W., Han, J. H., Kim, S. K., Kim, D. G., Kim, Y. S., Suh, D. H., Hong, Y. T., Kim, T. H., & Kim, B. G. (2018). Intrinsically micrporous polymer-based hierarchical nanostructuring of electrodes via non solvent-induced phase separation for high-performance supercapacitors. *Journal of Materials Chemistry A*, *6*(19), 8909–8915. https://doi.org/10.1039/c8ta02451k

[50] Yi, H., Li, D., Lv, Z., Li, R., Ling, M., Zhang, H., Zheng, Q., & Li, X. (2019). Constructing high-performance 3D porous self-standing electrodes with various morphologies and shapes by a flexible phase separation-derived method. *Journal of Materials Chemistry A*, *7*(39), 22550–22558. https://doi.org/10.1039/c9ta08845h

[51] Winter, M., & Brodd, R. J. (2004). What are batteries, fuel cells, and supercapacitors? *Chemical Reviews*, *104*(10), 4245–4270. https://doi.org/10.1021/cr020730k

[52] Arenas, L. F., Ponce de León, C., & Walsh, F. C. (2017). Engineering aspects of the design, construction and performance of modular redox flow batteries for energy storage.

Journal of Energy Storage, *11*, 119–153. https://doi.org/10.1016/j.est.2017.02.007

[53] Olson, M. V. (n.d.). *Oxidation-reduction reaction*. https://www.britannica.com/science/oxidation-reduction-reaction

[54] Petrovic, S. (2020). *Basic electrochemistry concepts. electrochemistry crash course for engineers*. Springer. https://doi.org/10.1007/978-3-030-61562-8_2

[55] Fuller, T. F., & Harb, J. N. (2018). *Electrochemical engineering*. Wiley. www.wiley.com/go/fuller/electrochemicalengineering

[56] Lumen. (n.d.). *Standard reduction potentials*. https://courses.lumenlearning.com/boundless-chemistry/chapter/standard-reduction-potentials/

[57] Zheng, Q., Xing, F., Li, X., Ning, G., & Zhang, H. (2016). Flow field design and optimization based on the mass transport polarization regulation in a flow-through type vanadium flow battery. *Journal of Power Sources*, *324*, 402–411. https://doi.org/10.1016/j.jpowsour.2016.05.110

[58] Forner-Cuenca, A., Penn, E. E., Oliveira, A. M., & Brushett, F. R. (2019). Exploring the role of electrode microstructure on the performance of non-aqueous redox flow batteries. *Journal of The Electrochemical Society*, *166*(10), A2230–A2241. https://doi.org/10.1149/2.0611910jes

[59] Winsberg, J., Hagemann, T., Janoschka, T., Hager, M. D., & Schubert, U. S. (2016). Redox-flow batteries: From metals to organic redox-active materials. *Angewandte Chemie International Edition*, *56*(3), 686–711. https://doi.org/10.1002/anie.201604925

[60] Bird, B. R., Stewart, W. E., & Lightfoot, E. N. (2001). *Transport phenomena* (2nd ed.). Wiley.

[61] Costentin, C., & Savéant, J. (2019). Concepts and tools for mechanism and selectivity analysis in synthetic organic electrochemistry. *Proceedings of the National Academy of Sciences*, *116*(23), 11147–11152. https://doi.org/10.1073/pnas.1904439116

[62] Ward, K., & Fan, Z. H. (2015). Mixing in microfluidic devices and enhancement methods. *Journal of Micromechanics and Microengineering*, *25*(9), 17. https://doi.org/10.1088/0960-1317/25/9/094001

[63] Lo, R. C. (2013). Application of microfluidics in chemical engineering. *Chemical Engineering & Process Techniques Cite*, *442*, 368–373.

[64] Regner, M., Östergren, K., & Trägårdh, C. (2006). Effects of geometry and flow rate on secondary flow and the mixing process in static mixers—a numerical study. *Chemical Engineering Science*, *61*(18), 6133–6141. https://doi.org/10.1016/j.ces.2006.05.044

[65] Mansour, M., Khot, P., Thévenin, D., Nigam, K. D., & Zähringer, K. (2020). Optimal Reynolds number for liquid-liquid mixing in helical pipes. *Chemical Engineering Science*, *214*, 114522. https://doi.org/10.1016/j.ces.2018.09.046

[66] Messaggi, M., Rabissi, C., Gambaro, C., Meda, L., Casalegno, A., & Zago, M. (2020). Investigation of vanadium redox flow batteries performance through locally-resolved polarisation curves and impedance spectroscopy: Insight into the effects of electrolyte,

flow field geometry and electrode thickness. *Journal of Power Sources*, *449*, 227588. https://doi.org/10.1016/j.jpowsour.2019.227588

[67] Xu, Q., Zhao, T. S., & Leung, P. K. (2013). Numerical investigations of flow field designs for vanadium redox flow batteries. *Applied Energy*, *105*, 47–56. https://doi.org/10.1016/j.apenergy.2012.12.041

[68] Ghanem, A., Lemenand, T., Della Valle, D., & Peerhossaini, H. (2014). Static mixers: Mechanisms, applications, and characterization methods – a review. *Chemical Engineering Research and Design*, *92*(2), 205–228. https://doi.org/10.1016/j.cherd.2013.07.013

[69] del Olmo, D., Pavelka, M., & Kosek, J. (2021). Open-circuit voltage comes from non-equilibrium thermodynamics. *Journal of Non-Equilibrium Thermodynamics*, *46*(1), 91–108. https://doi.org/10.1515/jnet-2020-0070

[70] Trovò, A., Picano, F., & Guarnieri, M. (2019). Comparison of energy losses in a 9 kW vanadium redox flow battery. *Journal of Power Sources*, *440*, 227144. https://doi.org/10.1016/j.jpowsour.2019.227144

[71] van der Heijden, M., & Forner-Cuenca, A. (2021). Transport phenomena and cell overpotentials in redox flow batteries. *Reference Module in Earth Systems and Environmental Sciences*. https://doi.org/10.1016/b978-0-12-819723-3.00132-3

[72] Yao, Y., Lei, J., Shi, Y., Ai, F., & Lu, Y. C. (2021). Assessment methods and performance metrics for redox flow batteries. *Nature Energy*, *6*(6), 582–588. https://doi.org/10.1038/s41560-020-00772-8

[73] Greco, K. V., Forner-Cuenca, A., Mularczyk, A., Eller, J., & Brushett, F. R. (2018). Elucidating the nuanced effects of thermal pretreatment on carbon paper electrodes for vanadium redox flow batteries. *ACS Applied Materials & Interfaces*, *10*(51), 44430–44442. https://doi.org/10.1021/acsami.8b15793

[74] Hassan, Y. M., Caviglia, C., Hemanth, S., Mackenzie, D. M. A., Alstrøm, T. S., Petersen, D. H., & Keller, S. S. (2017). High temperature SU-8 pyrolysis for fabrication of carbon electrodes. *Journal of Analytical and Applied Pyrolysis*, *125*, 91–99. https://doi.org/10.1016/j.jaap.2017.04.015

[75] Marin, E., Boschetto, F., Zanocco, M., Doan, H. N., Sunthar, T. P. M., Kinashi, K., Iba, D., Zhu, W., & Pezzotti, G. (2021). UV-curing and thermal ageing of methacrylated stereo-lithographic resin. *Polymer Degradation and Stability*, *185*, 109503. https://doi.org/10.1016/j.polymdegradstab.2021.109503

[76] Dole, P., & Chauchard, J. (1996). Thermooxidation of poly(ethylene-co-methyl acrylate) and poly(methyl acrylate) compared to oxidative thermal aging of polyethylene. *Polymer Degradation and Stability*, *53*(1), 63–72. https://doi.org/10.1016/0141-3910(96)00026-2

[77] Hardyal, K. (2020, October 15). *What is graphitization? A carbon/graphite engineer explains*. Retrieved December 8, 2021, from https://blog.metcar.com/what-is-graphitization

[78] Bruice, P. (2016). *Organic chemistry* (8th ed.). Pearson.

[79] msbo-Mattingly, S. D., & Stout, S. A. (2011). Semivolatile hydrocarbon residues of coal and coal tar. *Coal and Peat Fires: A Global Perspective*, 173–208. https://doi.org/10.1016/b978-0-444-52858-2.00011-6

[80] Redwood, B., Schöffer, F., & Garret, B. (n.d.). *What is 3D printing?* Retrieved December 15, 2021, from https://www.hubs.com/guides/3d-printing/

[81] Bagheri, A., & Jin, J. (2019). Photopolymerization in 3d printing. *ACS Applied Polymer Materials*, *1*(4), 593–611. https://doi.org/10.1021/acsapm.8b00165

[82] Xu, W., Jambhulkar, S., Zhu, Y., Ravichandran, D., Kakarla, M., Vernon, B., Lott, D. G., Cornella, J. L., Shefi, O., Miquelard-Garnier, G., Yang, Y., & Song, K. (2021). 3D printing for polymer/particle-based processing: A review. *Composites Part B: Engineering*, *223*, 109102. https://doi.org/10.1016/j.compositesb.2021.109102

[83] Gregersen, E. (n.d.). *Anisotropy definition, examples, & facts*. Retrieved March 7, 2022, from https://www.britannica.com/science/anisotropy

[84] Zhang, J., Yang, B., Fu, F., You, F., Dong, X., & Dai, M. (2017). Resistivity and its anisotropy characterization of 3D-printed acrylonitrile butadiene styrene copolymer (ABS)/carbon black (CB) composites. *Applied Sciences*, *7*(1), 20. https://doi.org/10.3390/app7010020

[85] Formlabs. (n.d.). *Validating isotropy in SLA 3D printing*. https://formlabs.com/blog/isotropy-in-SLA-3D-printing/

[86] Formlabs. (n.d.). *FDM vs. SLA: Compare the two most popular types of 3D printers*. https://formlabs.com/blog/fdm-vs-sla-compare-types-of-3d-printers/

[87] Griffin, M. (2020, March 26). *SLA printing is 3D printer resin toxic?* Retrieved March 7, 2022, from https://all3dp.com/2/sla-3d-printing-is-3d-printer-resin-toxic/

[88] Mazzucco, R. (2015, October). *Slow photopolymerisation kinetics in PMMA*. https://doi.org/10.13140/RG.2.1.1633.0004

[89] Borrello, J., Nasser, P., Iatridis, J. C., & Costa, K. D. (2018). 3D printing a mechanically-tunable acrylate resin on a commercial DLP-SLA printer. *Additive Manufacturing*, *23*, 374–380. https://doi.org/10.1016/j.addma.2018.08.019

[90] Alemán, J. V., Chadwick, A. V., He, J., Hess, M., Horie, K., Jones, R. G., Kratochvíl, P., Meisel, I., Mita, I., Moad, G., Penczek, S., & Stepto, R. F. T. (2007). Definitions of terms relating to the structure and processing of sols, gels, networks, and inorganic-organic hybrid materials (IUPAC recommendations 2007). *Pure and Applied Chemistry*, *79*(10), 1801–1829. https://doi.org/10.1351/pac200779101801

[91] Xometry Europe. (2021, July 20). *SLA 3D printing process*. https://xometry.eu/en/stereolithography-sla-3d-printing-technology-overview/

[92] Piedra-Cascón, W., Krishnamurthy, V. R., Att, W., & Revilla-León, M. (2021). 3D printing parameters, supporting structures, slicing, and post-processing procedures of vat-polymerization additive manufacturing technologies: A narrative review. *Journal of*

Dentistry, *109*, 103630. https://doi.org/10.1016/j.jdent.2021.103630

[93] Formlabs. (n.d.). *Form 3: Industrial-quality desktop SLA 3D printer*. https://formlabs.com/3d-printers/form-3/

[94] Formlabs. (n.d.). *Form Wash and Form Cure: Automated post-processing*. Retrieved November 20, 2021, from https://formlabs.com/post-processing/wash-cure/

[95] Formlabs. (2021, March 19). *When to use different layer heights*. Retrieved November 20, 2021, from https://support.formlabs.com/s/article/When-to-Use-Different-Layer-Heights?language=en_US

[96] Wang, P., Zhang, H., Wang, H., Li, D., Xuan, J., & Zhang, L. (2020). Hybrid manufacturing of 3D hierarchical porous carbons for electrochemical storage. *Advanced Materials Technologies*, *5*(6), 1901030. https://doi.org/10.1002/admt.201901030

[97] Sa-nguanruksa, J., Rujiravanit, R., Supaphol, P., & Tokura, S. (2004). Porous polyethylene membranes by template-leaching technique: Preparation and characterization. *Polymer Testing*, *23*(1), 91–99. https://doi.org/10.1016/s0142-9418(03)00066-7

[98] Shiohara, A., Prieto-Simon, B., & Voelcker, N. H. (2021). Porous polymeric membranes: Fabrication techniques and biomedical applications. *Journal of Materials Chemistry B*, *9*(9), 2129–2154. https://doi.org/10.1039/d0tb01727b

[99] Baker, R. W. (2004). *Membrane technology and applications* (2nd ed.). Wiley. https://doi.org/10.1002/0470020393

[100] Kellenberger, C. A., Luechinger, N. A., Lamprou, A., Rossier, M., Grass, R. N., & Stark, W. J. (2012). Soluble nanoparticles as removable pore templates for the preparation of polymer ultrafiltration membranes. *Journal of Membrane Science*, *387*, 76–82. https://doi.org/10.1016/j.memsci.2011.10.011

[101] Marshall Scientific. (n.d.). *Sartorius CPA324S balance*. https://www.marshallscientific.com/Sartorius-CPA324S-Balance-p/sa-cpa324s.htm

[102] Hughes, S. W. (2005). Archimedes revisited: A faster, better, cheaper method of accurately measuring the volume of small objects. *Physics Education*, *40*(5), 468–474. https://doi.org/10.1088/0031-9120/40/5/008

[103] Formlabs. (2019, April 2). *Form 3 vs. Form 2: Comparing Formlabs desktop 3D printers*. https://formlabs.com/blog/form-3-form-2-3d-printer-comparison/

[104] Formlabs. (2020, March). *Safety dta sheet High Temp V2 resin*. https://formlabs-media.formlabs.com/datasheets/2001047-SDS-ENEU-0.pdf

[105] Formlabs. (2021, June). *Form Cure time and temperature settings*. https://s3.amazonaws.com/servicecloudassets.formlabs.com/media/Finishing/Post-Curing/115001414464-Form%5C%20Cure%5C%20Time%5C%20and%5C%20Temperature%5C%20Settings/FormCurePost-CureSettings.pdf

[106] Formlabs. (2021, January). *Form Wash time settings*. https://s3.amazonaws.com/servicecloudassets.formlabs.com/media/Finishing/Washing/115001347744-Form+Wash+Time+Settings/FormWashSettings.pdf

[107] Milshtein, J. (2016). *Schematic representation of an assembled and a disassembled flow cell.* Massachusetts Institute of Technology, Brushett Research Group.

[108] Engels. (2018). Chapter 10 - thermoset adhesives. *Thermosets* (2nd ed., pp. 341–368). Elsevier. https://doi.org/10.1016/B978-0-08-101021-1.00010-1

[109] Nijmeijer, K. (2019). Polymer membranes for sustainable process applications - membrane formation [Lecture slides].

[110] Lu, W., Yuan, Z., Zhao, Y., Zhang, H., Zhang, H., & Li, X. (2017). Porous membranes in secondary battery technologies. *Chemical Society Reviews*, *46*(8), 2199–2236. https://doi.org/10.1039/c6cs00823b

[111] Bulte, A. M. W., Naafs, E. M., van Eeten, F., Mulder, M. H. V., Smolders, C. A., & Strathmann, H. (1996). Equilibrium thermodynamics of the ternary membrane-forming system nylon, formic acid and water. *Polymer*, *37*(9), 1647–1655. https://doi.org/10.1016/0032-3861(96)83714-1

[112] Abeysena, I., & Darrington, R. (2013, February 6). *Understanding concentration and evaporation technology: Part 1: Basic principles of commonly used evaporation techniques*. Retrieved February 23, 2022, from https://americanlaboratory.com/914-Application-Notes/130187-Understanding-Concentration-and-Evaporation-Technology-Part-1-Basic-Principles-of-Commonly-Used-Evaporation-Techniques/

[113] Atkins, P., & Paula, D. J. (2014). *Physical Chemistry: Thermodynamics, Structure, and Change* (Tenth). W. H. Freeman.

[114] Krongauz, V. V. (2010). Crosslink density dependence of polymer degradation kinetics: Photocrosslinked acrylates. *Thermochimica Acta*, *503*, 70–84. https://doi.org/10.1016/j.tca.2010.03.011

[115] Meyer, E. A., Castellano, R., & Diederich, F. (2003). Interactions with aromatic rings in chemical and biological recognition. *Angewandte Chemie International Edition*, *42*(11), 1210–1250. https://doi.org/10.1002/anie.200390319

[116] Chemwatch. (n.d.). *Chemwatch*. Retrieved February 21, 2022, from https://jr.chemwatch.net/chemwatch.web/home

[117] Hansen, C. M. (1970). Polymer coatings. Concepts of solvent evaporation phenomena. *Product R&D*, *9*(3), 282–286. https://doi.org/10.1021/i360035a004

[118] Freier, T., Kunze, C., & Schmitz, K. P. (2001). Solvent removal from solution-cast films of biodegradable polymers. *Journal of Materials Science Letters*, *20*(21), 1929–1931. https://doi.org/10.1023/a:1013174400236

[119] Martínez-Pellitero, S., Castro, M. A., Fernández-Abia, A. I., González, S., & Cuesta, E. (2017). Analysis of influence factors on part quality in micro-SLA technology. *Procedia Manufacturing*, *13*, 856–863. https://doi.org/10.1016/j.promfg.2017.09.143

[120] Park, J. M., Jeon, J., Koak, J. Y., Kim, S. K., & Heo, S. J. (2021). Dimensional accuracy and surface characteristics of 3D-printed dental casts. *The Journal of Prosthetic Dentistry*, *126*(3), 427–437. https://doi.org/10.1016/j.prosdent.2020.07.008

[121] Zhou, J. G., Herscovici, D., & Chen, C. C. (2000). Parametric process optimization to improve the accuracy of rapid prototyped stereolithography parts. *International Journal of Machine Tools and Manufacture*, *40*(3), 363–379. https://doi.org/10.1016/s0890-6955(99)00068-1

[122] Onuh, S. O., & Hon, K. K. B. (2001). Improving stereolithography part accuracy for industrial applications. *The International Journal of Advanced Manufacturing Technology*, *17*(1), 61–68. https://doi.org/10.1007/s001700170210

[123] Cheng, W., Fuh, J. Y. H., Nee, A. Y. C., Wong, Y. S., Loh, H. T., & Miyazawa, T. (1995). Multi-objective optimization of part- building orientation in stereolithography. *Rapid Prototyping Journal*, *1*(4), 12–23. https://doi.org/10.1108/13552549510104429

[124] Formlabs. (2020, June 17). *Design specifications for 3D models*. Retrieved February 9, 2022, from https://support.formlabs.com/s/article/Design-specifications-for-3D-models-form-3?language=en_US

[125] Formlabs. (2020, September 15). *Model orientation best practices for SLA printing*. Retrieved January 20, 2022, from https://support.formlabs.com/s/article/Model-Orientation?language=en_US

[126] Campanelli, S. L., Cardano, G., Giannoccaro, R., Ludovico, A. D., & Bohez, E. L. J. (2007). Statistical analysis of the stereolithographic process to improve the accuracy. *Computer-Aided Design*, *39*(1), 80–86. https://doi.org/10.1016/j.cad.2006.10.003

[127] Nakamoto, T., Yamaguchi, K., Abraha, P. A., & Mishima, K. (1996). Manufacturing of three-dimensional micro-parts by UV laser induced polymerization. *Journal of Micromechanics and Microengineering*, *6*(2), 240–253. https://doi.org/10.1088/0960-1317/6/2/006

[128] Manapat, J. Z., Chen, Q., Ye, P., & Advincula, R. C. (2017). 3D printing of polymer nanocomposites via stereolithography. *Macromolecular Materials and Engineering*, *302*(9), 1600553. https://doi.org/10.1002/mame.201600553

[129] Anastasio, R. (2019, October 10). *UV-cured polymer networks: From processing to properties* [dissertation]. Technische Universiteit Eindhoven.

[130] Lee, T. Y., Guymon, C. A., Jönsson, E. S., & Hoyle, C. E. (2004). The effect of monomer structure on oxygen inhibition of (meth)acrylates photopolymerization. *Polymer*, *45*(18), 6155–6162. https://doi.org/10.1016/j.polymer.2004.06.060

[131] Behera, D., Chizari, S., Shaw, L. A., Porter, M., Hensleigh, R., Xu, Z., Roy, N. K., Connolly, L. G., Zheng, X. R., Saha, S., Hopkins, J. B., & Cullinan, M. A. (2021). Current challenges and potential directions towards precision microscale additive manufacturing – part II: Laser-based curing, heating, and trapping processes. *Precision Engineering*, *68*, 301–318. https://doi.org/10.1016/j.precisioneng.2020.12.012

[132] Chua, C. K., Chou, S. M., & Wong, T. S. (1998). A study of the state-of-the-art rapid prototyping technologies. *The International Journal of Advanced Manufacturing Technology*, *14*(2), 146–152. https://doi.org/10.1007/bf01322222

[133] ASML. (n.d.). *All about light and lasers in lithography*. Retrieved February 11, 2022, from https://www.asml.com/en/technology/lithography-principles/light-and-lasers

[134] Chartoff, P., Flach, L., & Weissman, P. (Eds.). (1993). Material and process parameters that affect accuracy in stereolithography.

[135] ASML. (n.d.). *Lenses & mirrors - lithography principles*. Retrieved February 11, 2022, from https://www.asml.com/en/technology/lithography-principles/lenses-and-mirrors

[136] Biesinger, M. C. (2021). *X-ray photoelectron spectroscopy (XPS) reference page carbon*. Retrieved March 2, 2022, from http://www.xpsfitting.com/search/label/carbon

[137] Cameron, G. G., & Davie, F. (1973). The oxidative thermal degradation of poly (methyl acrylate). *Chemical Papers*, *26*, 200–207. https://www.chempap.org/file_access.php?file=263a200.pdf

[138] James, O. O., Mandal, S., Alele, N., Chowdhury, B., & Maity, S. (2016). Lower alkanes dehydrogenation: Strategies and reaction routes to corresponding alkenes. *Fuel Processing Technology*, *149*, 239–255. https://doi.org/10.1016/j.fuproc.2016.04.016

[139] Straus, S., & Madorsky, S. L. (1953). Pyrolysis of styrene, acrylate, and isoprene polymers in a vacuum. *Journal of Research of the Notional Bureau of Standards*, *50*(3), 165–176. https://nvlpubs.nist.gov/nistpubs/jres/50/jresv50n3p165_A1b.pdf

[140] Johnston, P. K., Doyle, E., & Orzel, R. A. (1988). Acrylics: A literature review of thermal decomposition products and toxicity. *Journal of the American College of Toxicology*, *7*(2), 139–200. https://doi.org/10.3109/10915818809014519

[141] Czech, Z., Agnieszka, K., Ragańska, P., & Antosik, A. (2014). Thermal stability and degradation of selected poly(alkyl methacrylates) used in the polymer industry. *Journal of Thermal Analysis and Calorimetry*, *119*(2), 1157–1161. https://doi.org/10.1007/s10973-014-4290-5

[142] Bertini, F., Audisio, G., & Zuev, V. V. (2005). Investigation on the thermal degradation of poly(n-alkyl acrylates) and poly(n-alkyl methacrylates) (C1–C12). *Polymer Degradation and Stability*, *89*(2), 233–239. https://doi.org/10.1016/j.polymdegradstab.2004.11.023

[143] Özlem-Gundogdu, S., Gurel, E. A., & Hacaloglu, J. (2015). Pyrolysis of poly(methyl methacrylate) copolymers. *Journal of Analytical and Applied Pyrolysis*, *113*, 529–538. https://doi.org/10.1016/j.jaap.2015.03.015

[144] Kostecki, R., Schnyder, B., Alliata, D., Song, X., Kinoshita, K., & Kötz, R. (2001). Surface studies of carbon films from pyrolyzed photoresist. *Thin Solid Films*, *396*(1-2), 36–43. https://doi.org/10.1016/s0040-6090(01)01185-3

[145] Biesinger, M. C. (2021). *X-ray photoelectron spectroscopy (XPS) reference page graphite*. Retrieved March 2, 2022, from http://www.xpsfitting.com/search/label/Graphite

[146] Vasudevan, P. (2021, November 16). *Why rectangular column shape preferred over circular column?* Retrieved February 27, 2022, from https://www.civilera.com/post/why-rectangular-column-shape-preferred-over-circular-column

[147] Yi, Y., Weinberg, G., Prenzel, M., Greiner, M., Heumann, S., Becker, S., & Schlögl, R.

(2017). Electrochemical corrosion of a glassy carbon electrode. *Catalysis Today*, *295*, 32–40. https://doi.org/10.1016/j.cattod.2017.07.013

[148] Halliday, D., Resnick, R., & Walker, J. (1996). *Fundamentals of physics, extended* (5th). Wiley.

Appendix A. Elaboration on methods

A.1. Volume measurement

The entire volume of small samples can be measured with the suspension method, which is based on the Archimedes' principle [102]. The principle states that: "an object fully or partially immersed in a fluid is buoyed up by a force equal to the weight of the fluid that the object displaces" [148]. An illustration of the method is given below in Figure A.1.

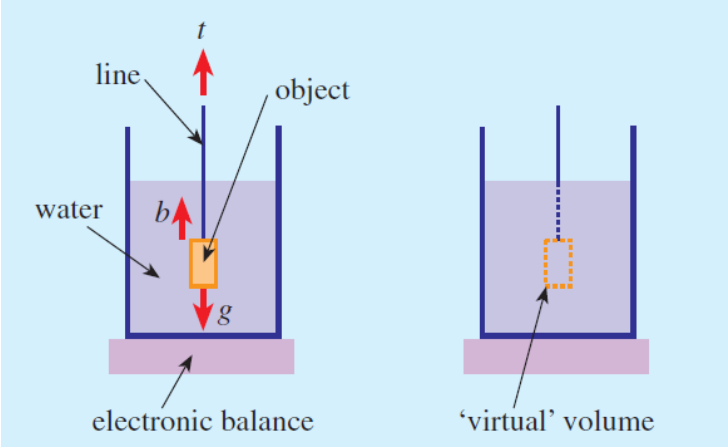

Figure A.1: Schematic representation of the suspension method for measuring volume. Since the immersed object is stationary, the downward gravitational force (g) is balanced by the upward buoyancy (b) and line tension (t). The immersed object is equivalent to a 'virtual' volume of water of exactly the same size and shape. From Hughes [102].

Hence, the volume of an object is the weight it creates while suspended in a liquid divided by the density of the liquid, as is given in Equation A.1

$$V_{sample} = \frac{\Delta w_{liquid}}{\rho_{liquid}} \tag{A.1}$$

This method has according to the work of Hughes [102] an accuracy of 0.03 ± 0.45%, and performs better than the overflow or level method for measuring small volumes specifically [102]. IPA was used as liquid for the measurement of the change in volume of the plastic samples caused by different heat treatments due to the hydrophobicity of the samples. Unfortunately, the volume measurements could not be performed for the carbonized samples, as they could not easily wet in IPA, and did not weigh enough for the lab scale to measure an significant difference. The difficulty in wetting was most likely due to the compact grid structure, which comprised a lot of small air pockets. This assumption is based on the fact that the material did wet in an organic liquid, but only after some time on a rolling bench.

The density of the samples were found by dividing the weight of the sample with the volume of the sample, according to Equation A.2.

$$\rho_{sample} = \frac{V_{sample}}{w_{sample}} \tag{A.2}$$

A.2. Structure of electrode

First the of one rod is computed based on a set length of holes L and size of rod d:

$$H_{square} = 2 \times d_{square} + z_H \times L_{square} + (z_H + 1 - 2) \times 0.5 \times d_{square}$$

$$h_{triangle} = 2 \times \sqrt{(\frac{3}{4})} \times d_{triangle} + z_H \times L_{triangle} + (z_H + 1 - 2) \times d_{triangle}$$

$$h_{ylinder} = 2 \times d_{cylinder} + z_H \times L_{cylinder} + (z_H + 1 - 2) \times d_{cylinder}$$

Then the number of elements in the grid is computed based on a given amount of units in the X, Y, and Z direction (x_H, y_H, z_H):

$$holes = x_H \times y_H \times z_H$$

$$blocks = (x_H + 1) \times (y_H + 1) \times (z_H + 1)$$

$$rods = (x_H \times (y_H + 1) + y_H \times (x_H + 1)) \times (z_H + 1) + ((x_H + 1) \times (y_H + 1)) \times z_H$$

Then the area is the electrode calculated for each shape rod:

$$area_{total} = area_z + area_{xy}$$

$$area_{squarexy} = (1 + 1) \times 3 \times (d_{square} \times L_{square}) \times (x_H \times (y_H + 1) + y_H \times (x_H + 1)) + (z_H + 1 - 2) \times 4 \times (d_{square} \times L_{square}) \times (x_H \times (y_H + 1)$$

$$area_{squarez} = 4 \times (d_{square} \times L_{square}) \times ((x_H + 1) \times (y_H + 1)) \times z_H$$

$$area_{trianglexy} = (1 + 1) \times 2 \times (d_{triangle} \times L_{triangle}) \times (x_H \times (y_H + 1) + y_H \times (x_H + 1)) + (z_H + 1 - 2) \times 3 \times (d_{square} \times L_{square}) \times (x_H \times (y_H + 1)$$

$$area_{trianglez} = 3 \times (d_{triangle} \times L_{triangle}) \times ((x_H + 1) \times (y_H + 1)) \times z_H$$

$$area_{cylinderexy} = (1 + 1) \times 0.75 \times (d_{cylinder} \times L_{cylinder} \times \pi) \times (x_H \times (y_H + 1) + y_H \times (x_H + 1)) + (z_H + 1 - 2) \times (d_{cylinder} \times L_{cylinder} \times \pi) \times (x_H \times (y_H + 1)$$

$$area_{cylinderz} = 1 \times (d_{cylinder} \times L_{cylinder}) \times ((x_H + 1) \times (y_H + 1)) \times z_H$$

Then the volume is calculated, from which the porosity was derived:

$$volume_{square} = d_{square}^2 \times L_{square} \times rods + d_{square}^3 \times blocks$$

$$volume_{triangle} = d^2_{square} \times \sqrt{\frac{3}{4}} \times L_{triangle} \times rods + d^3_{triangle} \times blocks$$

$$volume_{1rodcylinder} = \pi \times d^2_{cylinder} \times L_{cylinder} \times \frac{1}{4}$$

$$volume_{cylinder} = (1+1) \times 0.75 \times (x_H \times (y_H + 1) + y_H \times (x_H + 1)) \times volume_{1rodcylinder}$$
$$+ (z_H + 1 - 2) \times (x_H \times (y_H + 1) + y_H \times (x_H + 1)) \times volume_{1rodcylinder} + d^3_{cylinder} \times blocks$$

Appendix B. Additional figures of results 3D printing

B.1. Deviations measured holes and beams

see below

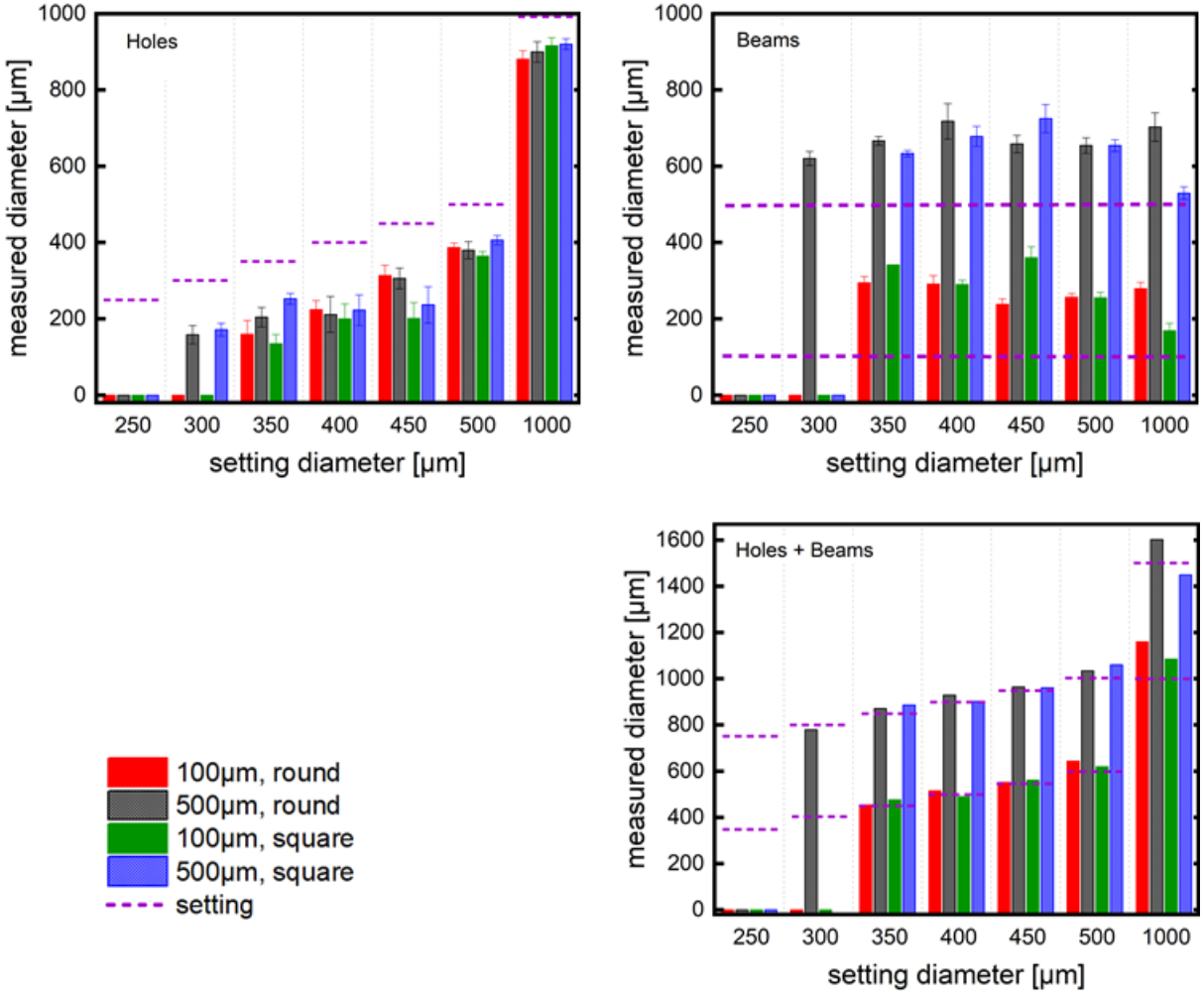

Figure B.1: Measured performance of the Form 3 on printing accuracy of the holes. Top left shows the average diameter of the holes, top right shows the average size of the solidified space between the holes, and bottom right shows the average diameter of the hole + the size of the solidified space in between. The shape and spacing of the holes is indicated in the legend.

Appendix C. Additional figures of results polymerization-induced phase separation

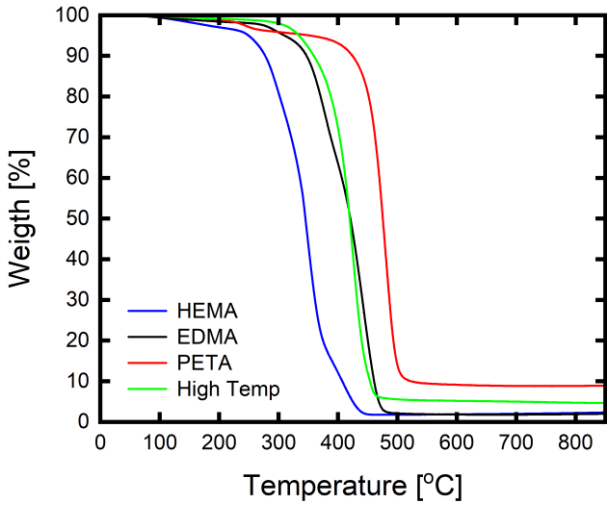

Figure C.1: TGA under N_2 of polyacrylate made with various acrylate monomers

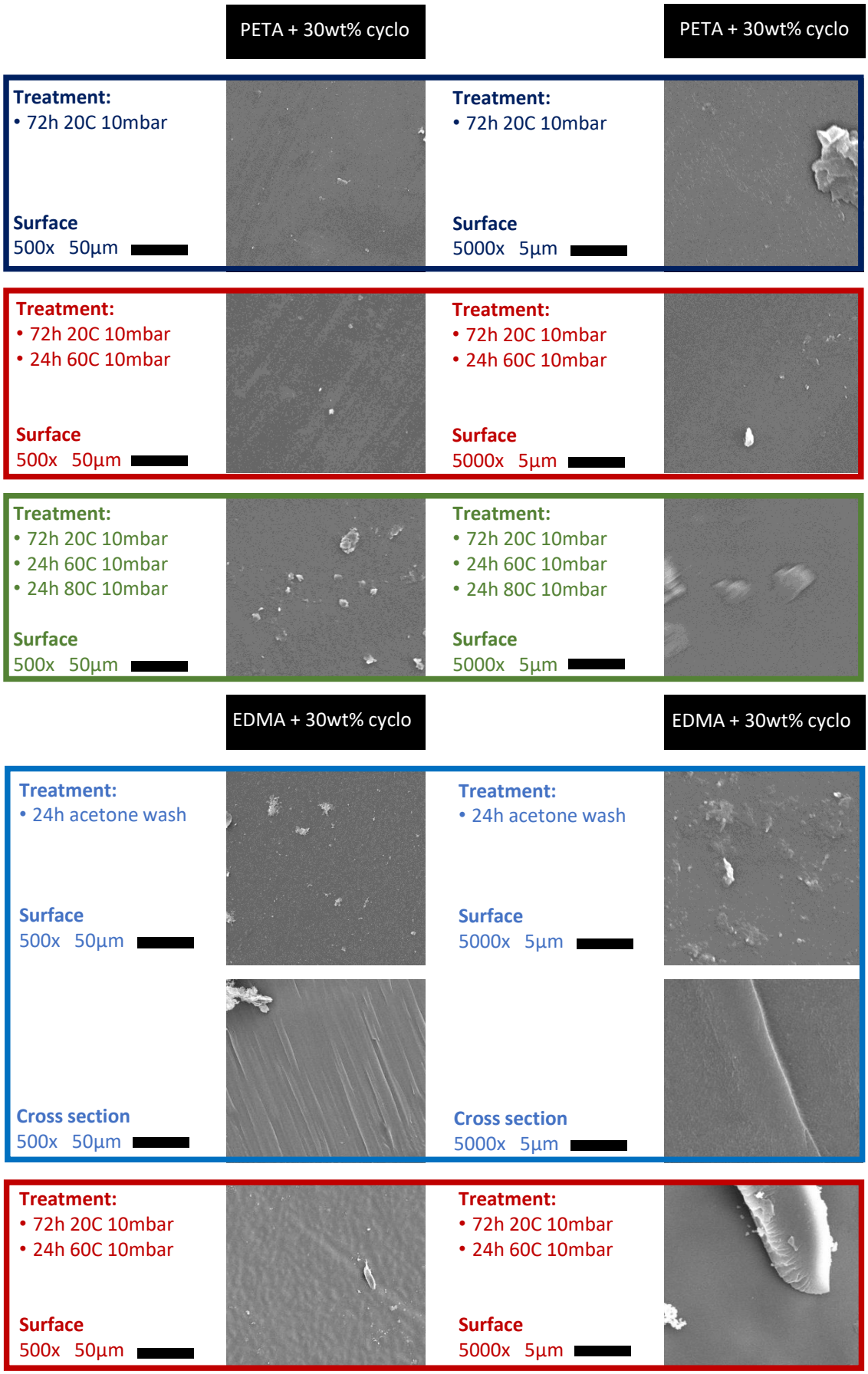

Figure C.2: Image taken with a SEM at a 500× and 5000× magnification of the surface and cross section of polymerized PETA (top) and EDMA (bottom) + 30 wt% cyclohexanol after various extraction treatments (rows).

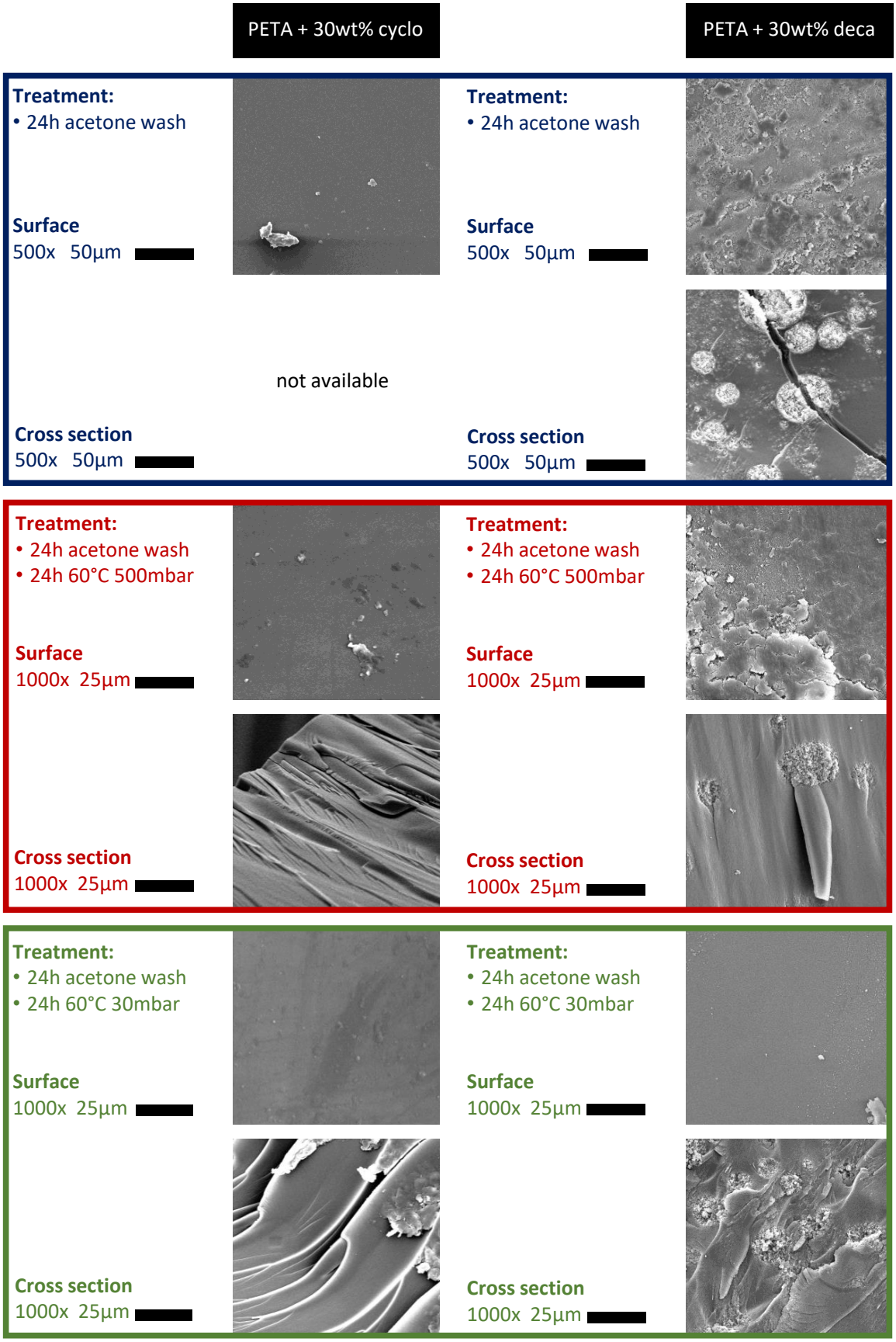

Figure C.3: Image taken with a SEM at a 500× and 1000× magnification of the surface and cross section of polymerized PETA + 30 wt% cyclohexanol (left) and 1-decanol (left) after various extraction treatments (rows).

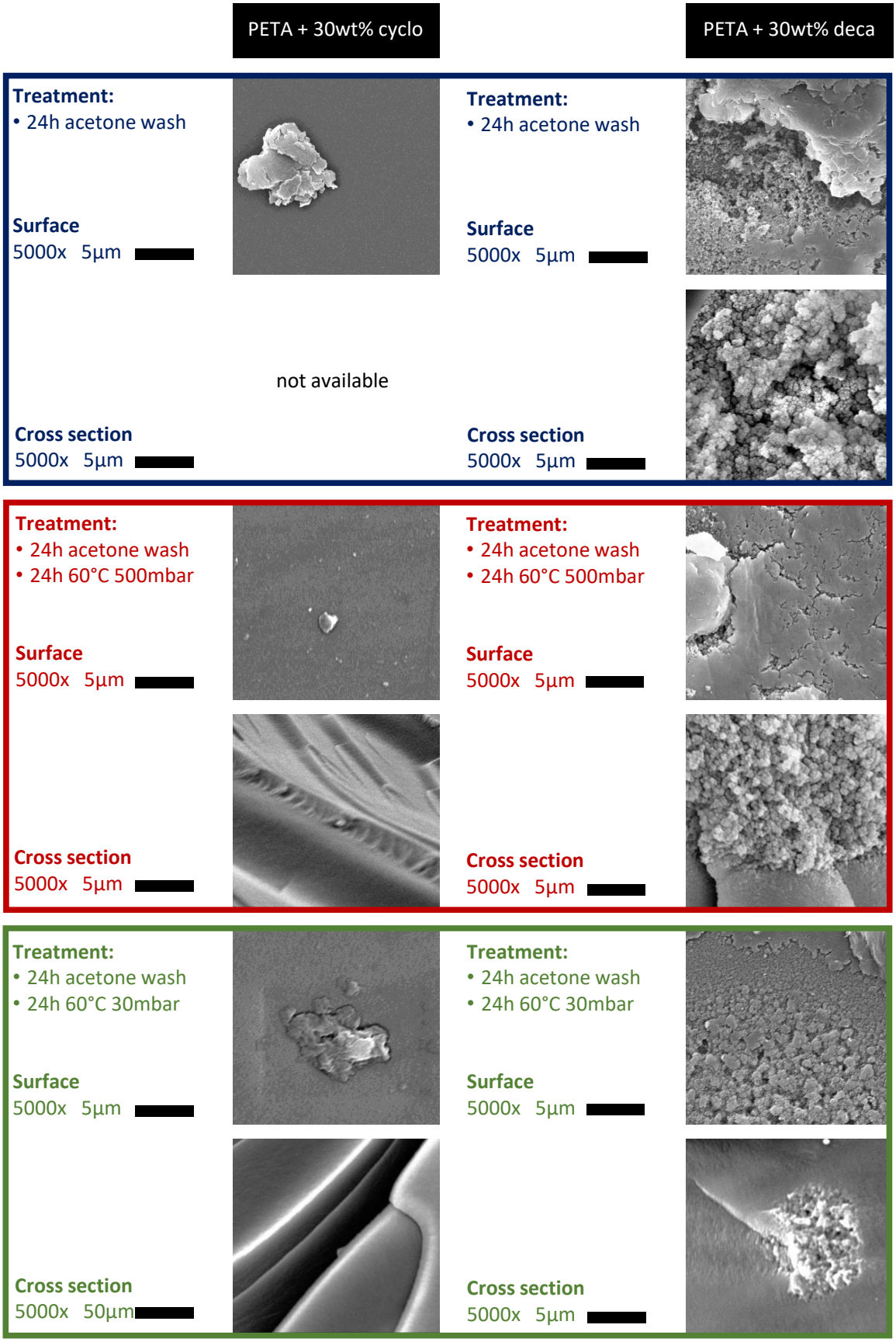

Figure C.4: Image taken with a SEM at a 5000× magnification of the surface and cross section of polymerized PETA + 30 wt% cyclohexanol (left) and 1-decanol (left) after various extraction treatments (rows).

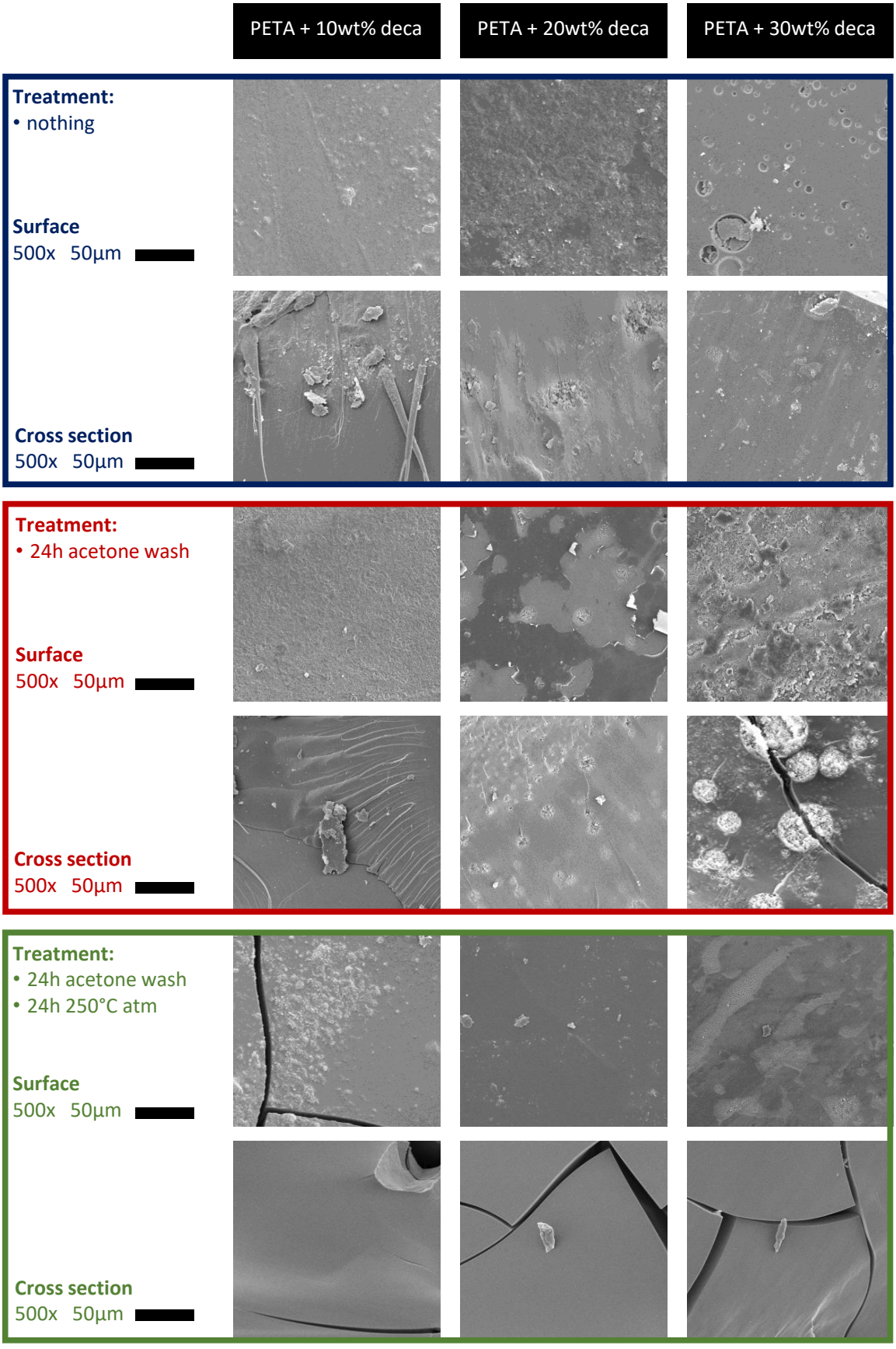

Figure C.5: Image taken with a SEM at a 500× magnification of the surface and cross section of polymerized PETA + 10 wt% (left) 1-decanol, + 20 wt% 1-decanol (middle), and + 30 wt% 1-decanol (right) after various extraction treatments (rows) part 1.

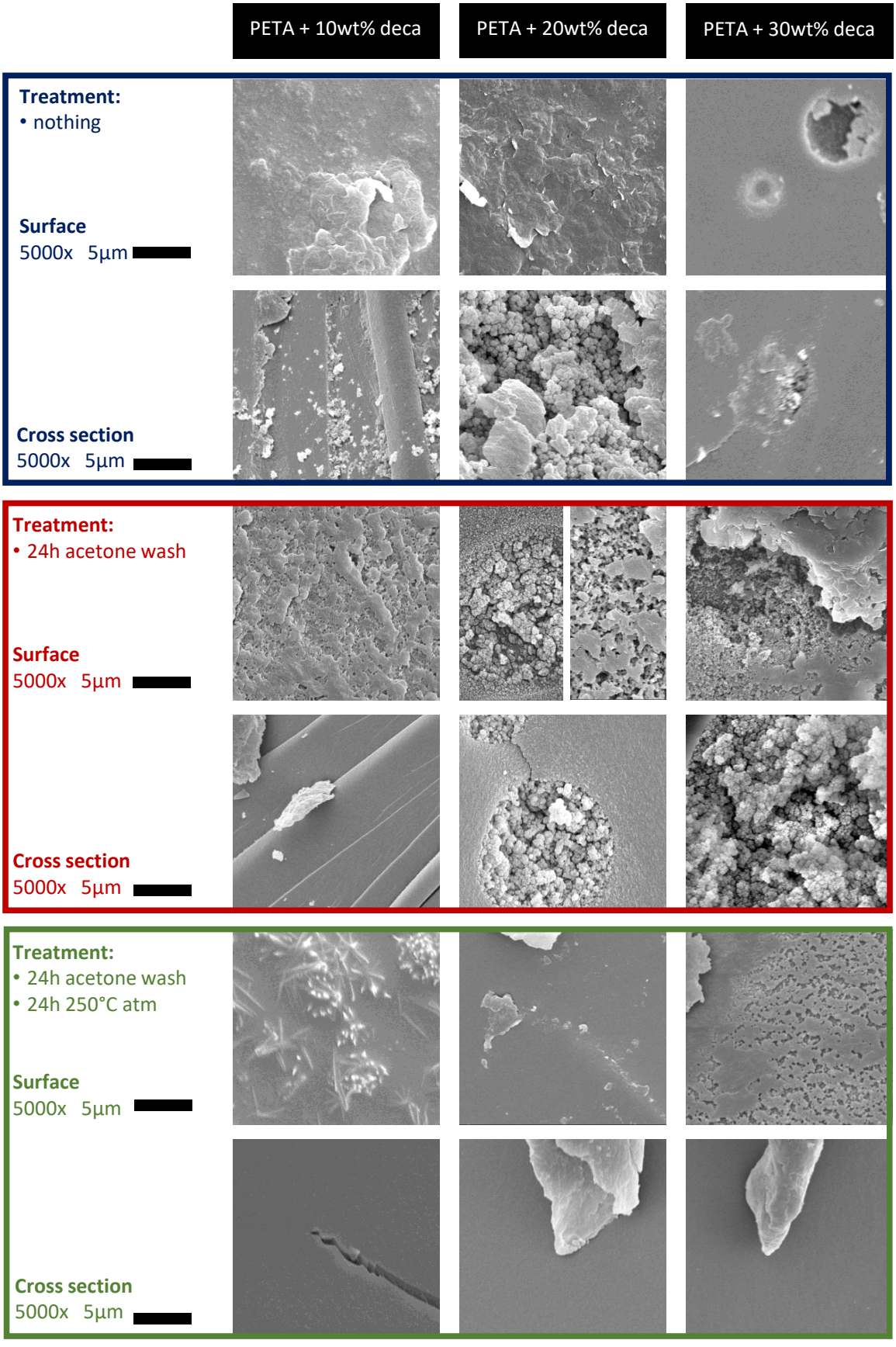

Figure C.6: Image taken with a SEM at a 5000× magnification of the surface and cross section of polymerized PETA + 10 wt% (left) 1-decanol, + 20 wt% 1-decanol (middle), and + 30 wt% 1-decanol (right) after various extraction treatments (rows) part 1.

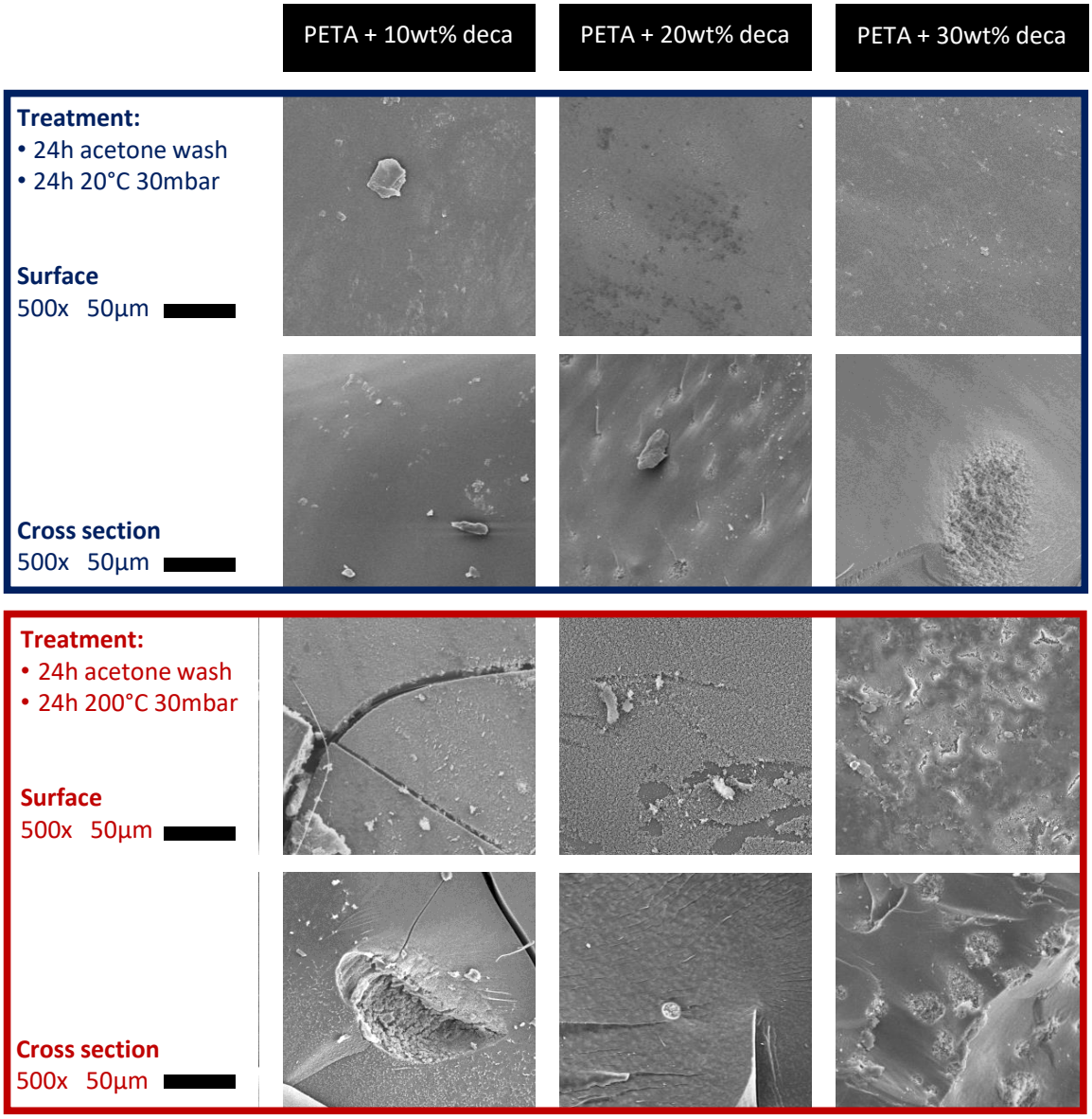

Figure C.7: Image taken with a SEM at a 500× magnification of the surface and cross section of polymerized PETA + 10 wt% (left) 1-decanol, + 20 wt% 1-decanol (middle), and + 30 wt% 1-decanol (right) after various extraction treatments (rows) part 2.

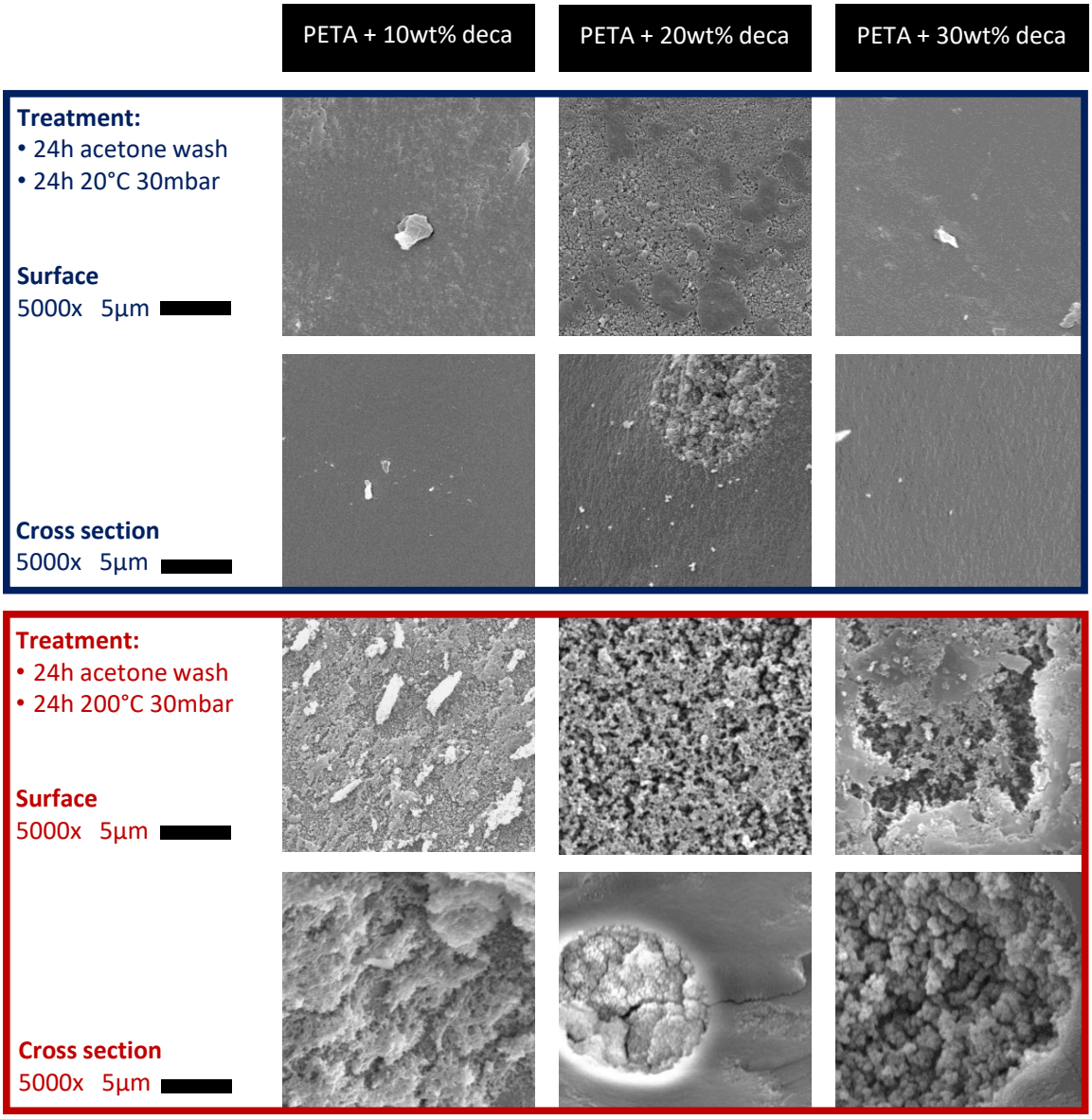

Figure C.8: Image taken with a SEM at a 5000× magnification of the surface and cross section of polymerized PETA + 10 wt% (left) 1-decanol, + 20 wt% 1-decanol (middle), and + 30 wt% 1-decanol (right) after various extraction treatments (rows) part 2.

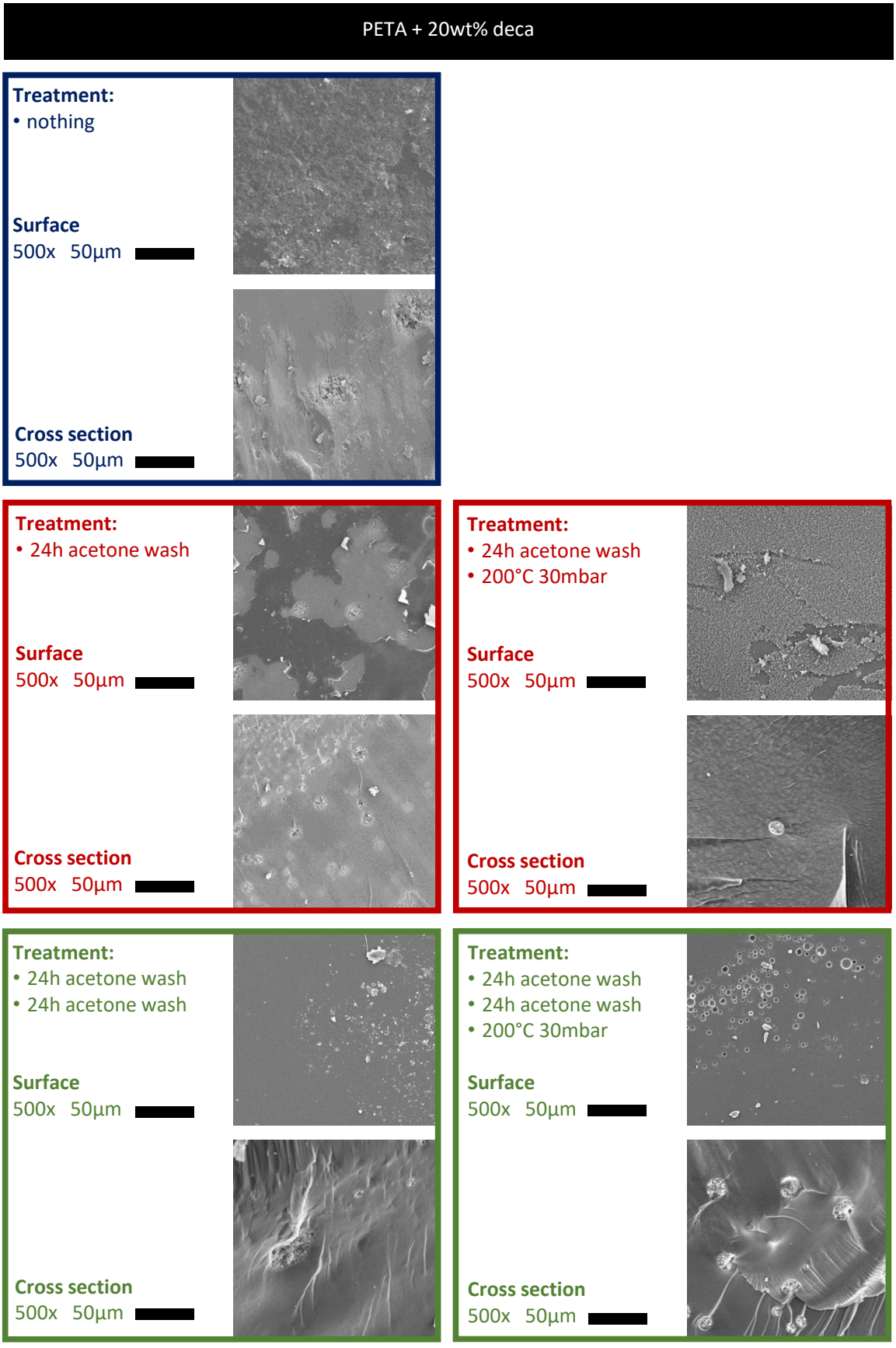

Figure C.9: Image taken with a SEM at a 500× magnification of the surface and cross section of polymerized PETA + 20 wt% 1-decanol with no treatment (top) and washed with acetone (middle and bottom) after various extraction treatments (rows and columns).

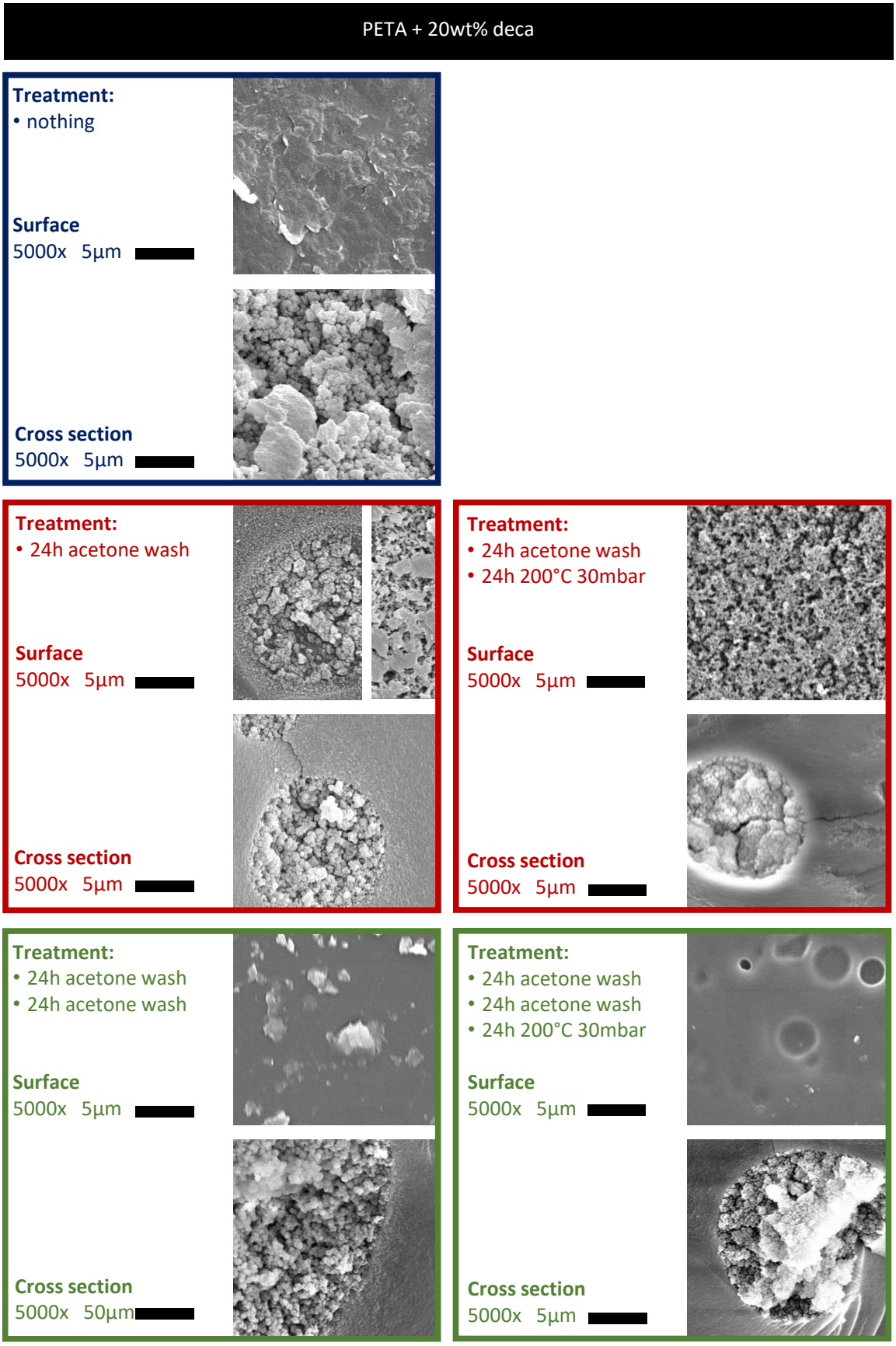

Figure C.10: Image taken with a SEM at a 5000× magnification of the surface and cross section of polymerized PETA + 20 wt% 1-decanol with no treatment (top) and washed with acetone (middle and bottom) after various extraction treatments (rows and columns).

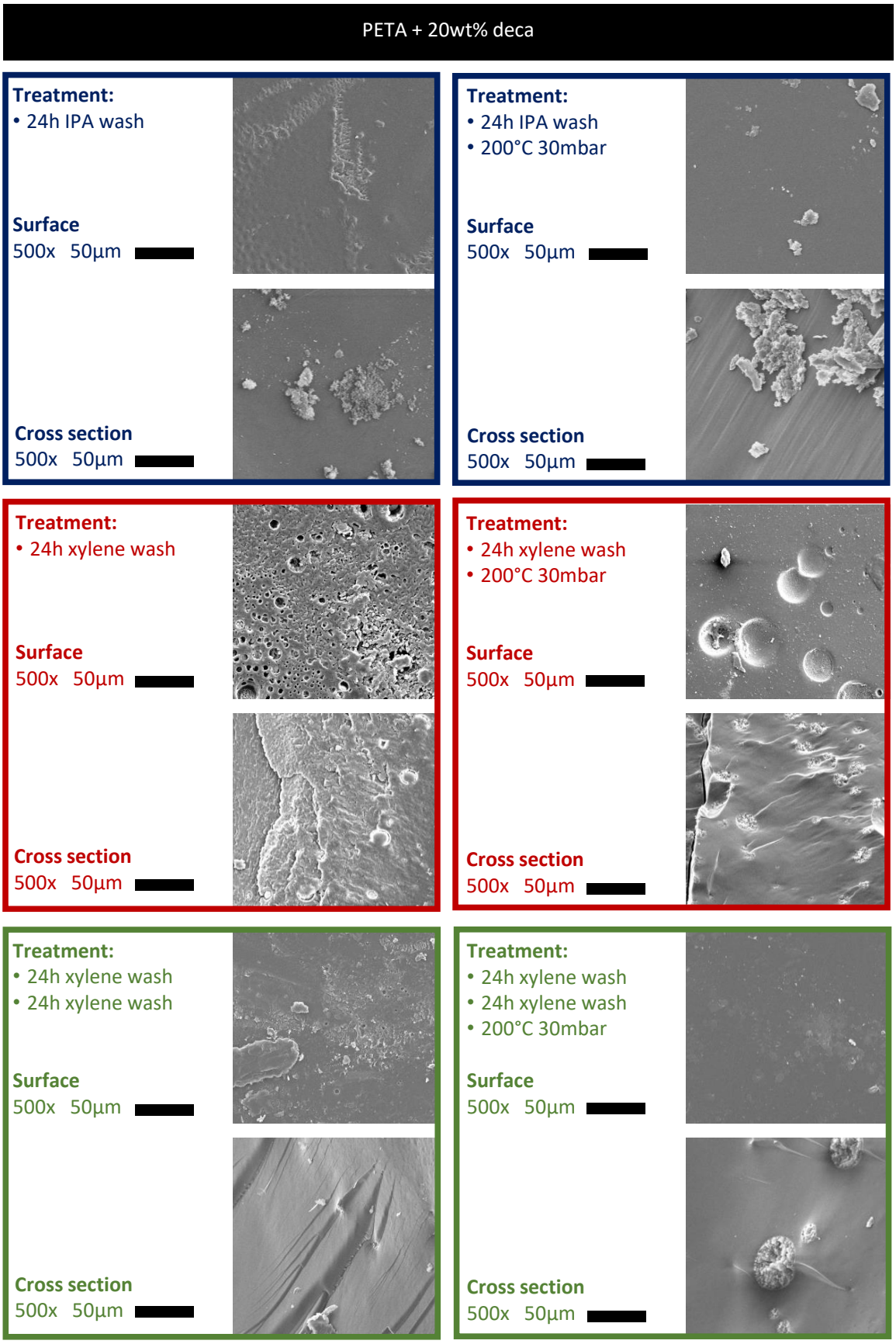

Figure C.11: Image taken with a SEM at a 500× magnification of the surface and cross section of polymerized PETA + 20 wt% 1-decanol washed with IPA (top) and with xylene (middle and bottom) after various extraction treatments (rows and columns).

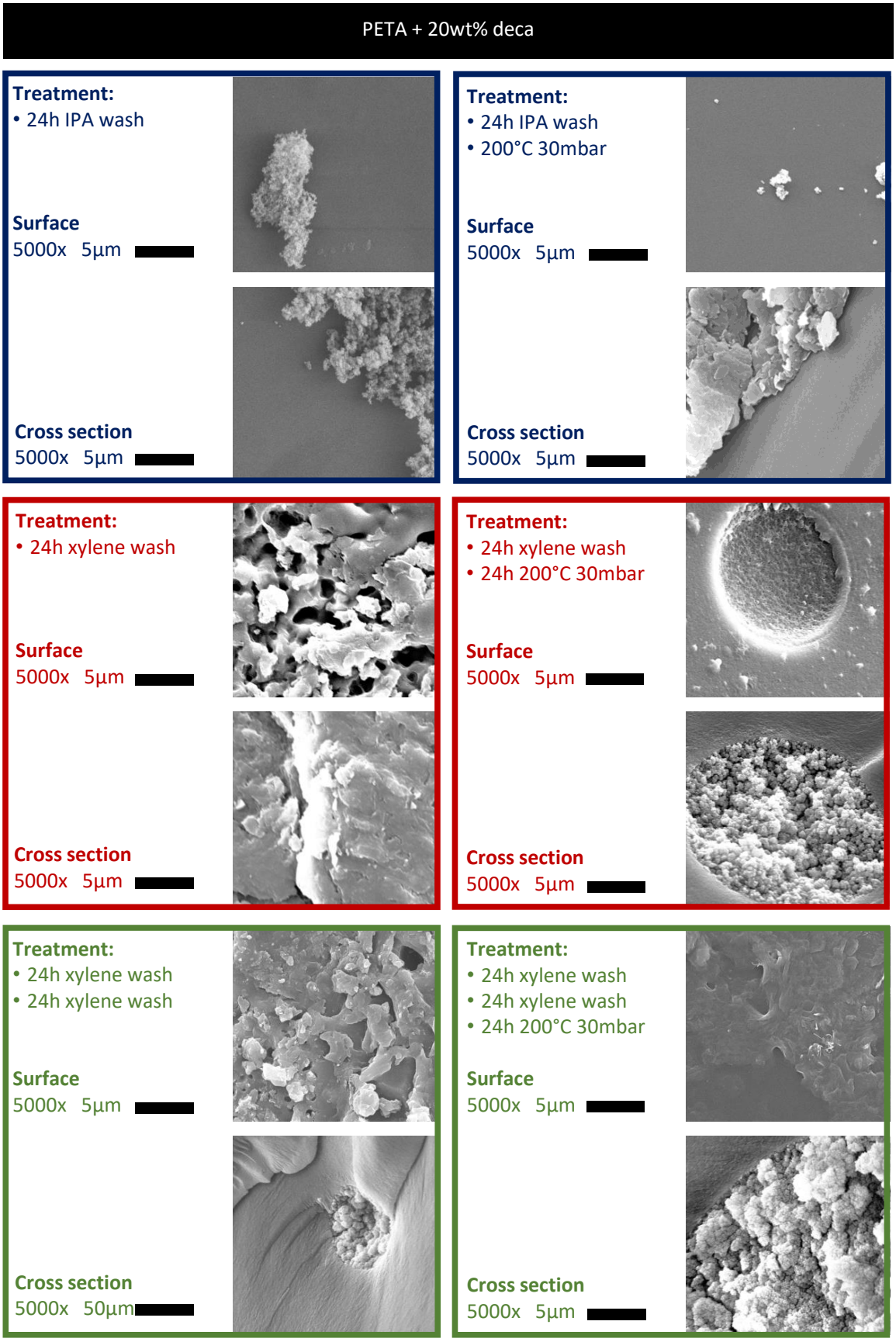

Figure C.12: Image taken with a SEM at a 5000× magnification of the surface and cross section of polymerized PETA + 20 wt% 1-decanol washed with IPA (top) and with xylene (middle and bottom) after various extraction treatments (rows and columns).

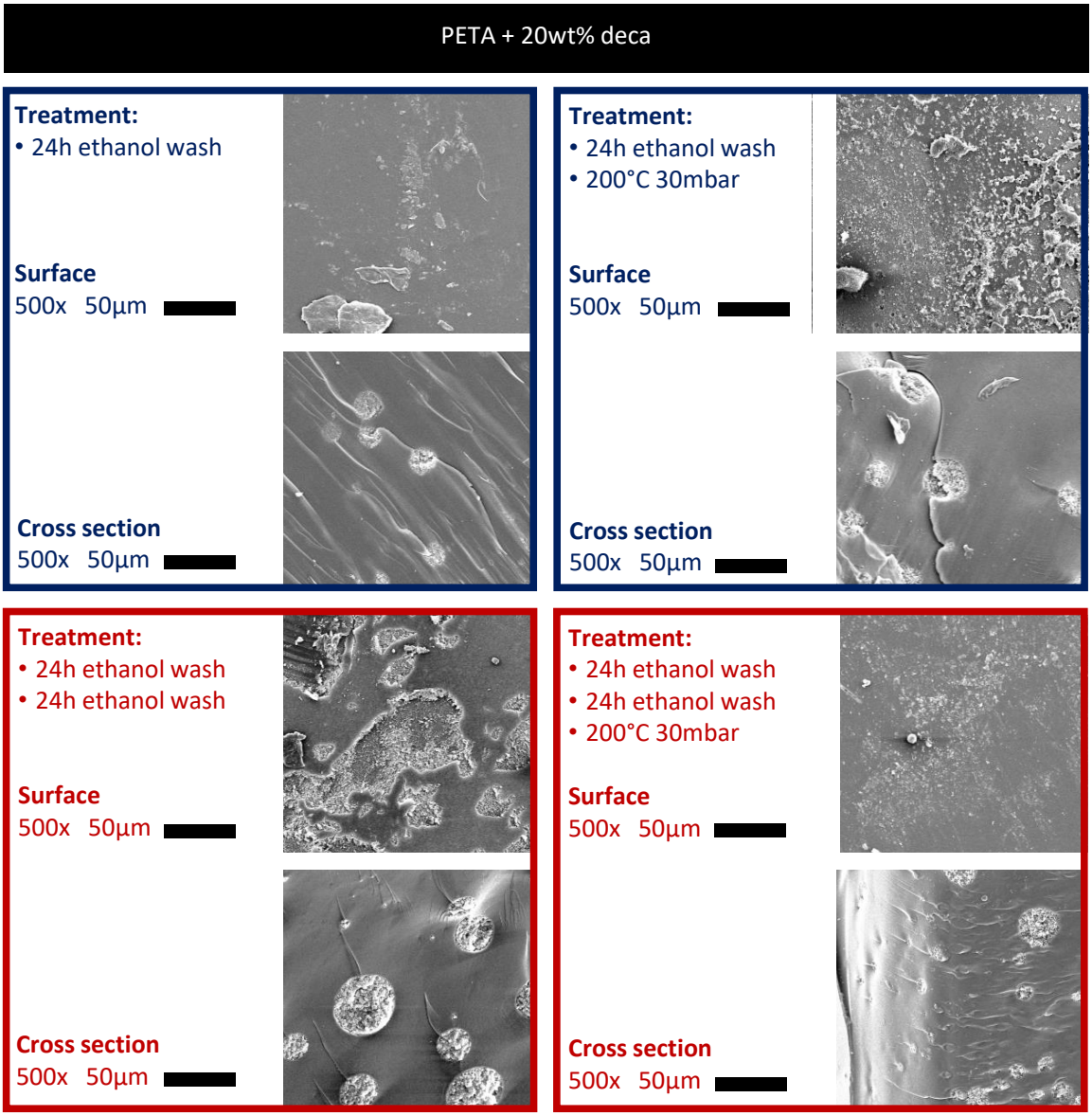

Figure C.13: Image taken with a SEM at a 500× magnification of the surface and cross section of polymerized PETA + 20 wt% 1-decanol washed ethanol after various extraction treatments (rows and columns).

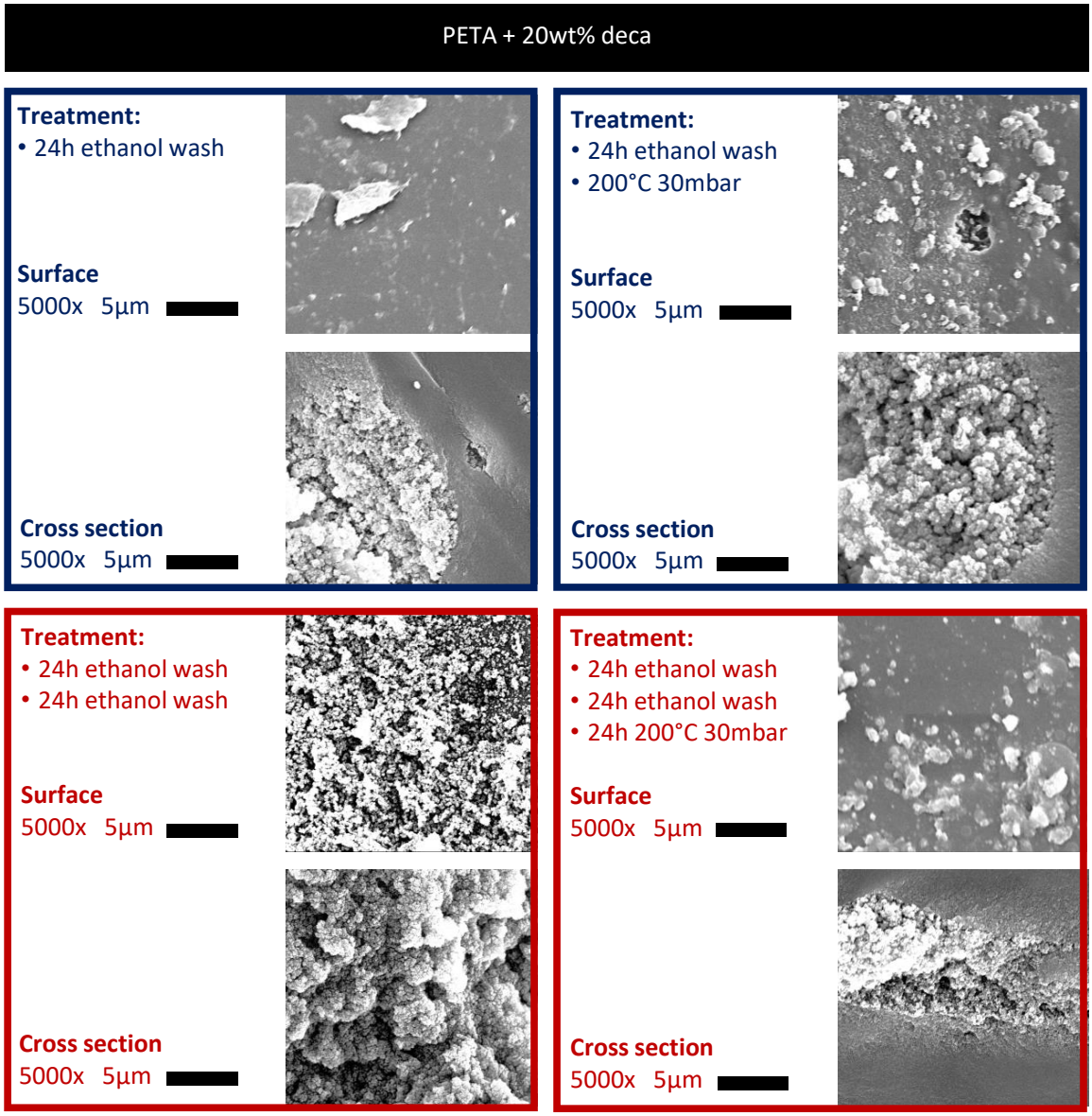

Figure C.14: Image taken with a SEM at a 5000× magnification of the surface and cross section of polymerized PETA + 20 wt% 1-decanol washed with ethanol after various extraction treatments (rows and columns).

Appendix D. Additional figures of results heat treatments

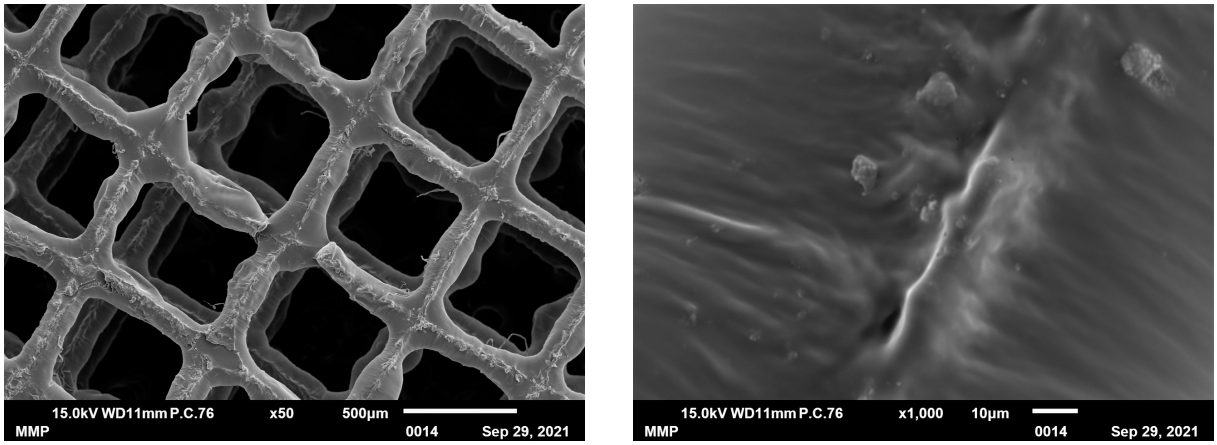

Figure D.1: Surface image taken with a SEM with a 50× and 1000× magnification of oxidized (5 h at 250 °C) and carbonized (5 h at 850 °C) electrode.

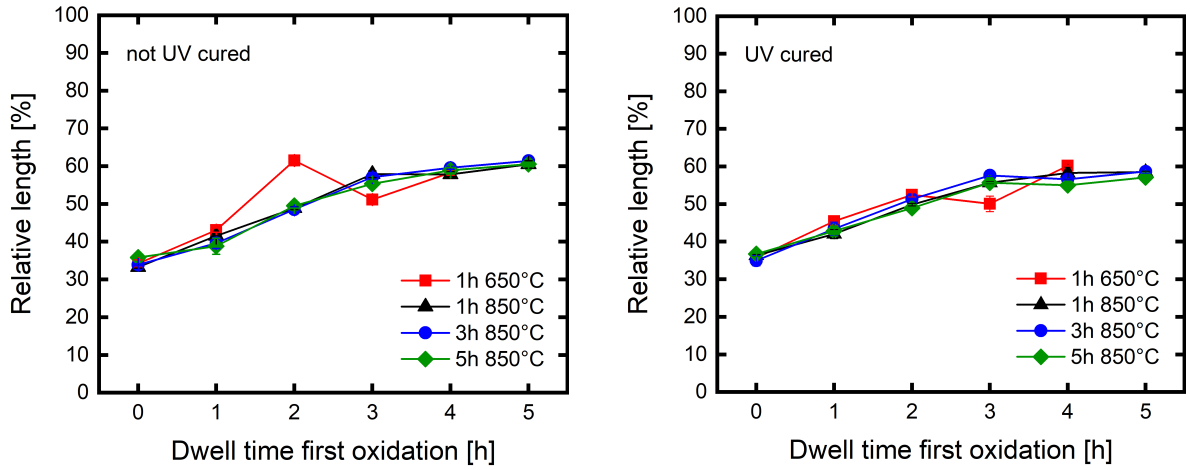

Figure D.2: The effect of the oxidation dwell time (x axis) and the dwell time and temperature of the carbonization (lines) on the length of the non UV cured samples (left) and UV cure samples (right). The length of the carbonized samples is given relative to untreated length.

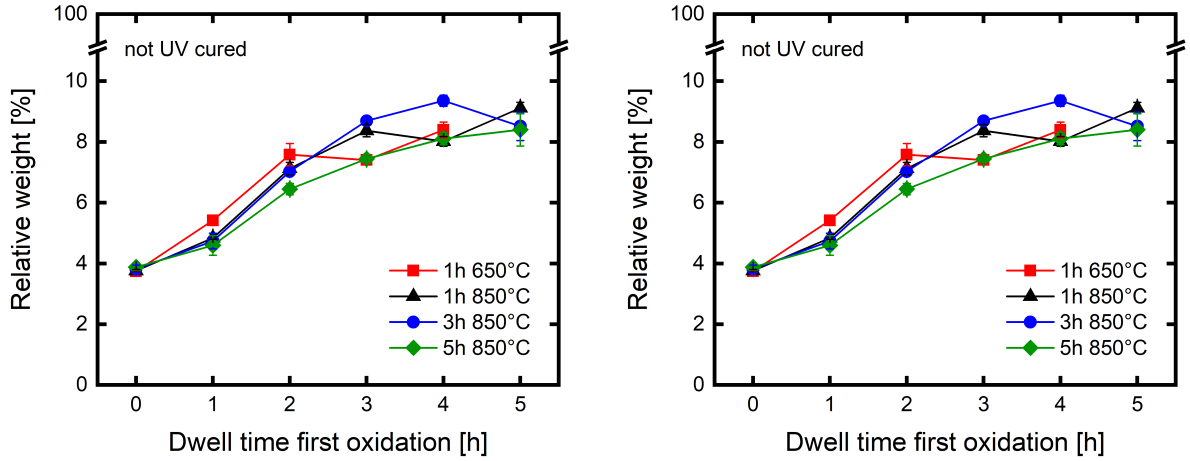

Figure D.3: The effect of the oxidation dwell time (x axis) and the dwell time and temperature of the carbonization (lines) on the weight of the non UV cured samples (left) and UV cure samples (right). The weight of the carbonized samples is given relative to untreated weight.

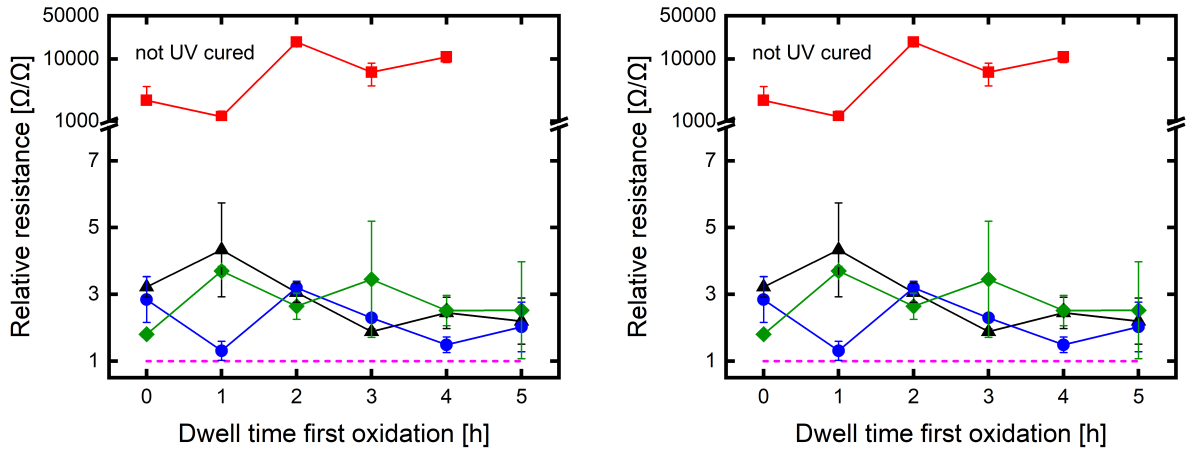

Figure D.4: The effect of the oxidation dwell time (x axis) and the dwell time and temperature of the carbonization (lines) on the electrical resistance of the non UV cured samples (left) and UV cure samples (right). The resistance is plotted relative to that of a Freudenberg paper. Note that the relative resistance is plotted linearly for low ratios, but logarithmically for high ratios.